This is to certify that the

dissertation entitled

SYNTHESIS AND STRUCTURAL STUDIES OF ALKALIDES AND ELECTRIDES THAT CONTAIN Rb^- AND COMPLEXED Rb^+

presented by

Odette Fussa'

has been accepted towards fulfillment
of the requirements for

Ph.D. degree in Chemistry

James L. Dye
Major professor

Date 9/01/86

SYNTHESIS AND STRUCTURAL STUDIES OF ALKALIDES AND ELECTRIDES THAT CONTAIN Rb^- AND COMPLEXED Rb^+

By

Odette Fussá

A DISSERTATION

Submitted to
Michigan State University
in partial fulfillment of the requirements
for the degree of

DOCTOR OF PHILOSOPHY

Department of Chemistry

1986

ABSTRACT

SYNTHESIS AND STRUCTURAL STUDIES OF ALKALIDES AND ELECTRIDES THAT CONTAIN Rb^- AND COMPLEXED Rb^+

By

Odette Fussá

Three new rubidides, $Cs^+(18C6)_2Rb^-$, $K^+C222Rb^-$, and $Li^+C211Rb^-$, were synthesized. $Cs^+(18C6)_2Rb^-$ was identified as a pure rubidide by optical spectroscopy, ^{87}Rb and ^{133}Cs solid state NMR and Rb K-edge XANES spectroscopy. EPR, magnetic susceptibility and dc conductivity indicated that this compound contains a small concentration of mutually non-interacting trapped electrons. $K^+C222Rb^-$ was identified as a rubidide by optical spectroscopy and XANES.

The structure of $Rb^+(15C5)_2Na^-$ was determined by single crystal X-ray diffraction. The unit cell is monoclinic (C2/m) with a = 11.555(3) Å, b = 13.587(3) Å, c = 9.958(3) Å, β = 92.03(2)°, and Z = 2.

The structure of $Rb^+(18C6)Br^-$ dihydrate was obtained by X-ray diffraction to serve as a model in XANES and EXAFS studies. The unit cell is orthorhombic (P_{nma}) with

a = 10.110(3) Å, b = 15.173(5) Å, c = 12.519(5) Å, and Z = 4.

An extensive series of rubidium-containing alkalides and electrides was studied by rubidium K-edge XANES and EXAFS. The XANES studies allowed the unambiguous identification of $Cs^+(18C6)_2Rb^-$, $K^+C222Rb^-$ and $Cs^+(15C5)_2Rb^-$ as pure rubidides, and of $RbK(15C5)_2$ and RbK(18C6) as mixtures of both potasside and rubidide. $Rb^+(15C5)_2Na^-$ and $Rb^+(18C6)Na^-$ are pure sodides. Powders of the electrides $Rb^+(15C5)_2e^-$and Rb^+C222e^- were identified and distinguished from the corresponding rubidides $Rb^+(15C5)_2Rb^-$, and $Rb^+C222Rb^-$.

Rubidium K-edge EXAFS results for complexes of the form $Rb^+(15C5)_2N^-$, for N^-= Na^-, Rb^- or e^-, indicated similar structures as evidenced by similarities in the distances (Rb^+ - O, 2.95 - 3.01 Å; Rb^+ - C, 3.80 - 3.82 Å), and the number of neighbors. $Rb^+(15C5)_2Na^-$ was used as model.

$Rb^+(18C6)SCN^-$ and $Rb^+(18C6)Br^-$ dihydrate were models for compounds of the form $Rb^+(18C6)N^-$ with N = Na^- or Rb^-. The results indicate that $Rb^+(18C6)Na^-$ has typical Rb^+- O (2.95 Å) and Rb^+- C (3.73 Å) distances and coordination numbers, which indicate complexation by a single crown. For $Rb^+(18C6)Rb^-$ and Rb(18C6), three sets of distances were obtained (Rb^+- O, 2.92-2.99 Å; Rb^+- X, 3.60-3.64 Å; Rb^+- C, 3.75-3.77 Å). It has been postulated that the distances of 3.60-3.64 Å are due to coordination to crown-ether oxygens,

elongated by a distortion in the ring.

To my mother
and to Tim

ACKNOWLEDGMENTS

I am deeply grateful to Dr. James L. Dye for the guidance and support he provided throughout the course of this work. I also wish to thank Dr. Boon-K. Teo for his guidance and help with the X-ray absorption spectroscopy project, and Dr. Donald L. Ward for his guidance and collaboration with the crystal structure determinations. In addition, I wish to thank Dr. Richard Schwendeman, my second reader, for his valuable suggestions on this manuscript. I am also grateful to the other members of my committee, Dr. Thomas Pinnavaia, and Dr. Chris K. Chang.

I wish to thank all the members of Dr. Dye's group for their help, friendship and support. The camaraderie shared in the lab will never be forgotten. I am especially grateful to those group members who assisted in the collection of the EXAFS data at CHESS, Steven Dawes, Margaret Faber, Rui Huang and Jineun Kim. Thanks also go to Long D. Le, Ahmed Ellaboudy, Mary Tinkham, John Papaioannou, Zheng Li, Francoise Tientega, Lauren Hill, Mark Kuchenmeister and Joseph Skowyra.

I also wish to thank the technical staff for their excellent work in manufacturing the equipment that was used throughout this work. I am especially grateful to

glassbowers Keki Mistry, Manfred Langer and Scott Bancroft, electronics designer Marty Rabb and machinists Deak Watters, Russ Geyer and Dick Menke. I appreciate the help of Carol Zink in typing Chapter 4, and of graphics artists Bill Draper and Bev Adams, who prepared a portion of the figures.

Finally, I wish to thank the members of my family, especially my grandmother Carla, for their faith in me and their support, even though they were physically so far away. I am especially grateful to my mother, Zaida and to my fiancé Tim, for their continuous encouragement, love and support. To them I dedicate this work.

Financial support provided by the Department of Chemistry, the Minority Competitive Doctoral Fellowships Program at Michigan State University, and the National Science Foundation (grants DMR 79-21979 and DMR 84-14154) is gratefully acknowledged.

TABLE OF CONTENTS

PAGE

PAGE

LIST OF TABLES

LIST OF FIGURES

CHAPTER ONE

INTRODUCTION

The chemistry of the alkali metals as presented in inorganic chemistry textbooks is, for the most part, based on their strongly electropositive nature. The metals have the lowest ionization potentials in the periodic table and release their weakly held valence s electron to form ionic compounds. Over the past decade, new types of compounds of the alkali metals have been synthesized which significantly expand their chemistry.

Alkalides are novel ionic solids in which the anion is a reduced alkali metal [1 - 12]. Numerous alkalides have been synthesized with Na^-, K^-, Rb^-, or Cs^- as the anionic species. The cation in these salts consists of an alkali metal cation -which may be or may not be the same alkali metal as that of the anion - complexed by an organic macrocycle such as a cryptand [13 - 14] or a crown ether [15 -16]. Among the complexants most extensively used are the bicyclic polyoxadiamine, cryptand 222, or C222, and the macrocyclic polyethers 18-crown-6, and 15-crown-5, (Figure 1). The coordination of the alkali metal cation by the ether oxygens (and the nitrogens of the cryptands) provides

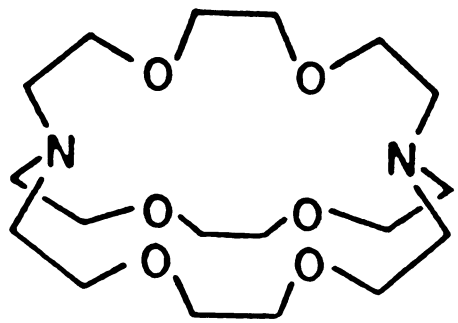

C2 2 2

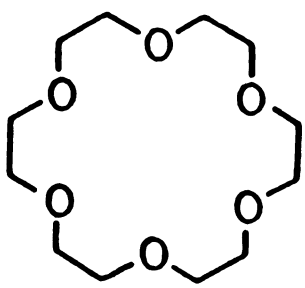

18 C 6

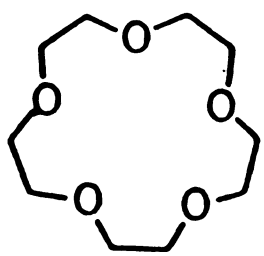

15C 5

Figure 1. Structural formulas of complexing agents.

the stability necessary to prevent the reduction of M^+ in the presence of the alkali metal anion.

The electrides [2, 5, 6, 7, 11, 17 - 21] contain the same type of cationic moiety as the alkalides, but in these salts, trapped electrons occupy all the anionic sites. Electrides with Li^+, Na^+, K^+, Rb^+, and Cs^+ complexed by various ligands have been synthesized.

A number of spectroscopic methods have been employed to study the properties exhibited by these new solids. Of particular interest are the electronic and magnetic properties, which provide the most information about the nature of the anionic species, and about how these interact in the solid to determine the properties of alkalides and electrides. Among the properties of interest shown by these compounds are semiconductivity [6, 8, 10, 25], photoelectron emission [10, 22], intense visible and near IR absorption bands [17, 18, 23], a wide spectrum of magnetic properties [21, 24], and exceptional chemical reducing power [12, 26].

Most frequently, alkalides and electrides are prepared by crystallization from amine and ether solutions that contain stoichiometric amounts of the desired alkali metals and complexants. It was, in fact, the study of similar solutions of the alkali metals in liquid ammonia, amines, and ethers that led to the discovery of alkalides and electrides. The following sections describe the nature of these solutions and the evolution of the research, from

the early solution studies, to the preparation and characterizaton of the novel solids.

1.1 Metal - Ammonia Solutions

All of the alkali metals dissolve in liquid ammonia to produce dark blue solutions [27]. The studies of these solutions, started by Sir Humphrey Davy in 1808 [28], have been aimed at identifying and characterizing the species that give rise to the unique properties exhibited. Yet, because of the lack of specific experimental information about the species present, the characterization has been difficult, and a number of models have been developed to explain the observed properties.

In liquid ammonia and other polar solvents, the alkali metals dissolve according to

$$M_{(s)} \rightarrow M^{+}_{solv} + e^{-}_{solv} \qquad (1)$$

The high solubilities of the metals are accounted for by the small size and large dipole moment of ammonia (dielectric constant = 23 at the boiling point of -33.4^{o}C [7]), and allow for the preparation of very concentrated metal solutions of the cation and the electron.

The solution properties range from electrolytic in dilute solutions to metallic in concentrated solutions with a nonmetal to metal transition occuring between 2 and 9

mole percent metal [29]. It is generally accepted that at low concentrations ($< 10^{-3}$M) the principal species in solution are solvated cations and solvated electrons [30, 31]. These species behave independently of each other, and the influence of the cation in determining the solution properties is essentially negligible. Evidence for this is obtained from the electron paramagnetic resonance (EPR) spectra of the solutions of potassium and sodium in ammonia [29]. The spectra of solutions with concentrations down to 0.001 mole percent metal show a strong, narrow singlet with a g-factor of 2.0012 $\pm$ 0.0002, independent of concentration and frequency, and close to the g-factor of the free electron at 2.0023 [32]. The amount of information available is not sufficient to yield the structure of the solvated electron, but several models have been proposed to describe it. The most commonly accepted models consider the electron to be trapped in a potential well formed by the orientation of polar solvent molecules in the vicinity. The electron is only weakly attracted to the polarization center and is free to move readily to regions of higher stability [4, 26]. This model was originally proposed by Ogg [33], and later developed extensively by Jortner and coworkers [34 - 35].

As the metal concentration in the solutions is increased, the cations are preferentially solvated because of their higher primary solvation energy. As a result, at high concentrations,there is a deficiency of ammonia

molecules with which to solvate the electrons, and solvated cations and conduction electrons become the principal species [12]. The transition to the metallic state can be monitored by the variaton in electrical conductivity and reflectance spectra. The plots of specific conductance vs. mole percent metal clearly show the onset of metallic conductivity. Reflectance spectra show a gradual change from the characteristic spectrum of the solvated electron in dilute solutions to the plasma type absorption of conduction electrons at higher concentrations [12].

One of the most striking properties of metal-ammonia solutions is their intense blue color, which assumes a bronze sheen as the metal concentration is increased. The absorption spectra show a very intense band, broad and asymmetric, with a maximum absorption at approximately 1,500 nm [6, 30]. This band is essentially independent of the metal in solution and has, therefore, been assigned to the solvated electron. The absorption maximum shifts to lower energies with an increase in concentration, making it necessary to extrapolate the data to infinite dilution to obtain the spectral features of the isolated solvated electron. A correlation of the peak position with bulk solvent properties has not been established. Nevertheless, studies of the absorption maxima of the solvated electron in a number of different solvents have shown a correlation with the solvent dependence of the charge-transfer to

solvent (CTTS) transitions of the halides I^- and Br^-[36, 37].

The study of solutions of the alkali metals in ammonia and other amine and ether solvents would be more common were it not for the powerful reducing ability of the solvated electrons and metal anions [12]. The solvated electron is the strongest reducing agent and irreversible reactions such as

$$e^-_{solv} + ROH \rightarrow RO^- + 1/2\ H_2 \qquad (2)$$

and

$$e^-_{solv} + RNH_2 \rightarrow RNH^- + 1/2\ H_2 \qquad (3)$$

as well as various chain reactions initiated by electron attachment and hydrogen atom abstraction can occur. In most cases, the decomposition reactions are autocatalytic; following the onset of decomposition the solutions degrade rapidly and completely. These problems limit the number of solvents that can be used to dissolve the metals. In ammonia, certain amines, polyethers and a few other solvents, the reactions of e^-_{solv} and M^-_{solv} with the solvent are slow enough to permit the formation and study of metastable solutions of the alkali metals [12]. In addition to a judicious choice of the solvent, it is necessary to eliminate all easily reducible impurities from

the solution media [29]. In order to obtain stable solutions, the vessels in which the experiments are to be carried out must be scrupulously clean and the solvents and complexants must be pretreated with good reducing agents. It is also necessary to work in vacuo or in inert atmospheres.

1.2 Solutions in Amines and Ethers

In addition to ammonia, several other solvents are known to dissolve the alkali metals in appreciable quantities [29]. While some of the species present in these solutions are the same as those found in ammonia, namely, solvated cations and solvated electrons, it is known that these solutions contain a variety of novel species. The number of solvents that can be studied is severely limited, however, by the drastic reduction in solubilities of the metals as compared with ammonia. The solvents that have been most extensively studied include methylamine, ethylamine, ethylenediamine, and hexamethyl phosphoric triamide (HMPA, with the formula $[(CH_3)_2N]_3PO$) [4, 7, 26]. Experimentally, it is observed that the solubility of the metals decreases markedly as the donicity or polarity of the solvent decreases, that is, the solubilities decrease in the progression NH_3, HMPA, $MeNH_2$, EDA, $EtNH_2$, $PrNH_2$, polyethers. The decrease in solubility with solvent donicity is largely caused by the decrease in

the free energy of solvation of the cation. In addition to being an effective solvating agent, a potential solvent must, for solution stability purposes, be one that can be readily purified and be kinetically inert to reduction [30]. For the latter reason many polar solvents such as water and alcohols are excluded. The solubility in a given solvent generally increases for the heavier alkali metals. This progression can be explained in terms of the combined effects of the lattice energies of the metals, their ionization potentials, and the solvation energies of the gaseous cations. Lithium is a special case, with solubilities that can be greater than or smaller than the other alkali metals depending on the solvent used [12].

The range of solvents used to study alkali metal solutions was greatly expanded [38] by the use of complexing agents of the crown ether and cryptand [3, 30, 39] type, which can increase the solubility of the metals by as much as a factor of 10^6. The use of complexants in the study of solutions in amines and ethers will be described in Section 1.3.

The species present in amine and ether solutions are determined by the following equilibria [39]

$$2M_{(s)} \rightleftharpoons M^+_{solv} + M^-_{solv} \qquad (4)$$

$$M^-_{solv} \rightleftharpoons M^+_{solv} + 2e^-_{solv} \qquad (5)$$

$$M^+_{solv} + e^-_{solv} \rightleftharpoons M_{solv} \qquad (6)$$

In strongly solvating media such as ammonia, the equilibria shift toward the cations and solvated electrons. In less polar solvents, the species present interact more strongly and are thus more highly associated than in ammonia. These strong interactions give rise to new species; namely, the monomer, M, and the alkali metal anion, M^-.

One of the experimental techniques that has provided extensive information about the species present in these solutions is optical spectroscopy [6, 12, 30, 39, 40]. The transmission spectra of the solutions generally exhibit two intense optical absorption bands that can be classified according to whether they show a metal dependence. One of the bands appears in the infrared region of the spectrum - between 1,200 and 2,000 nm - and is independent of the metal present in the solution. It is similar to the band exhibited by metal solutions in ammonia and has been attributed to absorption by the solvated electron. This assignment was based on the correlation between the presence of this infrared absorption band and that of a strong singlet, of corresponding intensity, in the EPR spectrum of the solution. Additional evidence was obtained from pulse radiolysis studies. For a number of years, radiation chemists had been able to produce and detect the solvated electron in dozens of solvents and solvent mixtures, including hydroxylic, amine, and ether solvents,

by using pulse radiolysis and similar techniques [41 - 43]. The band shapes and peak positions of the solvated electron band for both ammonia and ethylenediamine are independent of the method of preparation, pulse radiolysis or metal solutions, indicating that the same species is produced by either method [43]. In general, the features of the solvated electron spectra do not change appreciably from one solvent to another; there are only slight variations in the band shapes. The position of the absorption maximum in a given solvent shifts to lower energies with an increase in temperature or concentration, and shifts to higher energies with an increase in pressure [12]. As was mentioned earlier, the variation of the position of the absorption maximum of the solvated electron in a number of solvents correlated well with that of the halide ions, suggesting the transitions are similar to the CTTS transitions of the ions [36, 37].

In addition to the IR band, an absorption band with a metal-dependent peak position can be observed for solutions of all the alkali metals except Li. The optical spectra for solutions of Li, Na, K, Rb, and Cs in ethylenediamine [40] are shown in Figure 2. The wavelengths of maximum absorption are observed at 660, 850, 900, and 1,020 nm for solutions of Na, K, Rb and Cs, respectively. In all cases, the absorption band is broad, structureless and strongly asymmetric on the high energy side. It should be noted that the solvated electron absorption appears as a shoulder

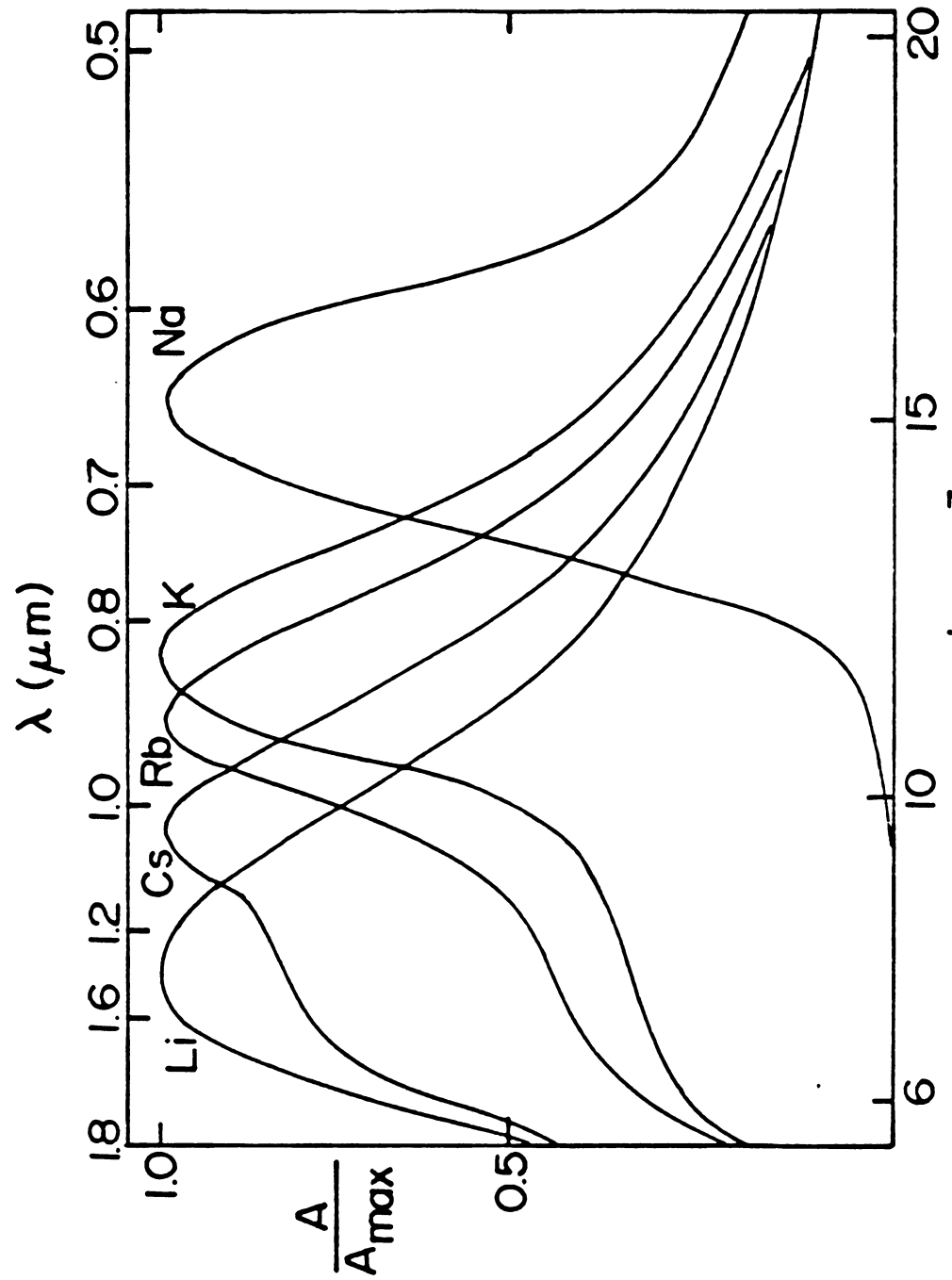

Figure 2. Optical spectra of metal solutions in ethylenediamine [40].

in the IR region of the spectra of K, Rb, and Cs. The ratio of the intensity of this absorption to that of the metal-dependent band is determined by the solvent, the metal and the concentration. As was the case with solubility trends, the lower the polarity of the solvent, the larger the intensity of the metal-dependent band compared to that of the solvated electron [4]. The same progression of solubility and optical absorption applies to the metals - with the exception of lithium - in a given solvent. The relative intensity of the solvated electron band with respect to the metal band increases in the order Na < K $\cong$ Rb < Cs. In lithium solutions only one band is observed which coincides in position and shape with that of the solvated electron produced by flash photolysis or pulse radiolysis of the same solvent [6].

The effects of temperature and solvent on the metal-dependent absorption bands led Matalon, Golden and Ottolenghi to propose in 1969 [44] that the absorbing species were alkali metal anions and that the observed bands were due to charge-transfer-to-solvent transitions of these anions. Some of the characteristics of CTTS transitions are: the pronounced dependence of the position of the absorption maximum upon solvent, the shift of the maximum to lower energies with an increase in temperature, the correlation between the shift of the peak position with solvent and the temperature coefficient, and the correlation between the position of the absorption maximum

and the size of the anion, with a shift to lower energies for larger ions. All of these characteristics have been observed in the absorption bands of the alkali metals in amines and ethers. The assignment of alkali metal anions as the absorbing species was also in agreement with the observed diamagnetic nature of the species - only weak ESR spectra were observed in solutions which only showed the metal-dependent band [30]. M^- would be expected to exist in a spin-paired ground state.

Although the evidence in favor of the anionic nature of the species M^- was very convincing, alternate models for this species had been previously proposed and could not be ruled out. Among these models were an ion pair consisting of the solvated cation and the dielectron, $M^+ e^=_2$, a solvent-shared triple ion, $e^- M^+ e^-$, and a solvated cation with two electrons in expanded orbitals [45]. The interactions of the electrons in these species could be strong enough to give metal dependent bands in the optical spectra, and the species would show diamagnetic behavior. All of these species show solvation of the cation.

The second novel species present in the solutions of amines and ethers is the monomer, a species of stoichiometry M, that can be described as a strongly interacting electron-cation pair. In the monomer, there is appreciable electron density at the metal nucleus with spin I, and the lifetime is long enough to produce a hyperfine pattern of 2I + 1 nearly equally spaced lines in the EPR

spectrum [26]. The separation of the lines - the hyperfine splitting- is a direct measure of the average contact density of the electron at the nucleus. When this splitting is expressed as a percentage of that of the free gaseous atom, it gives the "percent atomic character" of M. The percent atomic character varies with solvent and temperature and can assume values ranging from a few percent to approximately 50%. However, EPR intensities show that the monomers constitute only a small fraction of the total dissolved metal [4].

1.3 Role of Complexing Agents

The use of cation complexing agents was introduced in 1970 with the objective of increasing the solubility of the alkali metals in certain amines and ethers, thus expanding the number of solvents that could be studied [38]. The complexants used were of two kinds: crown ethers and cryptands. The first crown ether to be used for alkali cation complexation was synthesized by C. J. Pedersen in 1962 [15 - 16]. The most striking feature exhibited by this compound was its ability to form stable complexes with the alkali and alkaline earth cations. Beause of the interest generated by this unusual property, a major effort was undertaken to prepare all sorts of polyethers and, by the end of 1968, sixty authentic crown ether compounds had been synthesized [46]. At the same time, in France, J.-M.

Lehn and co-workers had completed the synthesis of some diazapolyoxamacrobicyclic compounds which they called cryptands [13, 14]. These showed a potent ability to complex alkali and alkaline earth cations as well.

The synthesis of a variety of crystalline complexes followed the preparation of the new complexing agents, and structural studies began in 1970 [47]. It was found that the stoichiometry, structure, and stability of a complex are determined largely by the match between the size of the cavity of the ligand and the cation diameter [46]. The most stable complexes tend to be those in which there is a close fit of the cation and the cavity size. Since these complexants are flexible, they can change their conformations slightly, as necessary, to best fit the cation size. The cation is held in the cavity by the electrostatic attraction between its positive charge and the negative dipolar charge on the complexing oxygen atoms which are, in most cases, symmetrically arranged around it in the polyether ring. The maximum of the charge density from the oxygens is directed toward the center of the ring, thus maximizing the attraction to the cation.

Upon adding a complexant to solutions of the alkali metals in amines and ethers, the complexation of the cation

$$M^+ + C \rightleftharpoons M^+C \qquad (7)$$

takes part in the equilibria present in the solution [3], and has a strong effect on the relative concentrations of all the species. The formation of M^+C causes a shift to the right in equilibria (4) and (5),

$$2M_{(s)} \rightleftharpoons M^-_{solv} + M^+_{solv} \qquad (4)$$

$$M^-_{solv} \rightleftharpoons M^+_{solv} + 2e^-_{solv} \qquad (5)$$

$$M^+_{solv} + e^-_{solv} \rightleftharpoons M_{solv} \qquad (6)$$

and shifts (6) to the left. As a result, the solubility of the metal is dramatically increased. For example, the solubility of sodium in ethylamine is less than 10^{-6}M, as evidenced by the absence of a blue color when the solvent is allowed to contact a metal film. By adding 18-crown-6 to the solutions, concentrations as high as 0.4 M have been obtained [2] to give a solubility enhancement of at least five orders of magnitude!

The high alkali metal concentrations achieved by adding complexants to the solutions made possible the use of nuclear magnetic resonance techniques [45, 48, 49] to study the species present. Extrapolation of NMR studies of solutions of sodium and C222 in various solvents to low temperatures indicated that the release of Na^+ from the cryptand cavity is slow at low temperatures - of the order of a minute or longer at -78° C [48]. For this reason, two

separate resonances, for Na^+C222 and Na^-, could be observed by ^{23}Na NMR. The ^{23}Na NMR spectra of solutions of sodium salts provide information about the environment of the sodium ion. The chemical shift of the solvated cation from the gaseous ion is a measure of the interaction of solvent molecules with the filled outer p-shell of Na^+ [45]. The magnitude of the observed paramagnetic shift, -45 to -75 ppm, correlates very well with the ability of the solvent to donate electron density to the cation. By contrast, the peak position for Na^+C222 was found to be nearly independent of the solvent and appeared at the same chemical shift as in solutions of salts such as $Na^+C222Br^-$. This is in accord with the fact that, in Na^+C222, the cation is enclosed within the cryptand cavity and is thus separated from the solvent. Most significant, however, was the observed absence of a solvent-induced paramagnetic shift for Na^- and the narrowness of its line. Furthermore, the chemical shift of Na^- is not only independent of solvent, but is also nearly the same as that calculated for Na^- in the gas phase [45]. As was stated, the paramagnetic shifts are caused by the orbital angular momentum introduced by the interaction of solvent electron density with the outer p orbitals of the ion. The absence of a shift for Na^- demonstrated that its 2p orbitals are well shielded from the solvent by the presence of the filled 3s orbitals [45]. The width of the ^{23}Na resonance line is, in most cases, determined by quadrupole coupling

of the nucleus to its surroundings and by the rate of modulation of this coupling via solvent motion. The quadrupole coupling is small when the ion is in a symmetric environment. The extremely narrow width of the Na^- line is evidence for its high spherical symmetry and large radius. These ^{23}Na NMR results provided conclusive evidence that Na^- is a large centrosymmetric anion with two electrons in the outer s orbital. It was now possible to rule out the alternative models for the species M^- -the "tight ion cluster", $e^- M^+ e^-$, the "ion pair with the dielectron", $M^+ e_2^=$, and the solvated cation with two electrons in expanded orbitals [45].

By using equimolar amounts of metal and the appropriate complexant, it is possible, in favorable cases, to drive reactions (4) and (5) almost completely to the right to obtain complexed cations and solvated electrons as the major solution species [12].

$$M_{(s)} + C \rightleftharpoons M^+C + e^-_{solv} \qquad (8)$$

On the other hand, if two moles of metal are used per mole of complexant, the effective reaction is

$$2M_{(s)} + C \rightleftharpoons M^+C + M^-_{solv} \qquad (9)$$

Thus, a high concentration of M^- can be achieved. As can be seen, the addition of the complexing agents allows a

measure of stoichiometric control over the composition of the solutions.

In addition to enhancing the solubilities of the metals and providing stoichiometric control of the solutions, the crowns and cryptands played a key role in stabilizing the species present. By encapsulating the cation in a cavity, its ability to react with the reducing species present in solution was greatly inhibited [2]. This resulted in the solution stabilization necessary for the synthesis of solid alkalides and electrides.

1.4 Alkalides and Electrides

The first solid salt of an alkali metal anion was synthesized in 1974 [2] from a solution of ethylamine with a Na/C222 molar ratio of two. The rapid evaporation of the solvent left deposits of metallic-looking gold-colored films on the walls of the vessel. Slow cooling of the solutions resulted in the growth of shiny, gold-colored crystals of $Na^{+}C222\ Na^{-}$. Elemental analysis and the determination of the crystal structure proved that this was, indeed, the first alkalide. Although the crystals have a relatively high melting point of 73° C [10], they are temperature sensitive and decompose irreversibly when held at high temperatures, even for a short time. They are also extremely reactive toward air and moisture and, consequently, must be handled either in evacuated vessels or in inert atmospheres.

In spite of these difficulties, single crystals of $Na^+C222\ Na^-$ can be obtained with relative ease and it was possible to fully characterize this compound. The crystal structure was found to consist of closest packed cryptated cations with the sodium anions in the octahedral holes as illustrated in Figure 3. The unit cell is hexagonal in the space group R32 with a=8.83 Å and c=29.26 Å [2]. The distance between Na^+ and Na^- is 7.06 Å. The spherical ion radius of the sodide can be estimated to be about 2.4 Å, by taking into account that the cryptated cations are essentially in van der Waals contact. The shortest Na^- to Na^- distances are 8.83 Å in the packing plane perpendicular to the threefold axis of the cryptate and 11.0 Å for sodides in adjacent planes. Thus, anisotropy of the electrical properties can be expected. The configuration of the Na^+C222 moiety, illustrated in Figure 4, was found to be virtually identical with that of $Na^+C222\ I^-$[50]. The cryptand cage exhibits threefold symmetry with an antiprismatic arrangement of the ether oxygens. Additional similarities between the sodide and the iodide are found in the placement, distances from other atoms and size of the anions.

Powder conductivity measurements indicate that $Na^+C222\ Na^-$ shows the temperature-dependent electrical conductivity expected for a semiconductor of band gap 2.4 eV. The solid is diamagnetic as indicated by its EPR spectrum and static susceptibility [6].

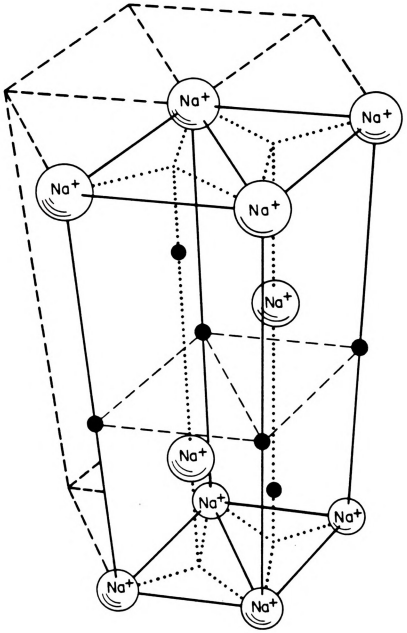

Figure 3. Packing of $Na^{+}C222$ and Na^{-} in $Na^{+}C222Na^{-}$ [2].

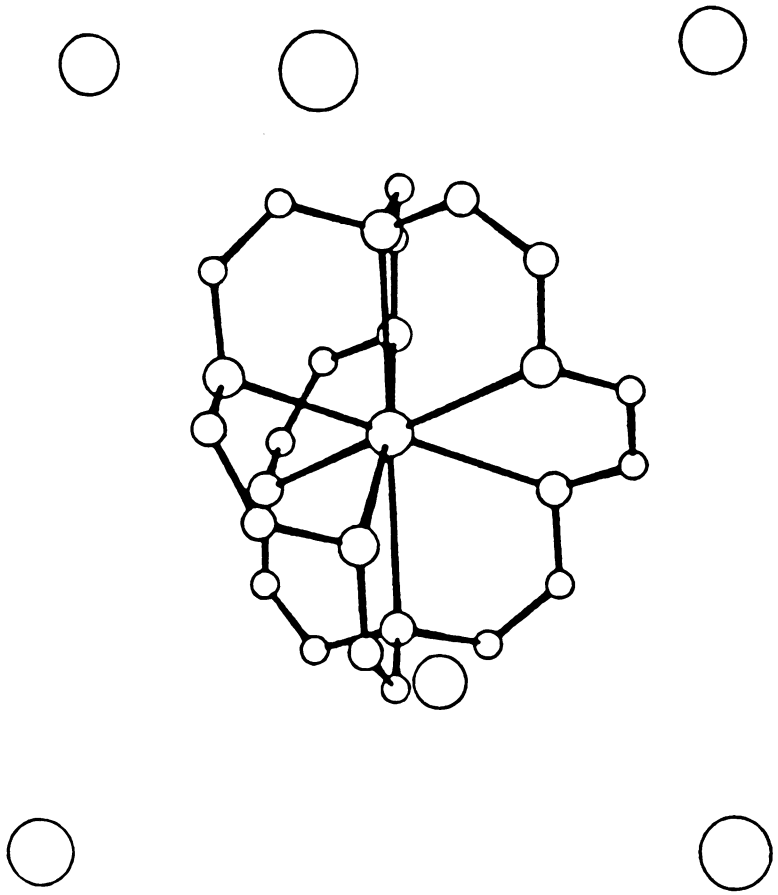

Figure 4. Structure of the $Na^{+}C222$ moiety in $Na^{+}C222Na^{-}$ [2].

Films of $Na^+C222\ Na^-$ obtained by evaporating the solvent from methylamine solutions show photoconductivity for photon energies above 1.5 eV, with a low quantum yield (10^{-3}) [10, 22]. Although the results of this study are not completely understood at this time, it has been proposed that the photoconductivity is a surface phenomenon resulting from the excitation of trapped electrons rather than bulk photoconductivity from photoexcitation of Na^-.

Following the synthesis of the first solid sodide, research efforts were directed toward the synthesis of new alkalides and of electrides, with stoichiometry $M^+C\ e^-$. Initially, no other crystalline compounds could be prepared. However, it was relatively easy to obtain solid films by the rapid evaporation of solutions containing different stoichiometries of Na, K, Rb, or Cs and complexing agents [3]. If the solutions contained high concentrations of M^-, the films appeared blue by transmitted light and varied in color from gold to dark bronze by reflected light, depending on the metal. Analogously, films from solutions with high concentrations of solvated electrons appeared blue by transmission and very dark blue-black by reflected light [6].

In order to obtain the absorption spectra, the films were prepared on the windows of quartz optical cells [6, 17, 18, 23]. The absorption bands could then be used to identify the particular alkalides present, and to point out the combinations of metals, complexants and solvents that

would yield solids with high trapped electron content. The spectra also provided information about the stability of the solids. The absorption spectra of the solvent-free films prepared from solutions with a 2:1 metal-to-complexant molar ratio show bands at 15,400, 11,900, 11,600 and 10,500 cm^{-1} for Na^-, K^-, Rb^-, and Cs^- [17], respectively, which are similar in position and width to those observed in solutions - 15,400, 12,000, 11,200, 9,800 cm^{-1}, respectively, in ethylenediamine [40]. However, for films of stoichiometry $M^+C\ N^-$, prepared from solutions that contained more than one alkali metal, the peak position corresponding to the anion shifted considerably depending upon the host crystal. For example, the Na^- absorption in films of $K^+(18C6)\ Na^-$ appears "red-shifted" by 2,700 cm^{-1} from that in $Na^+C222\ Na^-$[23]. This can be explained by considering that the absorption is due to an ns -> np transition of M^- [12]. Because the excited state wavefunction is expected to be quite diffuse, the transition energy will depend upon the environment of M^-, and, thus, yield the variations observed for different compounds.

By using equimolar amounts of potassium and C222 in methylamine, deep blue, solvent-free films were obtained [17]. The optical transmission spectrum showed a single, strong band in the infrared, centered at 7,400 cm^{-1}, very similar to that observed for solutions that contain high concentrations of solvated electrons. Because the films

are free of solvent, the bands could only be attributed to absorption by electrons trapped in the solid [6], and $K^+C222\ e^-$ became the first known electride. The EPR spectrum of powders of the same composition showed a very intense narrow line at the free electron g-value, also indicative of the presence of trapped electrons [2, 6]. The static susceptibilities showed the solid to be strongly paramagnetic.

As the optical studies were expanded to include an increased number of metal and complexant combinations with the stoichiometry $M^+C\ e^-$, it became clear that the electrides could exhibit two types of electronic behavior [25]. Some electrides appeared to contain locally trapped electrons and exhibited the characteristic absorption maxima in the near-infrared, while others showed plasma-type absorption and microwave conductivity indicating delocalization of the electrons. An example of the first type of behavior was obtained from films of Cs with 18C6. Films formed from solution with metal-to-complexant ratios, R, of 2, 1, 0.5, and 0.1 all showed a single band at 6,400 - 6,700 cm^{-1}. An important feature of this band was a sharp drop in the absorbance to nearly zero on the low energy side of the band [23].

The other type of electride behavior was represented by $K^+C222\ e^-$. Detailed optical studies of this compound revealed a time-dependence of the absorption bands. Films prepared with a metal-to-complexant ratio of 1 showed

initially two peaks: a peak of K^- at 11,900 cm^{-1}, and another peak at 5,600 cm^{-1}. Upon standing, the K^- peak decayed to a shoulder and the absorption of the trapped electron grew. The final spectrum exhibited substantial absorbance into the infrared, very similar to the plasma absorption of concentrated metal ammonia solutions, which suggested delocalization of the trapped electron. Additional studies on powders of this compound - microwave conductivity and asymmetry ratio measurements by EPR [24] - also indicated substantial electron delocalization and a tendency toward metallic character. Another electride, prepared with Li metal and cryptand-211, exhibited behavior which was strongly dependent on the metal-to-complexant ratio used. At $R << 1$, the optical, EPR and magnetic susceptibility data indicated that electrons are locally trapped in two nonequivalent sites and that spin pairing occurred as the temperature was reduced. With $R = 1.5$, only a single trapping site seemed to be involved and with R=2, plasma-type optical absorption, indicative of the onset of metallic character, was observed [21].

As the foregoing discussion suggests, the optical studies of solvent-free films provided much information about the nature and stability of solid alkalides and electrides and, initially, constituted the principal means of identifying the species present in the solids [6, 8, 9, 11, 17, 18, 19, 51]. However, as the number of new alkalides and electrides increased, it became clear that

the film absorption spectra could not provide an unambiguous identification in every case. The procedure for preparing the films involved dissolving the metals and the complexant, or the crystals to be studied, followed by fast evaporation of the solvent [9, 23]. There were some disadvantages inherent to this procedure. Among them were; the formation of films of nonuniform thickness, the lack of knowledge about the thickness and the time-dependent changes that occurred because of solid state reactions [12]. Furthermore, it was possible to prepare heterogeneous films which contained the solid of interest as well as unspecified residues of other nonvolatile solutes present in the original solution. The presence of several species in the solutions often led to complex film spectra and the appearance of new or shifted bands [10].

Another source of problems was the observed sensitivity of the peak position of an anion to the surroundings. For example, the spectrum of a film of the compound with stoichiometry KNa18C6 [51] showed a broad peak at 13,300 cm^{-1}. This peak appears red-shifted by 2,700 cm^{-1} from the Na^- band in $Na^+C222\ Na^-$ and blue-shifted by 2,100 cm^{-1} from the K^- peak in $K^+C222\ K^-$ and 1,100 cm^{-1} from that in $K^+18C6\ K^-$. It is clear that the absorption spectrum alone cannot provide an identification of the anion in this salt.

By 1983, the methodology required to synthezise and analyze crystalline alkalides was fully developed. A

number of them had been prepared and an in-house analysis scheme, which allowed precise determination of the stoichiometry of the crystals, had been developed [9]. In addition, a crystalline solid of stoichiometry Cs(18C6), suspected to be an electride, had been prepared [19]. As a result, the need for reliable methods of identifying the species present in the crystals became imperative.

The ability of alkali metal NMR spectroscopy to identify the species present in solutions was well known, and preliminary studies of ^{23}Na and ^{133}Cs solid state magic angle spinning NMR spectra promised to be equally helpful in identifying species present in crystalline and powdered samples of alkalides and electrides. For instance, the study of crystals of KNa18C6, RbNa18C6, and CsNa18C6 showed that the first two salts contained Na^- but not Na^+ and that the third contained both $Cs^+$and Na^- [51]. Rubidium and potassium NMR studies were not feasible at the time.

In addition to finding reliable methods of identification, a major goal was to obtain structural information about the new solids. In spite of the large number of compounds which had been synthesized, the preparations had failed in to yield crystals of sufficiently high quality for single crystal X-ray diffraction studies. The inability to obtain high quality single crystals was due, in part, to the intrinsic thermodynamic instability of the metal solutions from which the solids were to be crystallized [8]. Additional

problems were caused by the sensitivity of the alkalide and electride crystals to air, moisture, and high temperatures ($T \geq -20^{\circ}C$) and the autocatalytic nature of their decomposition reactions.

1.5 Objectives of the Present Work

A major objective of the present work was to obtain structural information about alkalides and electrides. This endeavor was approached in two ways: (a) through the use of a structural characterization technique that could utilize the polycrystalline solids which could be easily produced and (b) through the development of new, improved methods of crystallization and handling of single crystals for X-ray diffraction studies.

The first approach involved the use of the X-ray absorption techniques of X-ray absorption near edge structure (XANES) and extended X-ray absorption fine structure (EXAFS) to obtain structural information on polycrystalline samples of alkalides and electrides. The strength of the combined use of EXAFS and XANES in structural characterization has been demonstrated recently in a number of studies in which they have permitted structural determinations not possible by diffraction techniques [52]. EXAFS spectroscopy can provide structural information even if single crystals of the material to be studied are not available [53, 54]. Moreover, by using the

intense radiation from synchrotron sources, a whole spectrum can be recorded within 10 to 20 minutes, eliminating the need to expose the sample to the experimental conditions over an extended period of time.

For feasibility purposes, studies were initiated with the rubidium K-edge absorption and, thus, were limited to the study of those compounds that contained rubidium. With this in mind, the synthesis of three new rubidides, $Cs^{+}(18C6)_2Rb^{-}$, $K^{+}C222\ Rb^{-}$, and $Li^{+}C211\ Rb^{-}$, was successfully carried out. In addition, the necessary model salts were prepared and characterized. The structure of one of them, $Rb^{+}18C6\ Br^{-}2H_2O$, was determined by using single crystal X-ray diffraction methods.

The use of XANES spectroscopy as an identification tool for rubidium-containing alkalides and electrides was also investigated. It has been known for some time that the features in the region immediately before and after the absorption edge are rich in information about the electronic structure and environment of the absorber [55].

The single crystal growth studies focussed on optimizing crystallization conditions. Solution stability studies had demonstrated that enhanced stability could be obtained through the use of tertiary amines and other solvents which have neither β hydrogens nor acidic hydrogens [10]. Thus, very stable solutions are obtained in solvents such as dimethyl ether (Me_2O) and trimethylamine (Me_3N). These, and other solvents, in

various concentration ratios, were used to prepare single crystals of alkalides and electrides. The methodology for handling the single crystals of alkalides and electrides was also developed. This made possible the determination of the structure of a sodide, $Rb^{+}(15C5)_{2}Na^{-}$, by using single crystal X-ray diffraction.

CHAPTER TWO

EXPERIMENTAL

2.1 Glassware Cleaning

As stated in Chapter 1, to successfully prepare and handle alkalides and electrides, it is essential to work with rigorously clean glassware in order to prevent solution and sample decomposition. The following procedure was used to clean the glassware utilized throughout this work. First, the items were rinsed with a hydrofluoric acid cleaning solution consisting of 5% hydrofluoric acid (28 M stock solution), 33% concentrated (16 M) reagent grade nitric acid, 2% acid-soluble detergent, and 60% distilled water by volume. Following this rinse, the glassware was quickly rinsed at least six times with distilled water. Next, the vessels were filled with aqua regia (3:1 mixture of HCl and HNO_3), and allowed to stand overnight. The mixture was then poured out and the vessels were thoroughly rinsed, first with distilled water and then with conductance water. Finally, the vessels were dried overnight in an oven at 125^{o} C.

2.2 Vacuum Lines and Anaerobic Techniques

High vacuum and/or inert atmospheres were required for the syntheses and handling of alkalides and electrides. Each vacuum line consisted of an all glass manifold and a liquid nitrogen trap as described by Van Eck [58]. Most of the inert atmosphere work was done in a helium atmosphere dry box (Vac Atmospheres Co. Model DLX-001-S-G Dri-Lab). In addition, polyethylene glove bags (from I^2R) were used to transfer the samples into the cells used for physical measurements such as optical spectra, EPR spectra, and conductivities.

2.3 Materials

2.3.1 Complexing Agents

Cryptand [2.2.2] or C222 (IUPAC: 4, 7, 13, 16, 21, 24-hexaoxa-1,10- diazabicyclo [8.8.8] hexacosane, m.p. 68^{o} C). C222 was purchased from Fluka Chemical Corporation and sublimed under high vacuum at 95^{o} - 100^{o} C. It was stored in the drybox under a helium atmosphere.

18-Crown-6 or 18C6 (IUPAC: 1, 4, 7, 10, 13, 16 - hexaoxacyclooctadecane, m.p. 38-39^{o} C). 18C6 was purchased from Aldrich Co. and was recrystallized from warm (75^{o}C) acetonitrile. The recrystallized crown ether was dried

under vacuum. It was then sublimed under high vacuum at 60^{o}-65^{o} C and stored in the inert atmosphere glove box.

Cryptand [2.1.1] or C211 (IUPAC: 4, 7, 13, 18 - tetraoxa - 1, 10 - diazabicyclo-[8.5.5]eicosane). C211 was purchased from PCR Research Chemicals, Inc. The C211 was purified by following the procedure of Landers [56] of vacuum distillation at 65-68^{o} C in semidarkness. After distillation, the material was stored in the inert atmosphere box. Alternately, the material was purified in a special chamber in the synthesis vessel just prior to the start of a synthesis.

2.3.2 Metals

Lithium metal (99.99% purity) was purchased from Automergic Chemical Co. For the syntheses, small pieces of the desired weight were cut with a scalpel inside the drybox. The surface of the pieces was carefully peeled off to remove all oxide; only shiny, silver colored pieces were used. The pieces were weighed with a Mettler AC 100 balance and loaded into the synthesis vessel while still inside the drybox.

Sodium (99.95%), potassium (99.95%), and rubidium (99.93%), in five gram breakseal ampoules under argon gas, were purchased from Alfa Ventron Products. Cesium metal was obtained as a gift from Dow Chemical Co., and had been previously transferred into sealed glass ampoules with breakseals. The metals were transferred from their

original containers into evacuated tubes of known inner diameter by vacuum distillation as described by Issa [57].

2.3.3 Solvents

Methylamine (Matheson) was stirred over calcium hydride for at least twelve hours. The solvent was then frozen to liquid nitrogen temperatures and the system was evacuated to 10^{-5} torr. At this point, the solvent was thawed and subsequently frozen again. These freeze-pump-thaw cycles were repeated several times, until no significant change in pressure was observed after two successive cycles. The solvent was then distilled into a bottle containing Na-K (1:3 ratio) alloy. The blue color obtained should last for at least 24 hours. This procedure was followed with another set of freeze-pump-thaw cycles, and transferred to another bottle with fresh Na-K alloy. If the blue color persisted for more than 24 hours, the solvent was distilled into a stainless steel storage cylinder (from Whitey Co.).

The same procedure was used in the purification of isopropylamine (2-aminopropane, from Matheson), dimethylether (Matheson), diethylether (anhydrous, Mallinckrodt, Inc.), and trimethylamine (Matheson). For these solvents, however, it was necessary to use benzophenone along with the Na-K alloy. The violet-blue solution of the benzophenone ketyl and dianion served both as a drying agent and as a dryness indicator.

2.4 Synthesis

The preparation of crystalline alkalides and electrides is difficult due to the thermal instability of the solutions and the solids, and their high sensitivity to the presence of reducible compounds. In order to isolate the solids, highly specialized glassware had to be designed [58]. It was essential that the vacuum-tight vessels provide chambers for every stage of the synthetic procedure - from starting materials to isolated crystalline products. The vessels used originally were subsequently slightly modified by practically every investigator to suit the specific demands of each compound prepared. The vessel used throughout most of this work is illustrated in Figure 5. The dimensions of this vessel had been reduced slightly from those used previously, to allow it to fit in the entry port of the drybox.

The first step in a synthesis is the introduction of the starting materials. Ampoules containing known metal volumes were scribed with a glass-cutting knife and brought into the vessel through sidearm A. The sidearm was sealed by using a glass cap connected to the vessel by either a small piece of heat shrinkable tubing (Flo-Tite Tubing from Pope Scientific Co.), or a stainless steel "Ultra-Torr" connector (from Cajon). Following the introduction of the metal ampoule, sidearm B was sealed by attaching a glass cap with an "Ultra-Torr" connector, and the vessel was

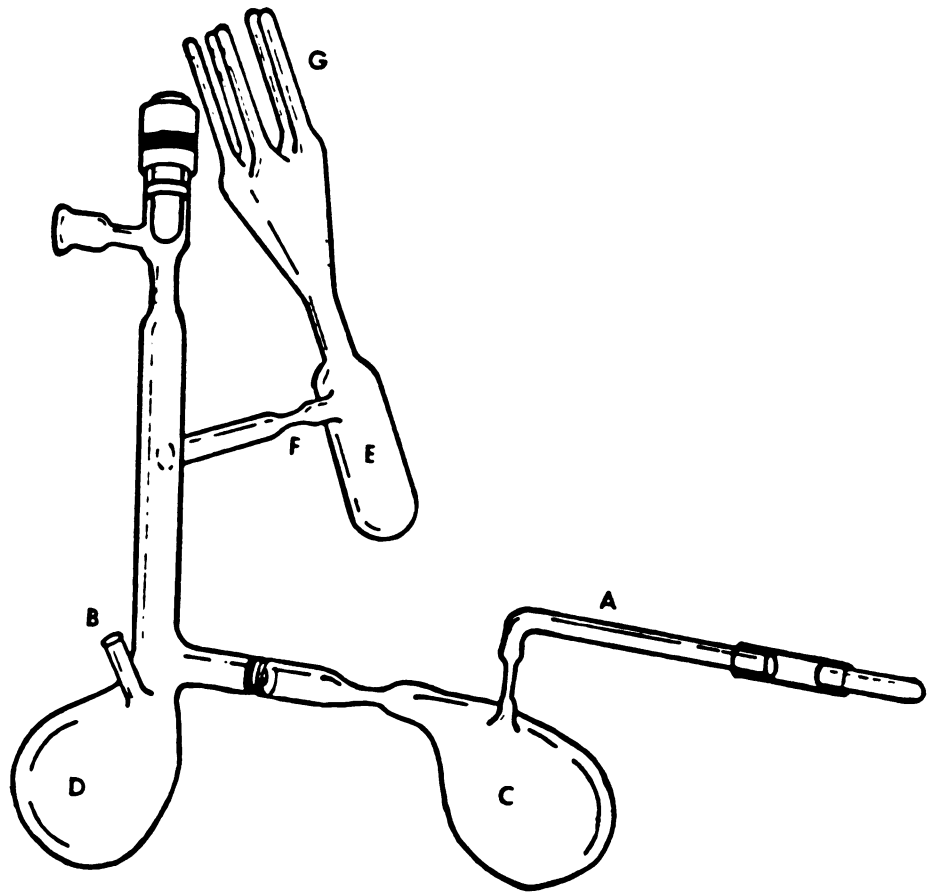

Figure 5. Vessel used in the synthesis of alkalides and electrides.

placed on the vacuum line for evacuation. The metal ampoule was subsequently opened by breaking at the scribe mark. When using the flexible heat shrinkable tubing to seal sidearm A, this was accomplished by simply placing the ampoule in the portion of the sidearm with the flexible tubing, and bending the tube at the scribe mark, until it was opened. If using the "Utra-Torr" connector, the vessel was introduced in the drybox; there the ampoule was removed from the sidearm, opened at the scribe mark, and placed back in the sidearm, which was capped again with the connector. While in the drybox, the necessary amounts of complexant were weighed and poured in through sidearm B. This sidearm was then capped, and the apparatus removed from the drybox and evacuated to 10^{-5} torr. Both sidearm B and the capped portion of sidearm A were then flame sealed-off. The metals (with the exception of lithium) were then distilled by using a hand torch to form a mirror on the walls of vessel C. Subsequently, sidearm A was flame sealed off. The solvent was then vacuum distilled from a storage tank into chamber D. The solvent-complexant mixture was stirred to dissolve as much of the complexant as possible. The solution was poured into the metal chamber C and stirred to dissolve and complex the metal. At this stage it was important to carefully control the temperature to maintain solution stability, while at the same time allowing efficient and prompt dissolution of the metal. Once the metal had been completely dissolved, the

solution was poured back into chamber D, and some of the initial solvent was distilled out. The amount removed varied, depending on the compound being prepared and on whether or not single crystals of the material were desired. Next, one or two cosolvents were added and the temperature was lowered. This part of the preparation is of critical importance if crystalline samples are desired. To grow large crystals it is often necessary to start out with dilute solutions. It is essential, however, that the solutions not be so dilute that extremely long crystallization times are required. Experience indicates that it is essential to recover the crystals within the first four days following the start of a synthesis. After longer crystallization periods, the tendency for decomposition is very high.

Once the crystals were obtained, the solvent was poured into chamber C and quickly distilled out of the synthesis vessel into a waste bottle. A washing solvent was added, and the crystals were poured into chamber E. There, they were washed by repeated distillations of the solvent into E followed by pouring back into chamber D. After washing, the solvent (in chamber D) was frozen at 77 K and the synthesis vessel was placed back on the vacuum line. The crystals were dried for at least one hour under dynamic vacuum. Following this, a flame seal-off was made at constriction F. The crystals were then poured into

individual sample tubes, G, which were separately sealed off.

2.5 Analysis

The analysis scheme included measurement of the volume of hydrogen released when the sample was decomposed by a controlled reaction with water. For alkalides this reaction is,

$$M^+C\ N^- + 2H_2O \rightarrow M^+C + N^+ + 2OH^- + H_2 \quad (10)$$

The volume of hydrogen released is directly proportional to the number of reducing equivalents in the sample. Thus, electrides produce only half as much hydrogen per mole as alkalides. The analysis also included titration of the produced hydroxide with a standardized HCl solution, analysis of the metal content by flame emission spectroscopy, and analysis of the crown or cryptand content by ^1H NMR analysis. The steps followed in carrying out the analysis have been described in detail by Van Eck [58].

2.6 Characterization Methods

2.6.1 Optical Spectra

Optical absorption spectra of thin, solvent-free films were obtained by using a Beckman DK-2 double beam recording spectrometer. The reference beam passed through air. The

cell compartment had been previously modified to allow temperature control over the range of -65°C to room temperature. This is achieved by flowing nitrogen gas consecutively through a set of copper coils chilled with liquid nitrogen and then through the cell. The temperature is controlled by adjusting the rate of nitrogen gas flow, and is measured by a copper-Constantan thermocouple placed near the sample and connected to a digital thermometer (Digicator from Omega). The spectra were recorded from 4,000 cm^{-1} (2,500 nm) to 25,000 cm^{-1} (400 nm).

The thin films were prepared and studied in the vessel shown in Figure 6. Because the dilute solutions of lithium, potassium, rubidium and cesium are prone to contamination by sodium abstraction from glass, all portions of the vessel that would be in contact with the solutions or the films were constrcted of fused silica. The procedure used to prepare the films has been previously described [58].

The spectra obtained in this way were normalized to a scale of 0.0 to 1.0 by subtracting a baseline correction - the spectrum of the empty cell - and scaling the measured absorbance at the peak to a value of unity. Data were calculated at 500 cm^{-1} intervals. It was necessary to use a new baseline correction for each run.

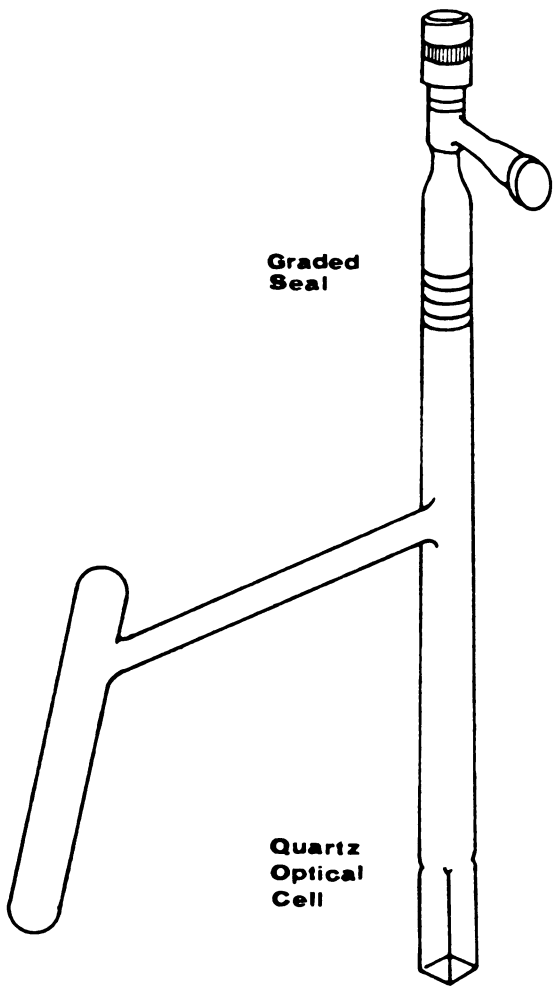

Figure 6. Vessel used in the optical spectroscopy studies of alkalides and electrides.

2.6.2 Electron Paramagnetic Resonance

X-band EPR spectra were measured on a Bruker Model 200 EPR spectrometer over the temperature range of 3.6 to 100 K. These temperatures were achieved by using a continuous-flow liquid helium system (Oxford Instruments Co., Ltd., Model ESR 9). Digital temperature readout was based on a thermocouple (Au + 0.03% Fe/Chromel) placed just below the sample.

Each sample was loaded into a 4 mm O.D. "Spectrosil" fused silica glass tube connected to a Kontes high vacuum valve. These tubes were then evacuated and sealed off under high vacuum.

2.6.3 Magnetic Susceptibility

The magnetic susceptibilities were measured with an S.H.E. computer-controlled variable temperature SQUID (Superconducting Quantum Interference Device) magnetometer. The sample cell - a small cylidrical bucket of dimensions 8.5 mm by 6.5 mm in diameter - was made of Kel-F. A thread 15-20 cm long was attached to the bucket through four holes. The buckets were filled with the samples, while being kept cold, inside a glove bag. In order to keep the samples cold while loading into the SQUID, a copper block, previously immersed in liquid nitrogen, was fit into the airlock of the SQUID. This block has a central hole 7 mm in diameter to allow passage of the sample through it. To

prevent the introduction of air and moisture into the SQUID during loading, a glove bag had been placed around the airlock and purged with helium gas. The procedures used to load and center the samples in the SQUID cavity have been described in detail by Issa [57]. The susceptibility measurements were made over a temperature range of 1.7 to 280 K. Ten readings were obtained at each temperature and the average χ_s was calculated. χ_s and χ_d are actually only relative susceptibilities since the mass was not included in their calculation. To correct for the residual diamagnetism of the bucket, this was removed from the SQUID cavity and the sample was allowed to decompose at room temperature in an inert atmosphere. Subsequently, the bucket containing the decomposed sample was loaded back into the SQUID, and its susceptibility was measured as was done previously for the pristine sample. The electronic contribution to the susceptibility χ_M^e was calculated by subtracting the diamagnetism of the bucket and the decomposed sample, χ_d, from the sample susceptibility as described by:

$$\chi_M^e = \frac{\chi_s - \chi_d}{n} \qquad (11)$$

in which n is the number of moles of sample.

2.6.4 Pressed Powder Conductivity

The conductivity measurements were made by using the apparatus designed and described by Yemen [60]. Powder sampes were loaded into a 2 mm I.D. heavy wall fused silica tube to be placed between two stainless steel electrodes. A steel spring with known force constant was used to compress the sample. A variable temperature controller (Varian Model V-4540) was used to control the sample temperature. The first part of the experiment involved measurement of the current at various voltages to determine whether the sample exhibited Ohm's Law behavior. Next, the current through the sample was measured at different temperatures at a constant voltage.

2.7 Recrystallization

The method most commonly used to recrystallize alkalides and electrides involves cycling the temperature of a solution of the corresponding compound. The temperature range is chosen such that, at the high temperature limit, all the material is in solution, while at the low temperature limit, crystals of the material are produced. The vessel used to prepare the solutions and the crystals is illustrated in Figure 7. The cell was initially evacuated to 10^{-5} torr, and subsequently opened inside a glove bag with a dry nitrogen atmosphere. Inside

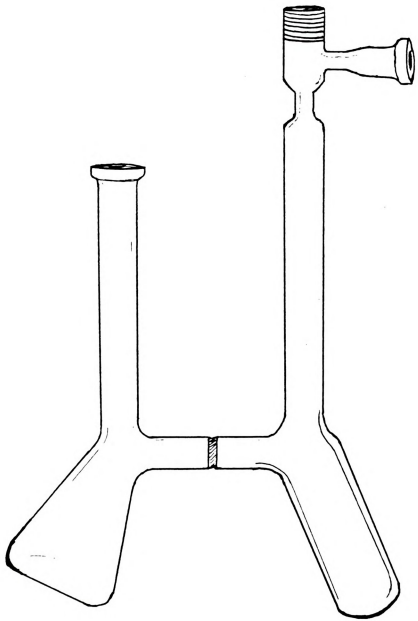

Figure 7. Vessel used in the recrystallization of alkalides and electrides.

the glovebag, samples consisting of about 0.25 mmole of compound were poured into the cell which was kept cold throughout the whole procedure. After attachment to the vacuum line a solvent of relatively high dielectric constant, such as methylamine or dimethylether, was distilled into the vessel. The object at this stage was to completely dissolve the sample in the smallest possible amount of solvent. The solution was stirred and poured through the glass frit inside the vessel to insure that all of the solid had dissolved. Once all the crystals had dissolved, a low dielectric constant solvent - in which the compound is insoluble - was added. It is important to find a ratio of solvents that will produce seed crystals with relative ease, while keeping the total volume of solution low. Usually the total volume of solution was less than 10 ml. At this point, the vessel was placed in a controlled temperature bath, and the scans were started. For example, in the recrystallization of a sample of $Cs^{+}(18C6)_2Rb^{-}$, the temperature was scanned between $-40^{o}C$ and $-60^{o}C$ over a period of five hours. After two or three cycles, the temperature was kept at the low limit or reduced further (-65 to -68 ^{o}C).

Once crystals had been obtained, the mother liquor was poured into the adjacent chamber and was distilled out of the vessel into a waste bottle. The crystals were then kept under dynamic vacuum ($p < 10^{-5}$ torr) at $-78^{o}C$ until use. Alternatively, they were loaded in glass ampoules and

stored in a freezer. However, the quality of the crystals deteriorates when stored for long periods of time. For best results, it is necessary to use the crystals promptly after preparation.

2.8 Synthesis and Crystallization of Model Compounds

The preparation of complexes of alkali metal salts with the various complexing agents was of interest since it was expected that these compounds could effectively model the structure and the electronic environment of the complex cation moiety found in alkalides and electrides. These model compounds played a key role in the X-ray absorption studies: in the XANES studies, their near-edge spectral features provided a prototype for the spectra of complexed cations. By comparing the position of the edge and the spectral features to those of alkalides and electrides, it was possible to identify the oxidation state of the absorbing metal in the solids. In the EXAFS work, the data from models of known crystal structure is essential in the determination of bond lengths and number of neighbors. In the alkali metal NMR studies, the spectra of the models provide a reference with which to compare chemical shifts and line widths.

With this in mind, several crystalline complexes were prepared. The procedures used were similar to those of Pedersen [15].

The rubidium salts RbSCN, RbI, RbBr, and RbCl were purchased from Pfalz and Bauer Inc. and were used after drying at 100° C. The solvents methanol, ethanol, and isopropanol were reagent grade and were dried with Linde type 4A molecular sieves.

The first method used to prepare the complexes involved dissolving stoichiometric amounts of the salt and the complexant in the minimum amount of methanol with stirring and mild heating. This was followed by fast filtration, fast cooling and storing at -15° C for crystallization. For most cases, however, this procedure did not yield crystals and it was necessary to concentrate the solution further, by heating and evaporating some of the solvent, in order to induce precipitation. However, if the cooling was fast, at best only powdery and polycrystalline solids were recovered. The complexes Rb^+(18C6) SCN^- and Rb^+(18C6) I^- were prepared by the following procedure. For the synthesis of the thiocyanate, equimolar amounts of RbSCN and 18C6 were dissolved in methanol (concentration 0.22M) with stirring at approximately 60° C. After the solutes had been dissolved, the filtered solution was stored at -15° C for two weeks but no crystals were formed. After concentrating the solution twice, white crystals were obtained. Their melting point is 192° C. In the case of the iodide, isopropanol was used to dissolve the starting materials, and a more dilute (0.02M) solution was used. White

crystals of the complex (melting point 224^{o}-227^{o} C) were obtained after 24 hours.

The procedure that worked best in producing single crystals involved the preparation of a dilute solution of the complexant and salt with heating to near-boiling temperatures while stirring, followed by fast filtration and then allowing the solution to slowly cool down to room temperature. The vessel was covered with a permeable material to allow very slow evaporation of the solvent. By using this procedure, large single crystals were obtained in almost every case.

In the preparation of Rb^{+}(18C6) Br^{-}, a solution containing equimolar amounts of RbBr and 18C6 (0.014M) was prepared in methanol at 60^{o} C. After the starting materials had been dissolved, enough isopropanol was added while heating to approximately double the volume. After a short time, the solution was filtered and allowed to cool down slowly. Slow evaporation of the solvent was also allowed. Overnight, large hexagonal, translucent single crystals were obtained. The crystals melt at 145^{o} -147^{o} C. The quality of these crystals deteriorates - they become brittle and cracked - when the solvent is evaporated to dryness; thus, for the crystallographic studies it was necessary to leave a small amount of mother liquor around the crystal.

The composition of the complex was analyzed by using proton NMR to determine the amount of compexant in the

solid. The crystal structure was obtained by single crystal X-ray diffraction, as will be described in Chapter 5.

The preparation of $Rb^{+}(18C6)_2Br^{-}$ was attempted from a solution of RbBr and 18C6 with a complexant/salt ratio of two. No crystals were obtained by following the usual procedures. The solution turned instead into a suspension of viscous consistency.

Translucent crystals of $Rb^{+}(18C6)\ Cl^{-}$ were obtained from a solution in methanol (0.14M) by using Method II. These crystals also degrade if the solvent is evaporated to dryness.

A complex of 15C5 was also synthesized. Crystals of $Rb^{+}(15C5)_2Cl^{-}$ were prepared from a solution 0.18M in RbCl and twice as concentrated in 15C5. Methanol was used as the solvent. After slow cooling and some slow evaporation of the solvent, a few crystals form. A small amount of acetone was added. This resulted in the precipitation of a large number of small white crystals of $Rb^{+}(15C5)_2Cl^{-}$.

CHAPTER THREE

SYNTHESIS AND CHARACTERIZATION OF RUBIDIDES

3.1 Synthesis of Crystalline Alkalides and Electrides

Because the X-ray absorption techniques, EXAFS and XANES, promised to be valuable in the studies of rubidium-containing alkalides and electrides, a list of the possible candidates for study was prepared. At the time, no pure rubidides - compounds of stoichiometry $M^+C\ Rb^-$ were known. Thus, it was of interest to prepare pure solid rubidides in order to compare and contrast their properties with those of other alkalides and electrides. The compounds were prepared by crystallization from solution. In essence, these syntheses consist of three parts. The first part involves the dissolution of the starting materials with a polar - high dielectric constant - solvent. Among the solvents most used are methylamine and dimethylether. These are not only highly effective in dissolving the starting materials, but also produce very stable solutions of the alkali metals and complexants.

The second part of the synthesis is the crystallization of the complexed salts. This process involves the addition of one or two co-solvents that can

induce the formation of crystals of the products. An ever-present goal of the crystallization step was the preparation of single crystals of the best quality possible within the constraints and limitations posed by the reactivity and instability of the solutions. Thus, several solvent systems were tried for each complex in order to optimize the crystallization conditions. The crystallization process was straightforward in some cases - just adding the crystallization co-solvent and cooling the solution to -78^{o}C was enough to produce small crystals. However, in the majority of cases it was necessary to add more than one co-solvent. These solvents were chosen such that a gradual increase of their concentration in solution would result in a decrease of the dielectric constant of the medium. It has been known for a long time [61] that, for ionic solids, the electrostatic forces between crystal and solution play a major role in crystal growth. It was shown that, as the dielectric constant of the solvent was increased, it became more difficult to detect the characteristic layer growth of single crystals [62]. In the preparation of alkalides and electrides it has been found experimentally that the reduction of the dielectric constant of the solution medium produces crystallization. Thus, crystals are prepared by dissolving the starting materials in methylamine (dielectric constant 9.4 at 25^{o}C) followed by slow replacement of the methylamine with isopropyl amine (dielectric constant 5.6 at 25^{o}C) and

diethyl ether (dielectric constant 4.34 at 20°C), or by dissolving with dimethyl ether (dielectric constant 5.02 at 25°C) followed by replacement of this solvent with trimethylamine (2.44 at 25°C.) The replacement of the initial solvent is achieved by vacuum distillation of up to 90% of the solvent followed by addition of the co-solvent(s), or by multiple successive distillations of smaller amounts of the original solvent out and the co-solvent(s) in. The more gradual the change, the better the quality of the crystals produced. The same applies to the control of the temperature of the solution. The alkalides and electrides crystallize when the temperatures of the solution are lowered. However, it is essential to cool the solutions gradually - fast cooling results in the formation of thick film deposits on the walls of the vessel or of compact chunks of powder or polycrystalline material that sticks to the bottom of the vessel.

The last part of the synthesis involves washing and drying the crystals. It is of extreme importance to utilize low temperatures and non-polar solvents for the washing. It is also essential to dry the crystals carefully by dynamically evacuating at $\leq 10^{-5}$ torr for at least 40 minutes in order to obtain loose, single crystals.

3.2 $Cs^+(18C6)_2Rb^-$: Preparation and Identification of Species

Of all the pure rubidides prepared, $Cs^+(18C6)_2Rb^-$ is the most stable and, for this reason, it has been possible to study its properties in more detail.

3.2.1 Synthesis

Solutions of the appropriate stoichiometry were prepared by dissolving the starting materials in dimethylether at temperatures between -10^oC and -20^oC, cooling further as the metal concentration in solution increased. Crystals can be easily obtained from trimethylamine. For slower crystallization and better quality crystals, diethylether was added first, followed by several successive additions of small amounts of trimethylamine. The crystals were washed with trimethylamine. The results of analysis indicated that 1.622×10^{-4} moles of H_2 were released upon oxidation of the sample with water. The results of titration gave 2.2×10^{-4} moles of OH^- while the NMR indicated the presence of 3.39×10^{-4} moles of 18C6 in the sample. The results of flame emission on a different sample indicated 1.30×10^{-5} and 1.53×10^{-5} moles of cesium and rubidium in the sample, respectively.

3.2.2 Optical Spectrum

The initial work on the characterization of $Cs^+(18C6)_2Rb^-$ involved the measurement of the optical spectra of thin solvent-free films of the material. The absorption spectrum is illustrated in Figure 8. The bronze-colored films were prepared by fast solvent evaporation from a solution in dimethyl ether. The principal absorption band is observed at 8,750 cm^{-1} (1,143 nm) with a shoulder at 10,800 cm^{-1} (923 nm). These bands can be assigned to the absorptions by the trapped electron and Rb^-, respectively. Both bands appear red-shifted from those obtained for films of rubidium and 18C6 with a ratio of metal to crown, R, equal to two [23]; the trapped electron band is shifted by 350 cm^{-1} and the Rb^- band by 1,200 cm^{-1}. The appearance of the spectrum does not change with temperature or time.

The absorption band of the ceside anion has been observed at 10,500 cm^{-1} (950 nm) in films prepared from cesium and C222 with R=2. This value is very close to that of the shoulder observed in the present spectrum of $Cs^+(18C6)_2Rb^-$. This could be interpreted to be an indication of the presence of some Cs^- in the film. However, previous results indicate that the films prepared with cesium and 18C6 only show a single band at 6400 - 6700 cm^{-1}, regardless of the ratio of metal to complexant. This band has been attributed to trapped electrons isolated

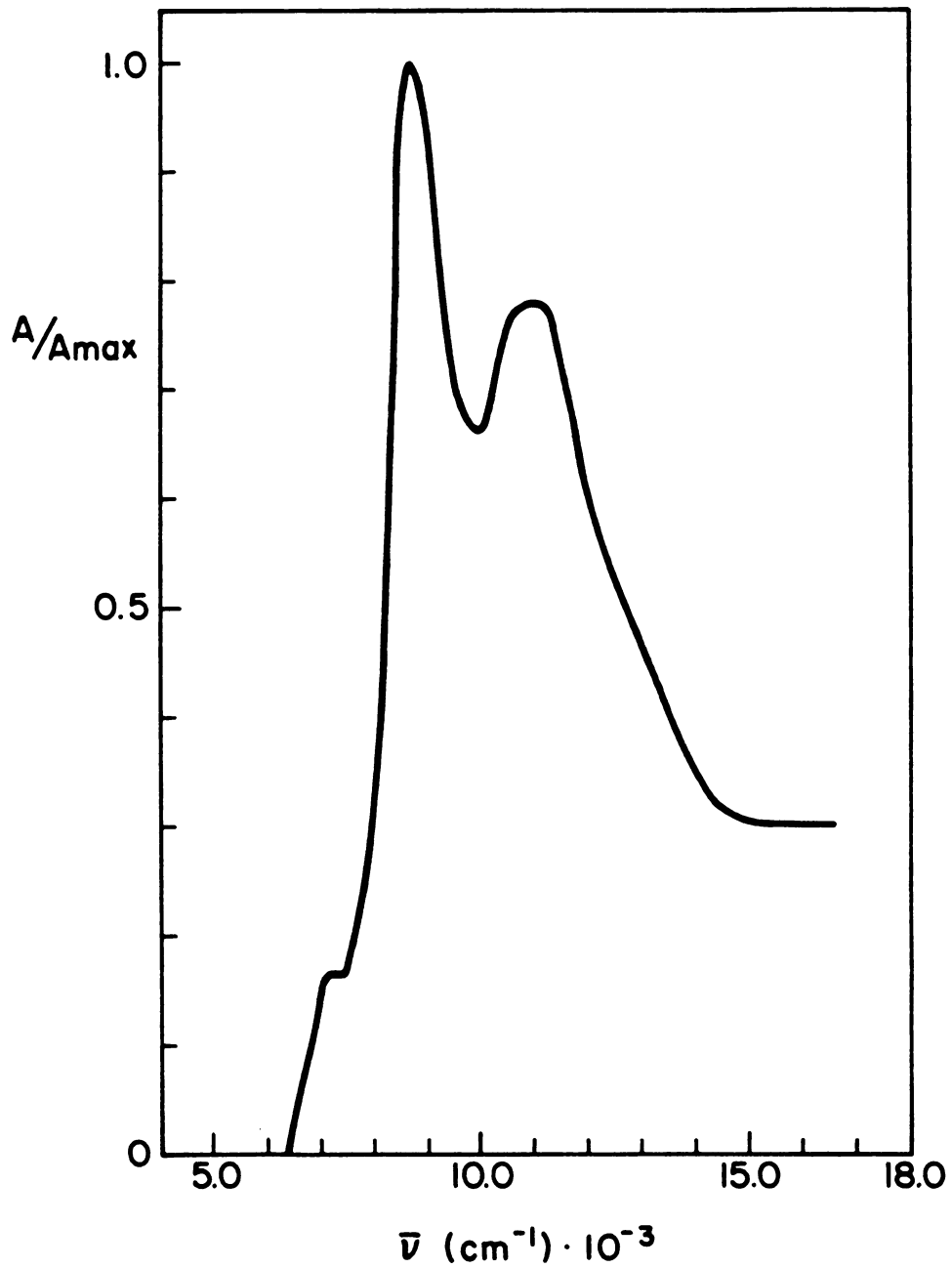

Figure 8. Optical spectrum of $Cs^{+}(18C6)_2Rb^{-}$, thin film prepared from dimethyl ether solution.

from Cs^+. The cesium cation would be effectively isolated from all other species if it were encapsulated by two 18-crown-6 rings. Thus, since the ceside band at 10,500 cm^{-1} has never been observed for films that contain 18-crown-6, it seems unlikely that the band at 10,800 cm^{-1} in the present spectrum would have some contribution from ceside absorption. In any case, it can be seen that it is not possible, by using the optical spectrum alone, to identify unambiguously the species present in the films. All evidence obtained so far indicates that the solvent-free films prepared from solutions by fast evaporation of the solvent contain species which are present in the mother solution, but which are not necessarily present in the crystals obtained by slow evaporation.

3.2.3 Solid State Nuclear Magnetic Resonance With Magic Angle Sample Spinning (MAS-NMR)

The fact that $Cs^+(18C6)_2Rb^-$ is a rubidide and not a ceside, electride, or a mixture was proved by using the data obtained from both XANES and ^{87}Rb and ^{133}Cs solid state MAS-NMR. The XANES data will be presented and discussed in Chapter 4. The MAS-NMR experiments were performed by A. Ellaboudy [59].

The chemical shifts and the linewidths measured for 1:1 complexes of Cs and 18C6 are clearly different from those of the 1:2 "sandwich" complexes. The chemical shifts

of complexes that contain the cation $Cs^+(18C6)_2$ are upfield from those of solids that contain $Cs^+(18C6)$, and are independent of the nature of the anion. This can be explained in terms of the enhanced shielding of Cs^+ from the anions that is provided by the three-dimensional "sandwich" arrangement of the complexant. The narrow NMR linewidths observed in the spectra of the "sandwich" complexes are due to their higher symmetry as compared with that of the 1:1 arrangement.

The ^{133}Cs and ^{87}Rb MAS-NMR spectra of $Cs^+(18C6)_2Rb^-$ are shown in Figure 9. The chemical shift of the $Cs^+(18C6)_2$ moiety is -57 ppm with respect to infinitely dilute $Cs^+_{(aq)}$, a value in the range characteristic for solids that contain the "sandwiched" $Cs^+(18C6)_2$ cation. The ^{87}Rb NMR shows a strong, narrow line at -193 ppm (at 163.6 MHz) with respect to infinitely dilute $Rb^+_{(aq)}$. Although this spectrum was the first one recorded for a solid rubidide, further studies have indicated that the observed chemical shift is in a range characteristic for rubidides [63].

3.3 $Cs^+(18C6)_2Rb^-$: Electronic and Magnetic Properties

It is reasonable to expect pure alkalides to be diamagnetic. However, studies of the electron paramagnetic resonance (EPR) spectra, magnetic susceptibilities and conductivities of crystalline alkalides [24] showed that

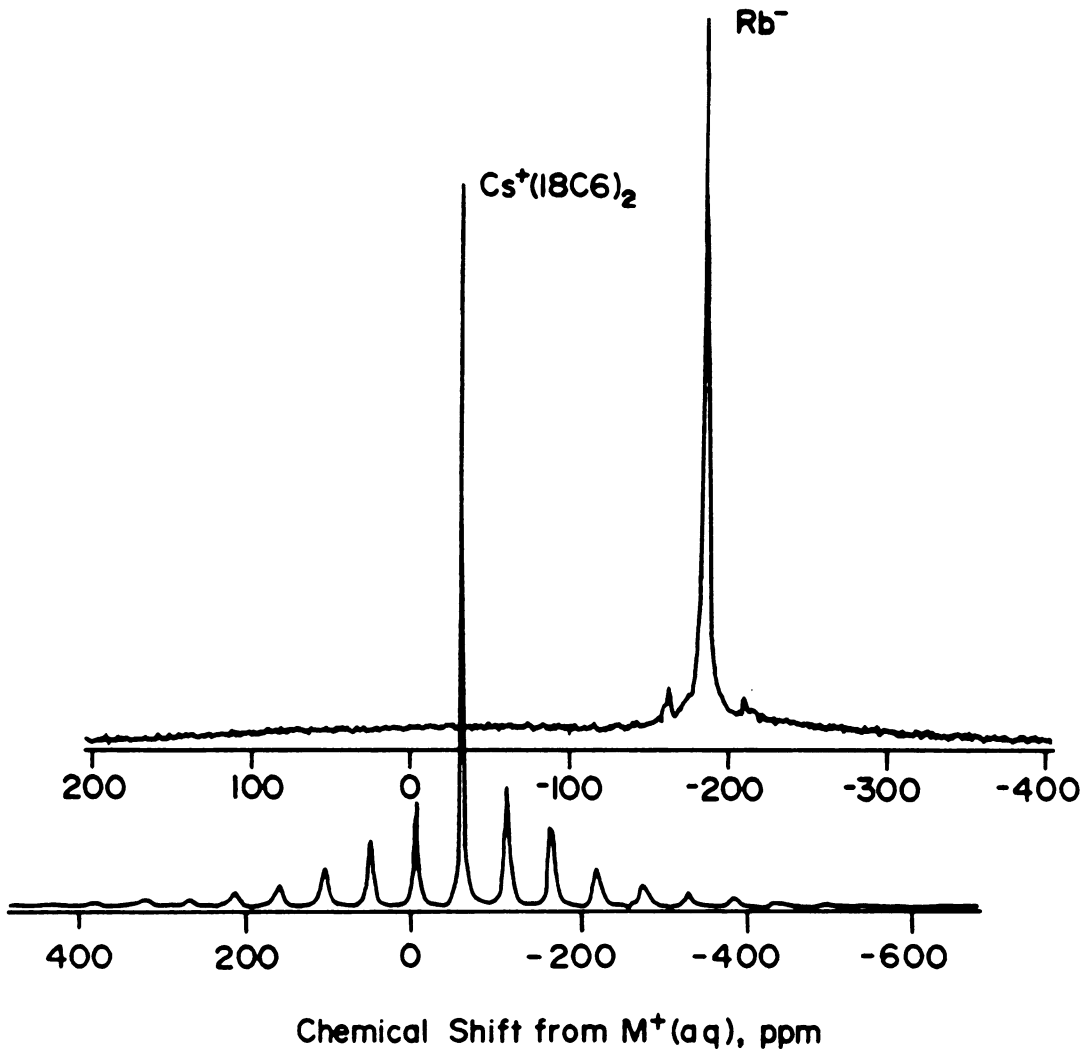

Figure 9. ^{133}Cs (at 65.61 MHz) and ^{87}Rb (at 163.6 MHz) MAS-NMR spectrum of $Cs^{+}(18C6)_2Rb^{-}$ [59].

alkalides can contain measurable concentrations of trapped electrons. The concentrations of such trapped electrons are dependent upon the method of preparation and ultimately, on the conditions used in the crystallization process. The magnetic susceptibility, EPR spectra, and conductivity data are valuable in probing the types of electron-trapping sites and the interactions of the trapped electrons with each other and with the other species present in the crystals. With this in mind, the electronic and magnetic properties of $Cs^{+}(18C6)_2Rb^{-}$ were examined.

3.3.1 Electron Paramagnetic Resonance

The EPR spectrum of $Cs^{+}(18C6)_2Rb^{-}$ at 10.3 K is shown in Figure 10. The spectrum consists of a single asymmetric line with a g-value of 2.0086 $\pm$ 0.0001 and linewidth of 2.4 $\pm$ 0.1 G. The signal is of intermediate intensity and has a ratio of low-field to high-field amplitudes, A/B, of 1.83. An A/B ratio greater than one usually accompanies a high microwave conductivity in a solid. However, in this case, the line appears inhomogeneously broadened, and this could be an indication of overlapping signals. If that were the case, the fact that the A/B ratio is greater than one would not necessarily imply high microwave conductivities. The intensity and width of the EPR signal are strongly dependent on temperature. Upon increasing the

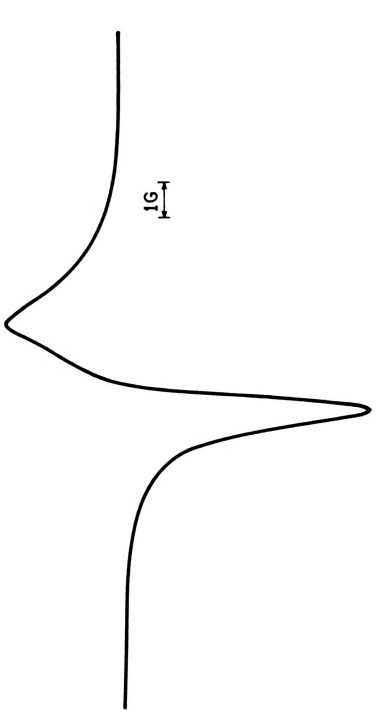

Figure 10. EPR spectrum of $Cs^{+}(18C6)_2Rb^{-}$ at 10.3 K.

temperature from 2.4 to 100 K, the intensity of the signal decreased to 25% of its original value.

3.3.2 Magnetic Susceptibility

Considerable information on the electronic and magnetic interactions in alkalides and electrides has been obtained from the study of the magnetic susceptibility as a function of temperature [24, 57, 59]. The magnetic susceptibility of polycrystalline $Cs^+(18C6)_2Rb^-$ was measured in the range of temperatures from 1.6 K to 256 K. The variation of the molar electronic susceptibility χ_M^e of $Cs^+(18C6)_2Rb^-$ as a function of temperature is illustrated in Figure 11. The electronic contribution to the susceptibility was obtained from the difference between the measured susceptibility of the sample and that of its decomposition product. As can be seen, the sample exhibits a small paramagnetism which is only slightly temperature-dependent at high temperatures, but which rises sharply as the temperature is decreased. The data shown were fit with the Curie-Weiss law in the form

$$\chi_M^e = \frac{fC}{T - \Theta} + B \qquad (12)$$

where f is the fraction of anionic sites which contain trapped electrons, C is the Curie constant, Θ is the Weiss constant, and B is the diamagnetic contribution to the

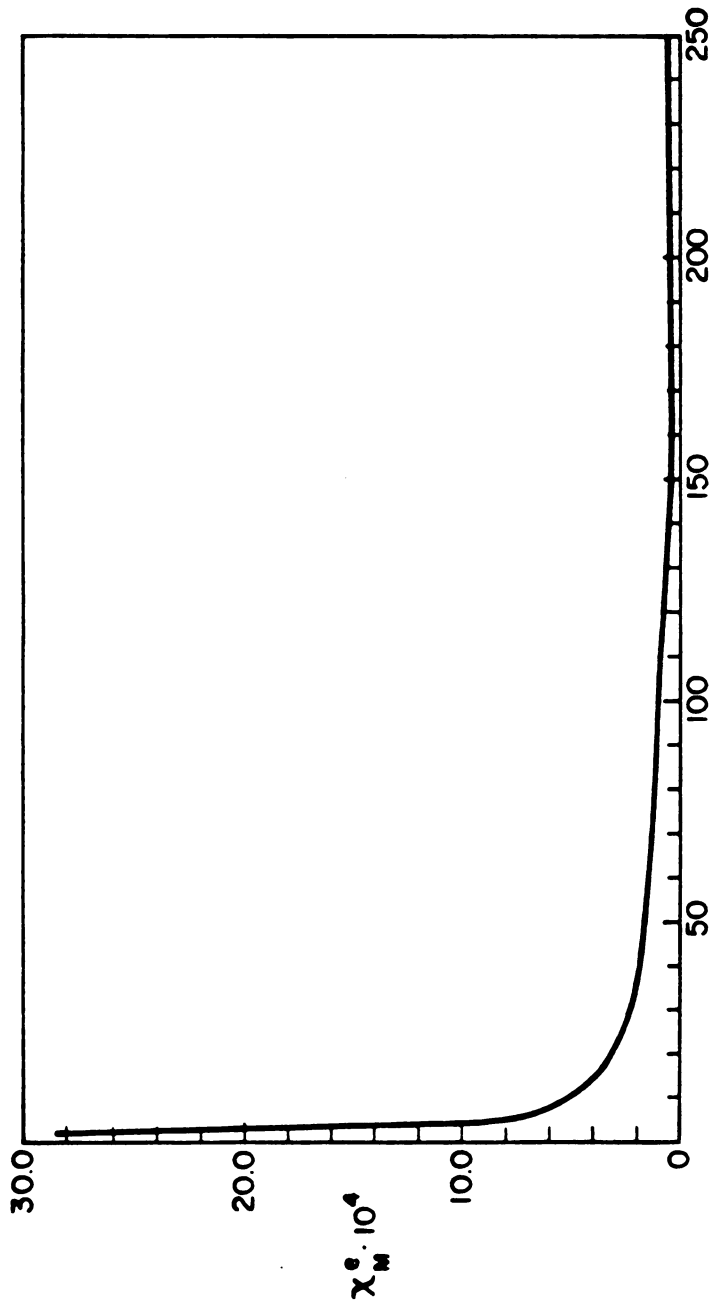

Figure 11. Molar electronic susceptibility, χ_M^e, of $Cs^+(18C6)_2Rb^-$ as a function of temperature.

molar electronic susceptibility, presumably from Rb^-. The susceptibility data for $Cs^+(18C6)_2Rb^-$ is peculiar in that the susceptibility values measured for rising temperatures were noticeably more positive than the values obtained for decreasing temperatures. For this reason each data set was fit separately to obtain different sets of parameters for rising and falling temperatures. The values obtained and their standard deviations are $f = 2.26 \times 10^{-3} \pm 0.41 \times 10^{-3}$, $\Theta = 2.4 \pm 1.7$, $B = 2.77 \times 10^{-4} \pm 0.08 \times 10^{-4}$ for increasing sample temperatures, and $f = 1.36 \times 10^{-2} \pm 0.06\ 10^{-2}$, and $B = 64 \times 10^{-6} \pm 10 \times 10^{-6}$, for decreasing temperatures. It was not possible to obtain a reliable value from the latter run. The values obtained clearly indicate the presence of a small amount of trapped electrons in the sample. The susceptibility data for increasing temperatures were collected immediately after loading the sample in the susceptometer's cavity, and it is possible that the higher susceptibility values obtained are a result of the handling of the sample just prior to data collection. The sample was transferred from a glove bag - where it had been poured into the SQUID bucket - to the SQUID airlock at 77 K. After the sample was placed in the airlock, this had to be purged with helium for a few minutes, which may have raised the temperature of the sample momentarily. Following this, the sample was loaded into the SQUID cavity and its temperature was lowered to 5 K. Once the data collection was started, susceptibilities

slightly higher than those shown in Figure 11 were obtained with increasing temperatures up to a temperature of 170 K where the susceptibility dropped to the illustrated values. The susceptibility values stayed lower than the values obtained initially for the rest of the run. The described behavior could be a result of annealing of the sample. The obtained f values indicate that initially the sample contained a fraction of its electrons either in the conduction band or in shallow traps in electron-paired states. These electrons seem to exhibit nearly temperature-independent paramagnetism. Upon raising the temperature, the sample anneals and an increasing number of electrons fall into deeper traps. As a result, higher f values are observed. Table 1 lists these values along with those of the other salts that contain $Cs^{+}(18C6)_2$ as the cation. The first compound in the series, $Cs^{+}(18C6)_2Na^{-}$, is diamagnetic in the temperature range 1.6 to 300 K with a molar susceptibility of -1.72×10^{-4} emu/mole (total susceptibility) [57]. The annealed rubidide shows an unpaired electron content of 1.36%, while the content in the ceside is higher at 2.01%.

3.3.2 Pressed Powder DC Conductivity

The pressed powder dc conductivity of $Cs^{+}(18C6)_2Rb^{-}$ was measured as a function of temperature. Initially, the current was measured as a function of voltage to test

Table 1: Parameters of the Curie-Weiss Equation for χ_M^e for Compounds that Contain $Cs^+(18C6)_2$

Compound	$10^2 f$	Θ, K	$10^6 B$
$Cs^+(18C6)_2Na^-$ (a)	-	-	-
$Cs^+(18C6)_2Rb^-$ (b)	0.226 ±0.041 (d)	2.4 ±1.7	277 ±8
$Cs^+(18C6)_2Rb^-$ (c)	1.36 ±0.06	-	64 ±10
$Cs^+(18C6)_2Cs^-$ (e)	2.01 ±0.02	-1.1 ±0.1	-36 ±1
$Cs^+(18C6)_2e^-$ (e)	73.6 ±0.9	-1.44±0.05	0

(a) From Ref. 57.

(b) Data obtained for increasing temperatures.

(c) Data obtained for decreasing temperatures.

(d) Standard deviation estimates from the fit of each data set independently.

(e) From Ref. 59.

whether the sample obeyed Ohm's Law. As shown in Figure 12, $Cs^{+}(18C6)_2Rb^{-}$ nearly follows Ohm's Law, although some polarization is evident. Next, the current was measured at various temperatures in the range from -4.0° C to -83.5° C, at a constant voltage of 4.00 V. The conductivity, σ, was obtained from the values of the current, and its logarithm, ln σ, was plotted as a function of reciprocal temperature, as illustrated in Figure 13. As can be seen, the conductivity drops as the temperature is decreased, as expected for semiconductor behavior. The initial ln σ values for reciprocal temperatures between 3.8 and 4.85×10^{-3} K^{-1} are artificially lower than the other points in the plot. This effect is probably due to changes in the resistance with sample packing in the quartz cell and has been observed often in the past.

The conductivity for semiconductors is largely controlled by the ratio of the band gap, E_g, to the temperature as given by [64]

$$\sigma = \sigma_\infty \exp \{-E_g/2kT\} \qquad (13)$$

where σ_∞ is the limiting specific conductance at infinite temperature.

The plot of ln σ vs. reciprocal temperature shows a change in the slope of the line at approximately 4.38×10^{-3} K^{-1}. The experimental points for each section of the data (from 1/T of 3.70×10^{-3} to 4.38×10^{-3} K^{-1} and

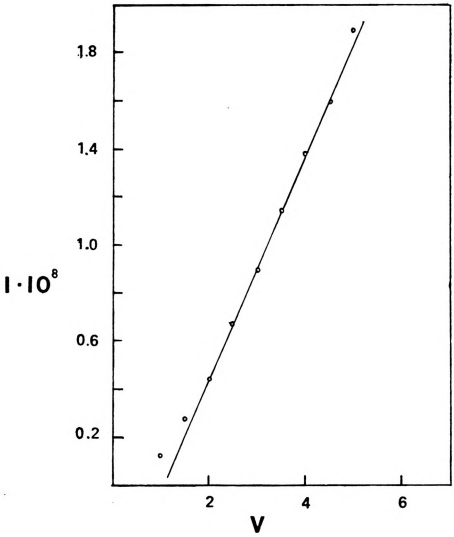

Figure 12. Ohm's Law plot for pressed polycrystalline $Cs^{+}(1806)_2Rb^{-}$.

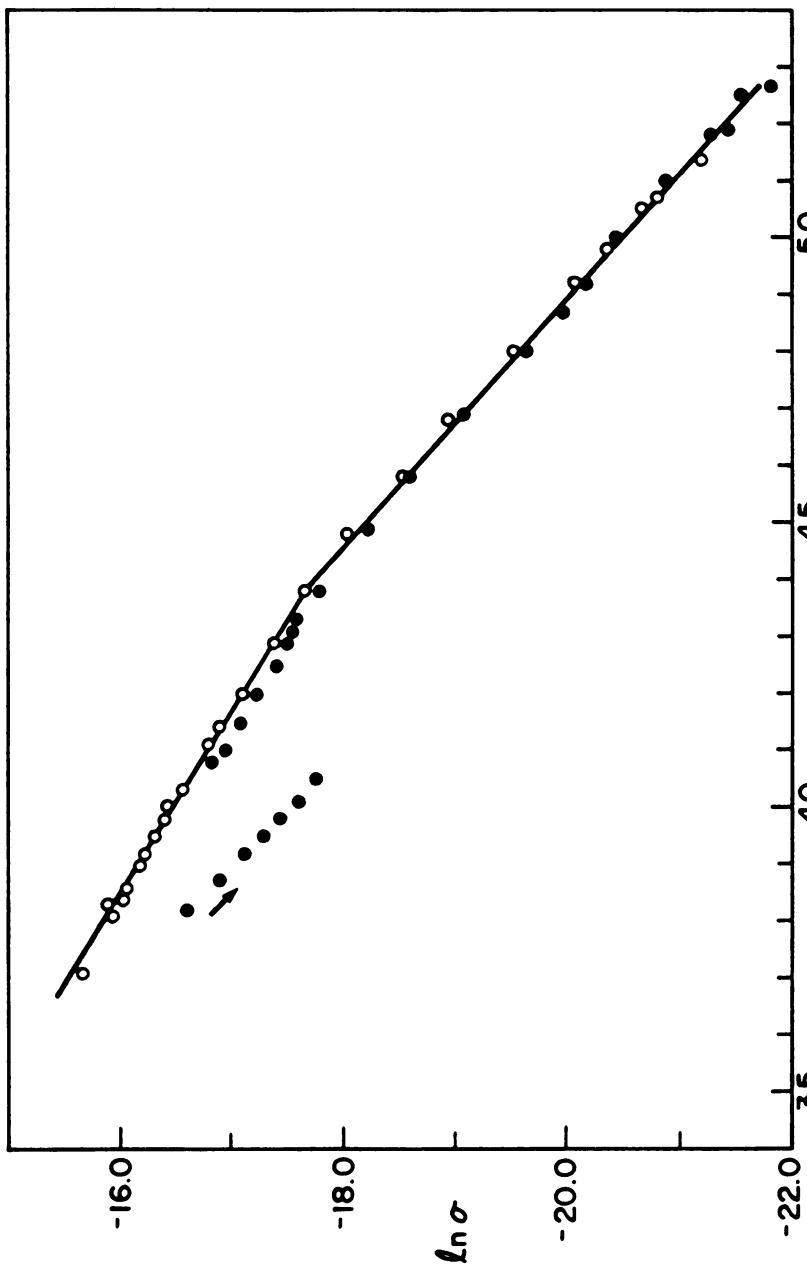

Figure 13. Plot of ln conductivity vs. reciprocal temperature for polycrystalline $Cs^{+}(18C6)_2Rb^{-}$.

from 4.40 x 10^{-3} to 5.27 x 10^{-3} K^{-1}) were least-squares fit with Equation 13 and values for the band gap and the limiting conductance were calculated. In the range of temperatures from -29 ^{o}C to -41^{o}C (3.70 x 10^{-3} $\leq$ 1/T $\leq$ 4.38 x 10^{-3} K^{-1}) the slope of the line gave an apparent bandgap of 0.56 eV. Extrapolation of the line to infinite temperature gave for the limiting specific conductance 0.0282 $ohms^{-1}cm^{-1}$, a value which falls in the range characteristic for extrinsic semiconductors. In the temperature range from -42^{o}C to -83.5^{o}C (4.38 x 10^{-3} $\leq$ 1/T $\leq$ 5.27 x $10^{-3}K^{-1}$) the band gap was found to be somewhat larger at 0.77 eV. The specific limiting conductance value obtained was 6.494 $ohms^{-1}cm^{-1}$. The value of approximately 0.8 eV for the band gap of the rubidide is the same as was obtained for the ceside [59], $Cs^{+}(18C6)_{2}Cs^{-}$, a value which is consistent with the thermal excitation of a low concentration of trapped electrons and which also corresponds to the position of the absorption maximum in electrides [24].

In conclusion, the EPR, magnetic susceptibility and dc conductivity data for $Cs^{+}(18C6)_{2}Rb^{-}$ are essentially determined by a small concentration of non-interacting trapped electrons. Similar behavior has been observed for $Cs^{+}(18C6)_{2}Cs^{-}$ and other alkalides.

3.4 $K^+C222Rb^-$

3.4.1 Synthesis

Stoichiometric amounts of the starting materials were dissolved in dimethyl ether at -35°C. Crystals were obtained relatively rapidly by adding diethyl ether and trimethylamine (approximately 30% and 70% by volume, respectively). The metal content as determined by flame emission gave 5.78×10^{-5} moles of potassium and 5.04×10^{-5} moles of Rb^-.

The identification of the species in the golden-colored crystals of $K^+C222Rb^-$ was accomplished by using optical spectroscopy and XANES spectroscopy. The XANES results are presented in Chapter 4. Attempts to identify the rubidide by using the ^{87}Rb MAS-NMR spectrum were unsuccessful as the expected signal of Rb^- was not detected. However, it has been found that the absence of an NMR peak of Rb^- cannot be used as evidence that the rubidide ion is not present, since there are a few instances of compounds for which the presence of Rb^- was determined by alternate experimental techniques, and for which no NMR signal was obtained [63].

3.4.2 Optical Spectrum

The absorption spectrum of $K^+C222Rb^-$ is illustrated in Figure 14. The films were prepared from a solution in dimethyl ether. An intense absorption band is observed at 10,800 cm^{-1} (900 nm) with a broad shoulder at 8,300 (1200 nm). The principal band can be attributed to absorption by Rb^-. It is red-shifted by 500 cm^{-1} from the rubidide peak in solutions of Rb and C222 in methylamine. The band at 8,300 cm^{-1} is probably due to absorption by trapped electrons. The appearance of the spectrum was independent of both temperature and time.

3.5 $Li^+C211Rb^-$

3.5.1 Synthesis

The vessel used in the synthesis of $Li^+C211Rb^-$ was made of fused silica and contained an additional compartment attached to the complexant chamber by a sidearm. This compartment allowed the purification of the C211 by 'in situ' distillation just prior to the start of a synthesis. This distillation into the complexant compartment was done at 70-75°C. Once all of the liquid complexant had been distilled into the synthesis cell, the extra compartment was flame-sealed off.

The starting materials were dissolved in methylamine

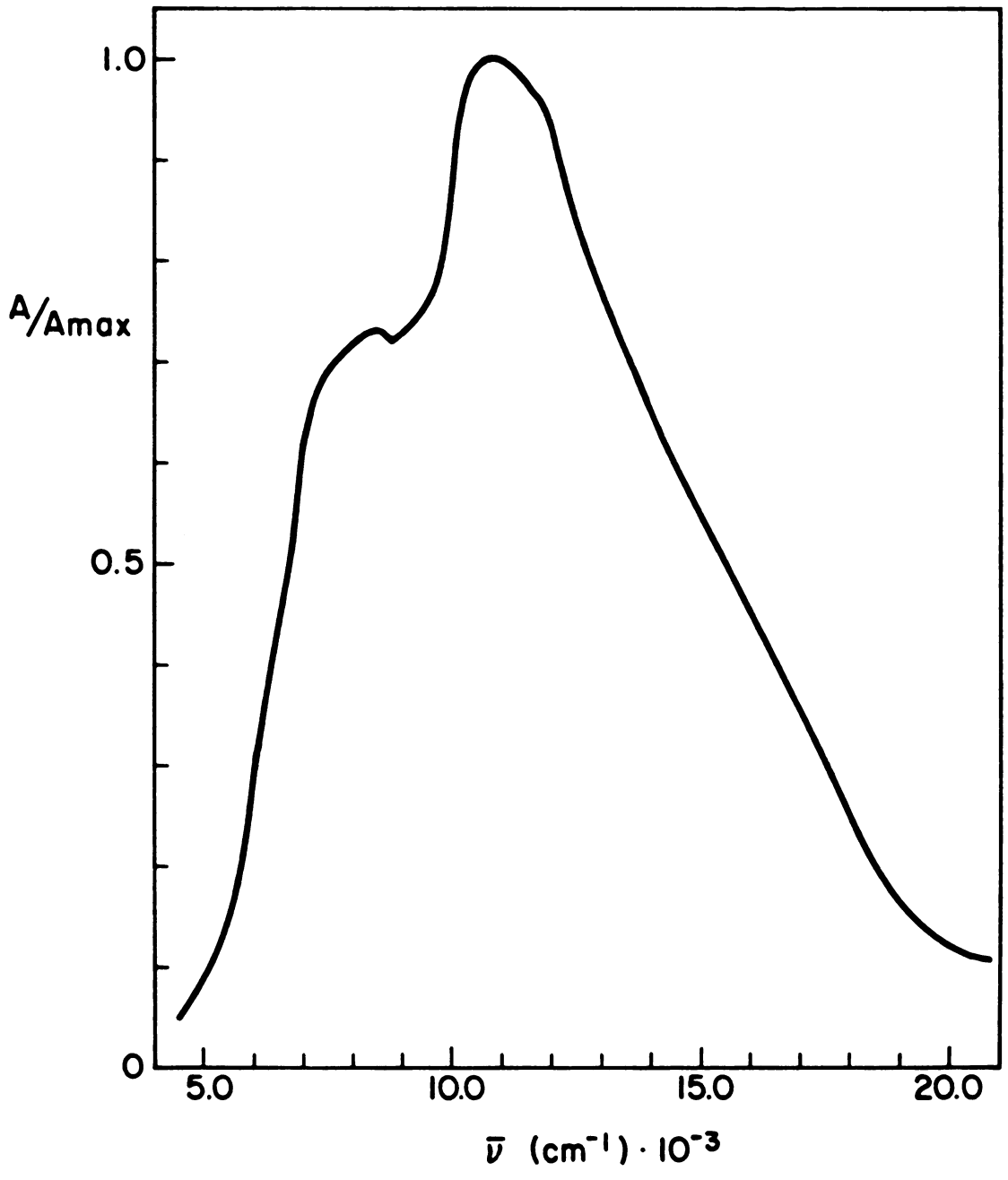

Figure 14. Optical spectrum of $K^{+}C222Rb^{-}$, thin film prepared from dimethyl ether solution.

at temperatures ranging from -38°C to -50°C. Following this, the solution was allowed to stand for two hours to allow complexation of the cation. Crystals of the product were obtained from a mixture of isopropylamine and diethyl ether, and were washed with the latter solvent. The results of the hydrogen evolution experiment indicated 1.73×10^{-5} moles of rubidide in the sample, while metal analysis by flame emission indicated 2.84×10^{-5} and 2.92×10^{-5} moles of lithium and rubidium respectively.

This rubidide is the most unstable of all the compounds discussed here. The solutions of the starting materials often decomposed if the temperature was higher than -35°C or if the solution was allowed to stand for more than four hours, as was necessary sometimes in order to dissolve the rubidium. The crystals obtained often deteriorated considerably upon washing. The dry solid decomposed violently. For these reasons it was not possible to fully characterize this compound. Magnetic susceptibility studies were carried out with the object of comparing the susceptibility with that of the $Li^{+}C211\ e^{-}$. This electride exhibits Curie-Weiss behavior at high temperatures, a maximum in the susceptibility at temperatures ranging from 20 to 70 K, and susceptibilities that approach zero at liquid helium temperatures [21]. It was of interest to find out if $Li^{+}C211\ Rb^{-}$ contained signigicant concentrations of trapped electrons as was the case for $Cs^{+}(18C6)_2Rb^{-}$.

Magnetic Susceptibility

The crystals of $Li^{+}C211\ Rb^{-}$ were found to be diamagnetic in the temperature range between 1.6 and 180 K, and there was no evidence for magnetic ordering. The experimentally obtained molar susceptibility value is 6.67×10^{-5} emu/mole. From this, it can be concluded that the concentration of trapped electrons in crystals of $Li^{+}C211Rb^{-}$ is negligible.

CHAPTER FOUR

RUBIDIUM X-RAY ABSORPTION STUDIES OF Rb^- AND COMPLEXED Rb^+ IN ALKALIDES AND ELECTRIDES

4.1 Introduction

In the measurement of an X-ray absorption spectrum, the absorption coefficient, μ, of an absorber is monitored as a function of the energy of incident radiation. Typically, the low energy region of the spectrum shows a smooth linear increase in the absorption coefficient. Upon scanning the energy value corresponding to the binding energy of a particular core level in the absorbing atom, an abrupt increase in the absorption coefficient can be observed; this feature is known as an absorption edge of the specific absorber [53, 54]. The edge is produced by the absorption of an X-ray photon by one of the core electrons. If the electron excited is initially in the 1s core level, the absorption edge produced is a K-edge; the 2s state produces the L_1 - edge and the $2p_{3/2}$ and $2p_{1/2}$ states produce the L_3- and L_2- edges respectively. As a result of the absorption, the electron escapes the core level and propagates as an outgoing spherical wave originating in the absorber. For an absorber in a molecule or in a condensed

phase, a sinusoidal modulation of the absorption coefficient is observed at energies between 40 and 1000 eV above the absorption edge. This oscillatory modulation is known as the extended X-ray absorption fine structure or EXAFS. It results from the interference between the outgoing photoelectron wave and the backscattered waves originating in the neighboring atoms.

Although the fine structure has been known for over 50 years [65], its strength as a practical structural tool was not recognized until the work of Sayers, Stern and Lytle [66], in the early 1970's. In recent years, EXAFS spectroscopy has become a powerful tool used in the structural characterization of materials which cannot be studied by diffraction techniques, such as amorphous solids, liquids, solutions, gases and polymers. The analysis by EXAFS spectroscopy can determine local structural features such as the number and kind of neighboring atoms and their distances away from the absorber. Single crystals of the material are not required. In addition, if the intense synchrotron radiation is used, a spectrum can be collected in 10 to 20 minutes, a feature which makes this technique particularly valuable in the study of sensitive or unstable compounds. In fact, part of the success in establishing EXAFS as a valuable structural technique has been attributed to the development of the synchrotron radiation sources which allow fast collection of the data.

The most widely accepted theory used in the

interpretation of EXAFS spectroscopy data is the short-range, single-electron, single-scattering theory [53, 66, 67]. According to this formulation, the modulation of the absorption coefficient, χ, can be expressed in terms of the photoelectron wave vector k, as

$$\chi(k) = \sum_j N_j S_i(k) F_j(k) e^{-2\sigma_j^2 k^2} e^{-2r_j/\lambda(k)} \frac{\sin\{2kr_j + \phi_j(k)\}}{kr_j^2}$$

Equation 14

where $F_j(k)$ is the backscattering amplitude from each of the N_j neighboring atoms of type j, at a distance r_j away. The Debye-Waller factor, σ_j, takes into account thermal vibration and static disorder. $\phi_j(k)$ represents the total phase shift that modifies the photoelectron wave, and which is due to the potentials of the absorber and backscatterer. $S_i(k)$ represents the amplitude reduction factor due to many-body effects such as shake-up or shake-off processes at the central atom. The factor $e^{-2r_j/\lambda}$ accounts for inelastic losses in the scattering process, due to neighboring atoms and the medium in between; λ represents the electron mean free path. It should be noted that, essentially, the EXAFS expression consists of a sum of oscillatory terms, each of which is a function of the interatomic distance ($2kr_j$), and the phase shift $\{\phi_j(k)\}$, and is multiplied by an amplitude function $\{N_j F_j(k)\}$ that is modified by the reduction factors $S_i(k)$, $e^{-2\sigma_j^2 k^2}$ and $e^{-2r_j/\lambda(k)}$.

The analysis of the EXAFS data involves curvefitting the observed data with the phenomenological EXAFS equation (Equation 14). The ab initio backscattering amplitude and phase functions calculated by Teo and Lee [68] are fixed in the fitting procedure. From the fits, best values for the structural parameters r_j, σ_j, and N_j can be obtained. This analysis technique is known as best fit based on theory or BFBT [53, 69].

The parameter correlations which often result from the curve fitting can be subsequently quantified to give phase and amplitude correlation curves for each term in the EXAFS equation. These curves, together with the structural parameters for a suitable model compound, can be used to improve the accuracy of the data treated by the BFBT formalism. This procedure is known as the fine adjustment based on model compounds, or FABM [69].

In addition to the structural information contained in the EXAFS region of the absorption spectrum, the spectral features in the vicinity of the absorption edge (up to 40 eV beyond the edge) or X-ray absorption near-edge structure, XANES, can provide information on the chemical surroundings of the absorber. One of the near-edge features, the absorption threshold resonance, or white line, has been described as a dipole transition from a core electron to vacant bound states in the absorber [54]. The area of the white line has been correlated to the number of unfilled bound states in the absorber [70]. The position of the

absorption edge has also been used to obtain information about the chemical state of the absorber. The information provided by the near-edge structure, however, is only qualitative at this point. This region of the spectrum is modified by effects such as many-electron interactions, multiple scatterings and the core-hole potential. The theories developed to date contain approximations that neglect most of the complex interactions [54].

Our interest in the characterization and structural elucidation of alkalides and electrides led us to use the combined techniques of extended X-ray absorption fine structure (EXAFS) and X-ray absorption near edge structure (XANES). The strength of these combined techniques has been demonstrated recently by a number of studies that permitted structural determinations not possible by conventional diffraction techniques [52]. We report here the first structural study of a series of rubidium-containing alkalides and electrides by Rb K-edge EXAFS and XANES spectroscopy. Compounds with the stoichiometry RbNa(18C6), Rb(18C6), Rb_2(18C6), RbNa(15C5)$_2$, Rb(15C5)$_2$, Rb(15C5), RbK(C222), CsRb(18C6)$_2$, RbK(18C6), RbK(15C5)$_2$, CsRb(15C5)$_2$, RbC222 and Rb_2C222 were studied. When only a single crystalline phase is present, the combined use of EXAFS and XANES spectroscopies has provided a method of identifying the rubidium-containing species. It has also provided structural information about the complexed rubidium cation and the rubidide anion in alkalides and electrides.

4.2 Experimental

4.2.1 X-ray Absorption Measurements

Transmission X-ray measurements for Rb (K-edge at 15.201 KeV) were made at the Cornell High Energy Synchrotron Source (CHESS) [71] on the C2 EXAFS beam line. The synchrotron used electron-positron energies of 5.3 GeV and a storage ring injection current of 30 mA. A channel-cut Si (220) single crystal monochromator, detuned by 50% for harmonic rejection, was used. The spectra were recorded from 15.000 keV to 16.230 keV. This energy range was divided into five sections. In the pre-edge region (from 15.000 to 15.175 keV), points were collected at 25 eV intervals. For the XANES region (15.175 keV to 15.225 keV), the measurements were made at 0.5 eV intervals, while for the EXAFS region (15.225 - 15.286 keV), 1.2 eV intervals were used. For the range from 15.286 to 15.496 keV, the measurements were collected at 2.1 eV intervals, from 15.496 to 15.681 keV data points were measured every 2.9 eV, and from 15.681 to 16.230 KeV, points were obtained every 4.3 eV. The beam size was 1 x 13 mm^2. The incident and transmitted beam intensities were measured by ionization chambers of 8 and 30 cm in length, respectively, filled with argon (flow type). The monochromator was calibrated with an yttrium foil (K-edge at 17.037 keV [72]).

4.2.2 Sample Preparation and Handling

Polycrystalline (powder) samples of alkalides and electrides were synthesized in our laboratory as described in Chapter 2, and stored at reduced temperatures in sealed glass ampoules. These ampoules were opened just prior to each scan. To prevent decomposition, all sample handling was done in inert atmosphere (N_2 gas) glove bags equipped with a cold well immersed in a tray of liquid nitrogen. The polycrystalline samples were mixed with dry boron nitride powder by using a cold agate mortar and pestle and pressed to form a uniform pellet of suitable thickness ($\mu\chi \sim 1.0$). The stainless steel sample cells, of dimensions 3-1/2 x 4-1/2 x 15 mm,[3] were sealed with 1-mil Kapton tape.

In order to maintain the samples cold and under an inert atmosphere during data collection, a sample holder-cryostat was designed. This air-tight cryostat, shown in Figure 15, was made of acrylic sheets, and contains three compartments through which prepurified nitrogen gas flows. The central compartment contains the sample holder and is maintained at temperatures $\leq$ -35°C during data collection. The two adjacent compartments are continuously flushed with dry nitrogen gas at room temperature to insure a frost-free beam path. Mylar tape was used on all windows in the X-ray path. A frame of lead adhesive tape around the beam entry and exit ports insured proper alignment of the cryostat with respect to the beam. A polyethylene glove bag around the whole assembly (but not in the beam path) prevented

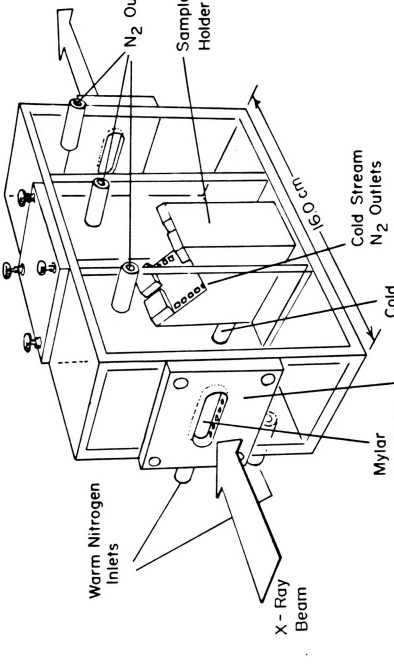

Figure 15. Sample-holder cryostat used in the X-ray absorption measurements.

contamination of the atmosphere in the cryostat when changing samples.

Before inserting the first sample, the sample chamber was purged with dry nitrogen at room temperature. After this, a cold nitrogen stream was used in the central chamber. The sample holder has a series of channels that allowed the stream of cold gas to flow directly over the sample, thus insuring that it was maintained cold and frost-free during the scan.

The salts $Rb^+(18C6)\cdot SCN^-$ and $Rb^+(18C6)\cdot Br^-\cdot 2H_2O$ are stable and were used as reference compounds to model the structure of the complexed rubidium cation. The structures of these two salts are known from single crystal X-ray diffraction studies [73].

After each run, the alkalide and electride samples were allowed to react with air to produce the corresponding hydroxides. Spectra of the oxidized materials were then scanned for comparison with the pristine samples.

4.2.3 Data Analysis

The analysis of the XANES and EXAFS data was carried out at AT & T Bell Laboratories, Murray Hill, with Dr. B. K. Teo. All calculations were performed on a Digital PDP 11/34 computer with local programs.

The X-ray absorption data were collected as plots of $\mu X = \ln(I_o/I)$ vs. E. For optimum background removal the plots were truncated at 16050 eV. To be able to extract the structural information from the EXAFS data it is essential

to transform the raw data into a function of the electron wave vector, k, which is defined as

$$k = \{ 2m (E - E_o) / \hbar^2 \}^{1/2} \quad (15)$$

where E_o is the energy threshold of the rubidium K-edge and m is the mass of the electron [53, 69]. The E_o value was measured for each compound from the raw data. It was consistently taken as the photon energy at half-height of the "edge jump". The edge jump is the step, $\Delta\mu X$, at the absorption edge. It is measured by extrapolating the EXAFS region into the edge, ignoring the white line. These threshold energies were found to be 15195 ± 1 eV for all those compounds that contain either the simple rubidium cation or the complexed rubidium cation in the form $Rb^+(18C6)$ or $Rb^+(15C5)_2$. However, because the calibration foil (yttrium) had an edge energy nearly 2 KeV higher than that of rubidium, the absolute accuracy of the threshold energy could not be ascertained. The phase functions are unique only when a particular energy threshold is specified. The experimentally chosen value of E_o may not be consistent with the theoretical E_o's for each of the different types of neighbors for which the theoretical phase shifts are defined [67]. A different E_o value must be allowed for each type of neighboring atom [68, 69, 74]. A practical solution to this problem is to least-squares refine

$$\Delta E_{oj} = E_{oj}^{th} - E_o^{exp} \quad (16)$$

in

$$k_j = \{ k^2 - 2(\Delta E_{oj})/7.62\}^{1/2} \qquad (17)$$

where k is the experimental wave vector with experimental threshold energy E_o^{exp} and k_j is the theoretical wave vector with theoretical threshold energy E_{oj}^{th} for atom j. ΔE_{oj} is one of the parameters refined in the BFBT calculations.

After the data had been transformed to k-space, the points were multiplied by k^3 and the background was removed by using a cubic spline technique [75, 76]. Five sets (ca. 2.92 A^{-1} each) of cubic spline functions were used. The resulting EXAFS curves, in the form $k^3\chi(k)$ vs. k, were normalized by dividing by the edge jump and corrected for the absorption decay by using Victoreen's true absorption equation [77],

$$\mu/\rho = C\lambda^3 - D\lambda^4 \qquad (18)$$

where μ/ρ is the mass absorption coefficient, λ is the wavelength of incident radiation and C and D are parameters characteristic for the absorbing atom with C = 374 and D = 174 for rubidium. The data were then truncated at 1.0 and 12.0 A^{-1}. The EXAFS data were at this point Fourier transformed [78], followed by Fourier filtering by using a window function (0.8 - 8.0 A), in order to remove the high frequency noise and the residual background [75, 78]. The filtered data were inverse transformed back to k-space and subsequently truncated at 2.0 and 10.0 A^{-1}. The data were then fit by using a nonlinear least-squares procedure. A

two term fit was performed by using Equation 14 in the form [74],

$$k^3\chi(k) = \sum_j B_j F_j(k_j) k_j^2 e^{-2\sigma_j^2 k_j^2} \frac{\sin[2k_j r_j + \phi_j(k_j)]}{r_j^2} \quad (19)$$

where all the variables are as previously defined. For K-edge absorption, the phase function, ϕ_j, has the form

$$\phi_j = \phi_i^a + \phi_j^b - \pi \quad (20)$$

where ϕ_i^a is the absorber phase function, ϕ_j^b is the backscatterer phase function and the term $-\pi$ is introduced to take care of an overall minus sign. The scale factor B_j is given by

$$B_j = N_j A_j \quad (21)$$

where A_j is defined as a general amplitude reduction factor,

$$A_j(k) = S_i(k) e^{-2r_j/\lambda(k)} \quad (22)$$

$S_i(k)$ tends to reduce the EXAFS amplitude at high k, while $e^{-2r_j/\lambda(k)}$, because of the k dependence of $\lambda(k)$, attenuates the amplitude more at low k. Thus, $A_j(k)$ can be approximated by the scalar A_j, which varies for different coordination shells. If the amplitude reduction factor A_j is known, the number of bonds N_j can be calculated from the fitted scale factor B_j [69].

Eight parameters were varied on each fit: two

distances, r_j (for example, r_O and r_C, corresponding to distances Rb^+ - O and Rb^+ - C respectively), two threshold energy differences, ΔE_{oj}, two Debye-Waller factors, σ_j, and two scale factors, B_j. The results of the fits of the data are described in the next section.

Inaccuracies in the determination of distance and coordination numbers by the BFBT method are caused by experimental errors and approximations inherent in the EXAFS model, and by parameter correlations in the nonlinear least-squares curve fitting, especially, between ΔE_o and r, and between σ and B or N within each term. The fine adjustment based on models or FABM is aimed at improving the accuracy of the best fit values by using the correlations in the parameters [69]. The FABM method is based on the measurement and analysis of the EXAFS spectra of one or more model compounds. The model(s) must contain the same set of neighboring atoms. It is not necessary to use a single model compound with all the same neighbors expected in the unknown; several models can be used, as long as each absorber-scatterer pair of the unknown is represented by at least one model compound. The experimental conditions used for the collection of the data, as well as the treatment subsequently applied for the analysis must be identical for model and unknown.

The FABM technique involves performing a series of fits by setting the distance being refined at different values up to ± 0.10 A away from the best fit value, while

allowing the remaining parameters within the same term to vary during the least-squares cycles. All parameters associated with the other term are held constant at their best fit values. The parameters allowed to refine are ΔE_o, σ, and the scale factor of the particular term. Following this, ΔE_o is plotted as a function of r, to obtain distance correlation curves [69, 79]. The characteristic ΔE_o for the model is obtained from the curve at the crystallographic value r_m. ΔE_o is then transferred to the unknown to determine its corrected distance, r. The ΔE_o vs. r plots are usually linear; thus, very accurate distance values can be obtained by using linear regression to fit the ΔE_o vs. r data.

A procedure analogous to that described is used for the fine adjustment of coordination numbers, except that for this case, the Debye-Waller factor of one term is given different values ranging from 0 to σ_m, while keeping the parameters of the other term at their best fit values. A subsequent plot of B vs. σ will allow direct determination of the B value of the unknown, by using the best fit Debye-Waller factor for the model σ_m.

It should be noted that, while the BFBT procedure is model independent, the FABM method depends very strongly on the use of effective model compounds.

4.3 Results and Discussion

The rubidium K-edge X-ray absorption spectrum, $\mu\chi$ vs. E (eV) of $Rb^+(15C5)_2 \cdot Na^-$ is shown in Figure 16(a). This spectrum exhibits features typical of those alkalides and electrides that contain the complexed rubidium cation. Similar features, namely, a sharp K-edge absorption threshold resonance (white line) and fine structure extending up to 300 eV above the edge, are observed in the spectra of the model compounds $Rb^+(18C6) \cdot SCN^-$, and $Rb^+(18C6) \cdot Br^- \cdot 2H_2O$, (Figure 17) as well as in the spectra of alkalides and electrides that contain $Rb^+(18C6)$ or $Rb^+(15C5)_2$. The spectra are illustrated in Figures 16-20. Very different features are observed in the EXAFS spectrum of $Cs^+(18C6)_2 \cdot Rb^-$, shown in Figure 21(a). The intensity of the white line is considerably smaller and the fine structure is absent. These differences in the spectra point to the difference in the oxidation state and environment of rubidium in these two types of compounds. The spectrum of the rubidide, $Cs^+(18C6)_2 \cdot Rb^-$, is remarkably similar to that of Kr gas [54]. The white line, which is due to transitions from core to vacant bound excited states and is a measure of the density of such states, is virtually absent, indicating the low density of vacant, bound excited states. Also, there is no discernible EXAFS, a result of the large size of Rb^-. The radius of this anion has been estimated to be 3.4 A, which would give a minimum interionic distance of 4.9 A [6]. The similarity in the spectra of Kr gas and

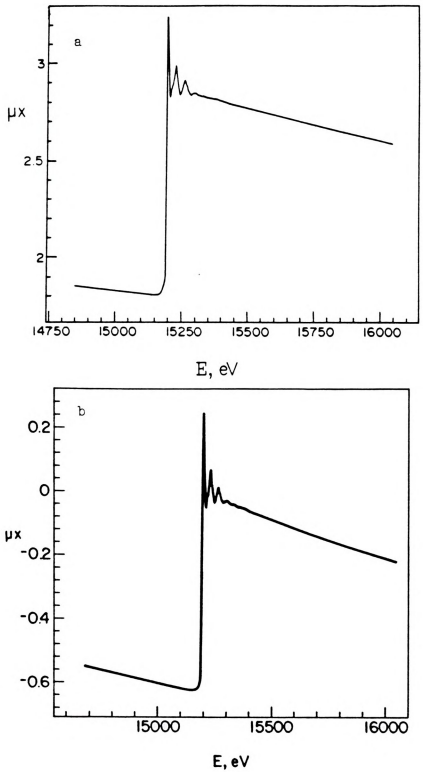

Figure 16. Rb K-edge transmission X-ray absorption spectra of (a) $Rb^{+}(15C5)_2Na^{-}$ and (b) $Rb^{+}(15C5)_2e^{-}$.

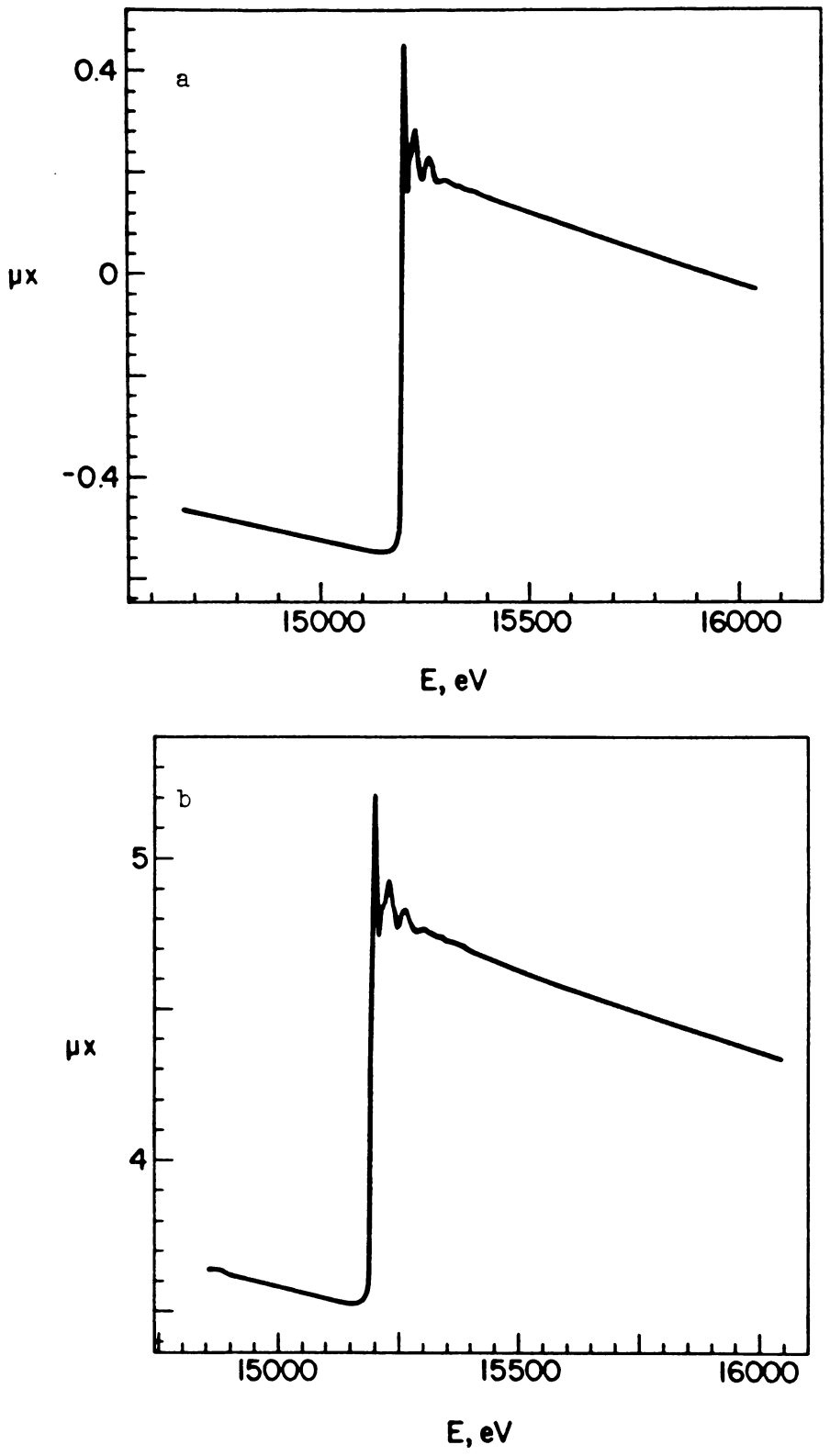

Figure 17. Rb K-edge transmission X-ray absorption spectra of (a) $Rb^{+}(18C6)SCN^{-}$ and (b) $Rb^{+}(18C6)Br^{-}\cdot 2H_2O$.

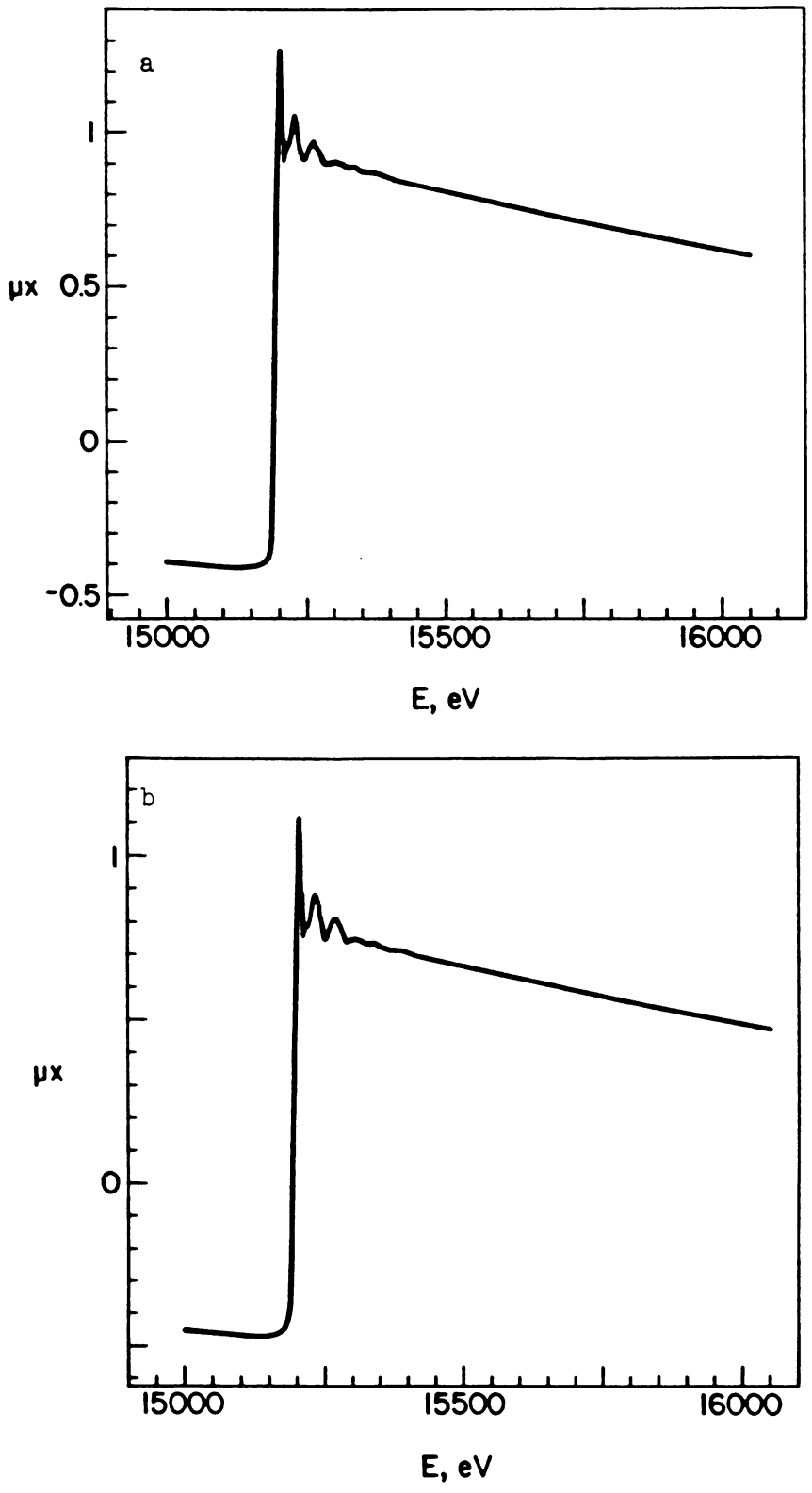

Figure 18. Rb K-edge transmission X-ray absorption spectra of (a) $Rb^{+}(15C5)_2Rb^{-}$ and (b) $Rb^{+}(18C6)Na^{-}$.

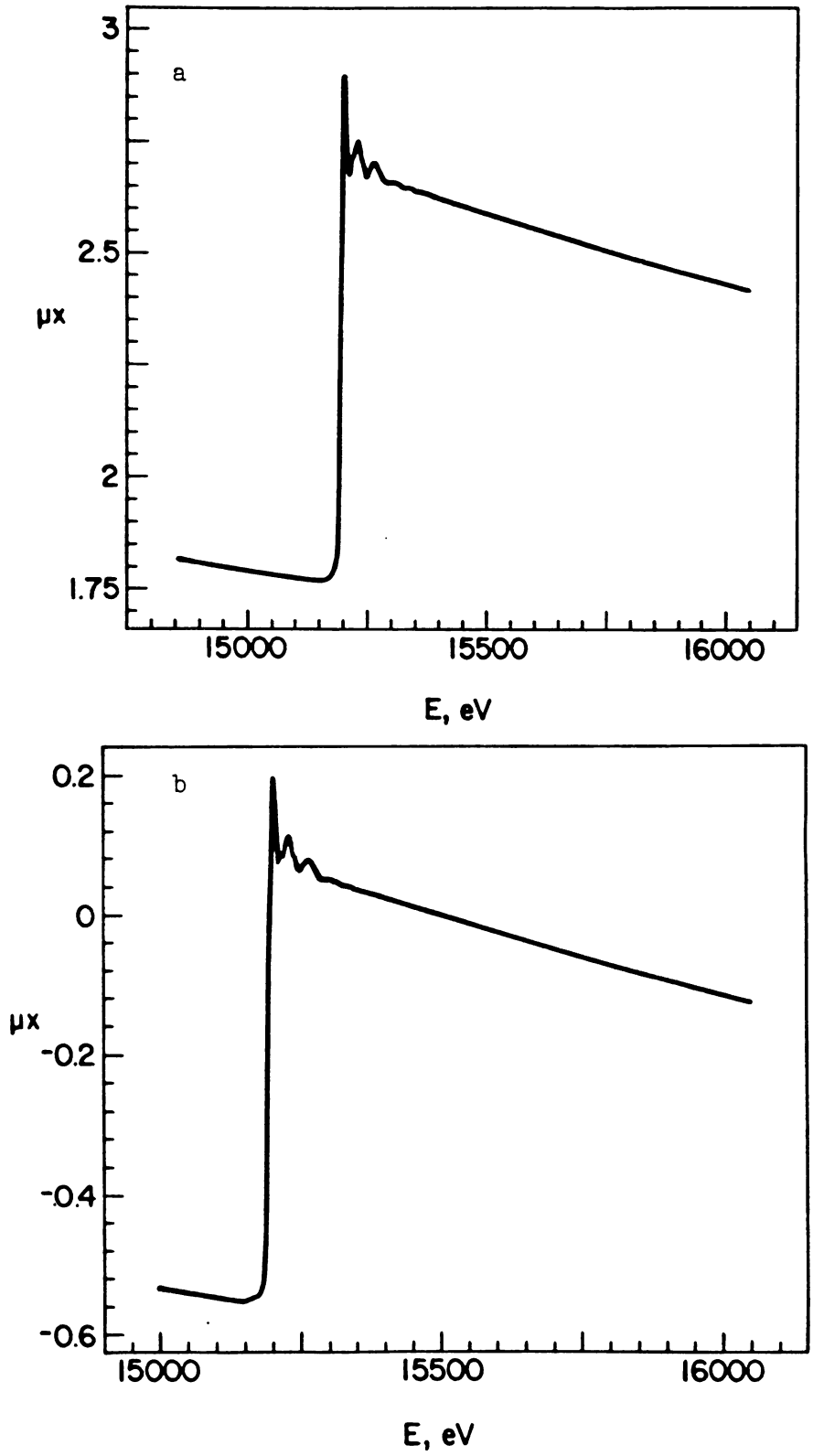

Figure 19. Rb K-edge transmission X-ray absorption spectra of (a) Rb(18C6) and (b) $Rb^{+}(18C6)Rb^{-}$.

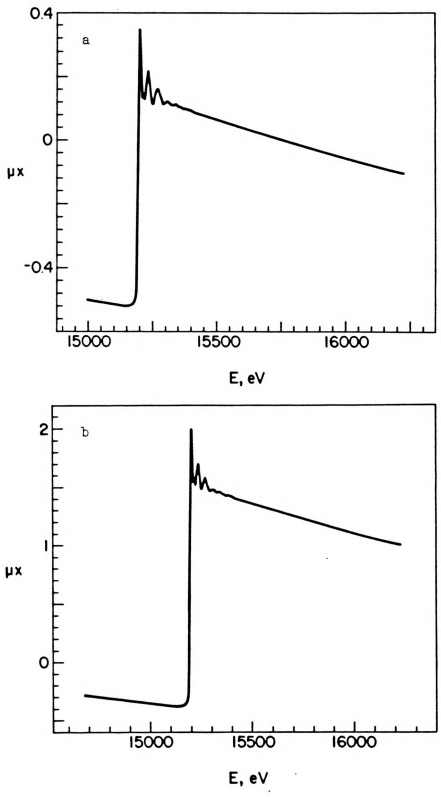

Figure 20. Rb K-edge transmission X-ray absorption spectra of (a) $Rb^{+}C222e^{-}$ and (b) $Rb^{+}C222Rb^{-}$.

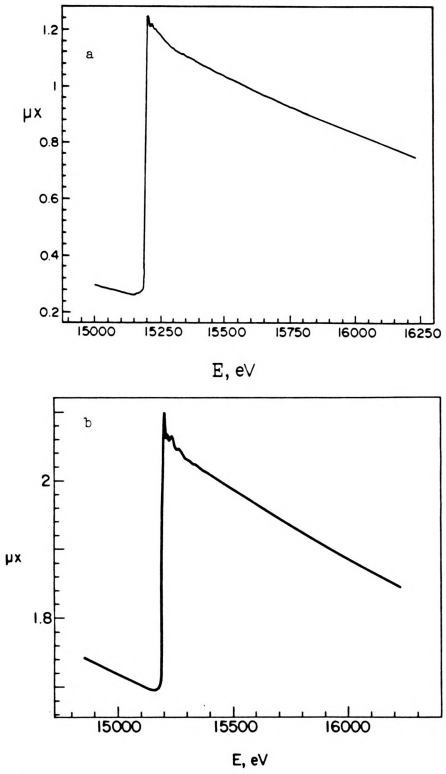

Figure 21. Rb K-edge transmission X-ray absorption spectra of (a) $Cs^{+}(18C6)_2Rb^{-}$ and (b) $K^{+}C222Rb^{-}$.

$Cs^+(18C6)_2 \cdot Rb^-$ confirms that the rubidide anion in the solid is a large spherical anion with no atomic or ionic species in close proximity. This type of environment for alkali metal anions has been observed in the crystal structures of the three sodides referred to earlier. Additional evidence in support of this description of the rubidide anion has been obtained from results of magic angle sample spinning NMR experiments [63].

The X-ray absorption spectra of $K^+C222Rb^-$ and $Cs^+(15C5)_2Rb^-$, illustrated in Figures 21(b) and 22, also exhibit the features characteristic of a pure rubidide.

4.3.1 XANES and White Line Areas

The rubidide anion has an electronic configuration that consists of a krypton core and two electrons in the 5s orbital. For K-edge absorption, where the initial state has s-symmetry and zero angular momentum, the dipole selection rule of $\Delta\ell=\pm1$ allows only a single important final state of $\ell=1$ with p-symmetry [54]. The observed white line in complexed Rb^+ can therefore be attributed largely to a dipole-allowed transition from the 1s to a bound 5p orbital in the molecular cage defined by the first shell of ligands. It is the confining effect of the cage potential in "inner well" unoccupied orbitals that enhances the oscillator strength of transitions to these orbitals [80]. In the rubidide, Rb^-, where the cage is no longer present, the 5p orbital is very diffuse, thereby giving rise to a weak oscillator strength for the dipole transition. In this

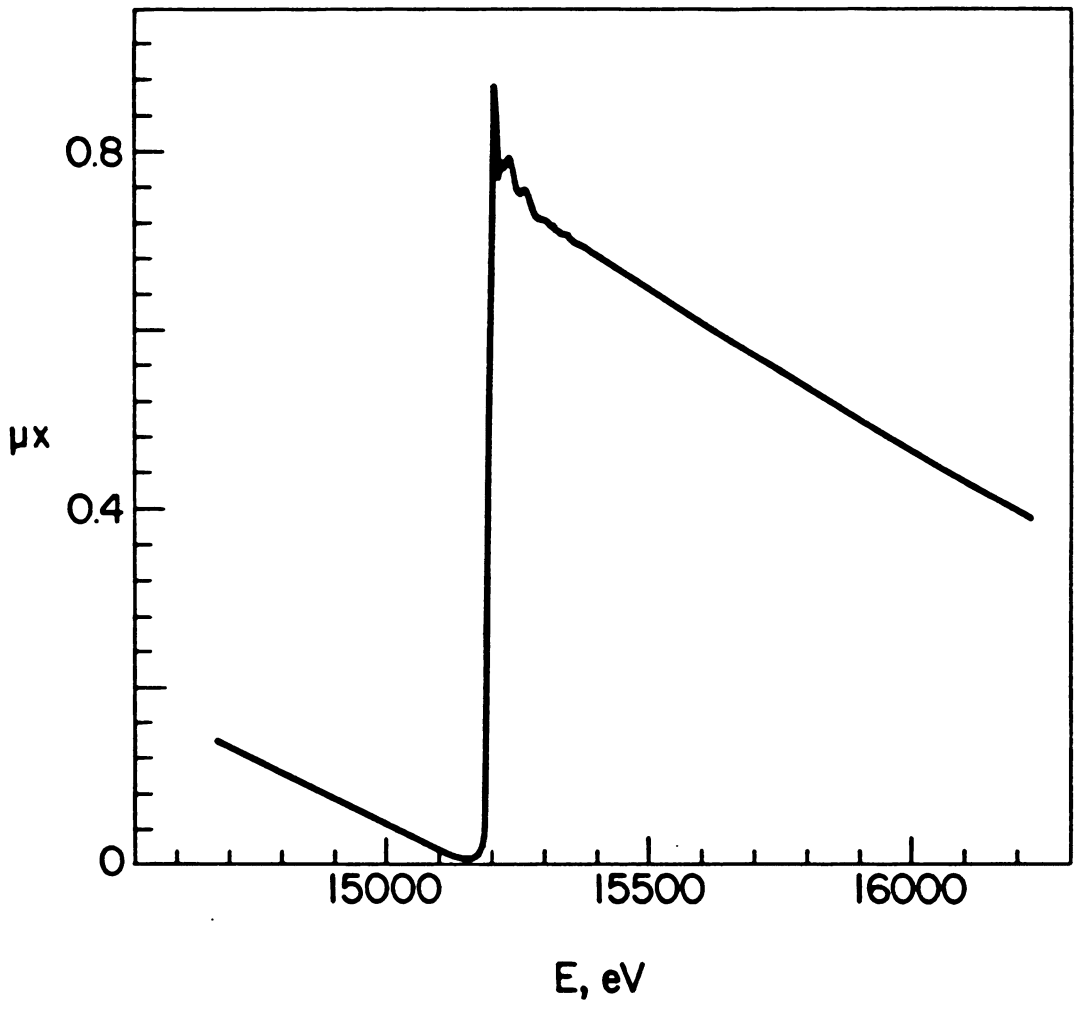

Figure 22. Rb K-edge transmission X-ray absorption spectrum of $Cs^{+}(15C5)_2Rb^{-}$.

regard, it should be pointed out that the 5p orbital in complexed Rb^+ is also much more tightly bound than in Rb^-.

These observations led to the conclusion that the areas of the white lines can be used to diagnose the oxidation state(s) of the absorbing rubidium species in alkalides and electrides. With this in mind, the areas of the white lines for all compounds studied were measured and normalized to unit edge jump. The results are presented in Table 2. The units (10^{-2} cm) are arbitrary and will be disregarded in the discussion that follows.

The compounds that contain only the complexed rubidium cation exhibit the largest white line areas, with values ranging from 19 to 27, close to those of the oxidized samples (27-36). On the other hand, the smallest white line areas are those of compounds that only contain rubidium as an anion, such as $Cs^+(18C6)_2 \cdot Rb^-$ and $K^+C222 \cdot Rb^-$. Between these two extremes are compounds that contain both the complexed rubidium cation and the rubidide anion, such as $Rb^+(18C6) \cdot Rb^-$ and $Rb^+(15C5)_2 \cdot Rb^-$. The white line areas, A=12 and 18 respectively, are approximately half the values observed for similar salts that contain only complexed Rb^+. This is consistent with the fact that in these rubidides only half the rubidium exists as Rb^+. Finally, the heteronuclear alkalides, $RbK(15C5)_2$ and RbK(18C6) (A=16 and 10) exhibit values lower than expected for the complexed rubidium cation but higher than those of pure rubidides. This suggests that they are mixtures of all or some of the

Table 2. Normalized Areas of White Line (cm x 10^2)

Compound	Pristine sample	Decomposed sample
RbCl	19	--
RbBr	15	--
$Rb^+(18C6)\cdot SCN^-$	27	--
$Rb^+(18C6)\cdot Br^-\cdot 2H_2O$	25	--
$Rb^+(15C5)_2\cdot Na^-$	29	34
$Rb^+(15C5)_2\cdot e^-$	32	39
$Rb^+(18C6)\cdot Na^-$	19	29
$Rb^+(15C5)_2\cdot Rb^-$	18	31
$Rb^+(18C6)\cdot Rb^-$	12	30
Rb(18C6)	16	30
$RbK(15C5)_2$	16	34
RbK(18C6)	10	35
$Rb^+C222\cdot Rb^-$	14	33
$Rb^+C222\cdot e^-$	22	29
$K^+C222\cdot Rb^-$	4	27
$Cs^+(18C6)_2\cdot Rb^-$	1	29
$Cs^+(15C5)_2\cdot Rb^-$	7	38

salts $Rb^+C \cdot K^-$, $K^+C \cdot Rb^-$, $Rb^+C \cdot Rb^-$ and $K^+C \cdot K^-$, where C represents the complexant. Magic angle sample spinning NMR data on K^- and Rb^- agree with this conclusion [63, 81].

In general, the $Rb^+(15C5)_2 \cdot X^-$ salts, which have Rb^+ sandwiched in a three dimensional trap formed by two 15-crown-5 rings, exhibit larger white line areas than those of either $Rb^+(18C6) \cdot X^-$ salts or simple rubidium salts such as Rb^+Cl^-. In the former non-sandwich crown ether salt, the rubidium cation is displaced from the mean plane of the ligand and is thus exposed to the anions. These results suggest that when the anion can come into contact with Rb^+ it can donate electronic charge more readily and thus decrease the density of available final states for the 1s → 5p transition.

The identification of the rubidium-containing species present in the salt of nominal stoichiometry Rb(18C6) poses a special problem. This stoichiometry represents more than one possible complex, i.e., $Rb^+(18C6) \cdot e^-$, a pure electride, or $Rb^+(18C6)_2 \cdot Rb^-$, a rubidide with two crown ether rings complexing the cation. Initial efforts to identify the species present involved optical spectroscopy studies of thin films of the compound prepared from a solution of the crystals in methylamine [59]. However, a definitive identification of the species present was not obtained. The films exhibited broad absorption bands at 11,600 cm^{-1} and 8,900 cm^{-1}, characteristic of Rb^- and the trapped electron respectively. The fact that the same features were also

observed in the optical spectra of films of $Rb_2$18C6 made identification difficult. More recently, rubidium-87 solid state magic angle sample spinning NMR experiments [59, 63] have identified the presence of the rubidide anion in some alkalides. However, for some homonuclear alkalides of the form $Rb^+C \cdot Rb^-$ where C=18C6 and C222, no NMR signals were observed for either the rubidide or the complexed rubidium cation, although both must have been present. Thus, NMR results can also be ambiguous. In particular, some samples of stoichiometry Rb(18C6) showed the presence of Rb^- while others did not.

Both XANES and EXAFS data for Rb(18C6) suggest the presence of the rubidium anion in the crystals. There is no appreciable difference in the area of the white line measured for Rb(18C6) compared to that of $Rb^+(18C6) \cdot Rb^-$. The value falls in the intermediate range of areas that correspond to mixtures of Rb^+ and Rb^-. Thus it is likely that the crystallites under study contain mixtures of both rubidium electride and rubidide. However, an alternate possibility cannot be ruled out; namely, that the small white line area in Rb(18C6) is a result of large electron density donation from the trapped electron to the exposed cation.

4.3.2 Edge Shifts:

The absorption edge threshold values for complexed rubidium in compounds that contain the $Rb^+(18C6)$ or $Rb^+(15C5)_2$ moieties were compared to those of salts that

contain rubidium only in the anionic state. For example, in the pure rubidide, $Cs^{+}(18C6)_2 \cdot Rb^{-}$, the edge is shifted to lower energies by 3 eV, compared to that of compounds which contain only Rb^{+}, reflecting the smaller energy required to remove the 1s electron to an outer state in the anionic species. The magnitude of the shift is, however, smaller than would have been predicted for a change in charge of two units (from Rb^{+} to Rb^{-}) in a completely ionic environment [82] or in the gas phase. A possible explanation is that the magnitude of electron pair donation from the oxygens of the crown ether to the complexed rubidium cation is such that the actual negative charge in the vicinity of the cation is not as different from that of Rb^{-} as would be deduced from the formal charge difference.

4.3.3 EXAFS and Structures

The Fourier transforms of the normalized EXAFS $k^3\chi(k)$ vs. k for the rubidium K-edge in $Rb^{+}(15C5)_2 \cdot Na^{-}$, $Rb^{+}(15C5)_2 \cdot e^{-}$ and $Rb^{+}(15C5)_2Rb^{-}$ are shown in Figures 23-25. These have not been corrected for the phase shift, so the peaks appear at distances that are somewhat shorter than the true distances. Note that these Fourier transforms show two broad peaks centered at 2.5 A and 3.5 A. The structure of $Rb^{+}(15C5)_2 \cdot Na^{-}$ has been determined by using single crystal X-ray diffraction methods as will be discussed in Chapter 5. In this compound the rubidium cation is sandwiched between two 15-crown-5 rings, and has as nearest neighbors ten oxygen atoms from the crown rings (Rb-O 2.99-3.07 A, average

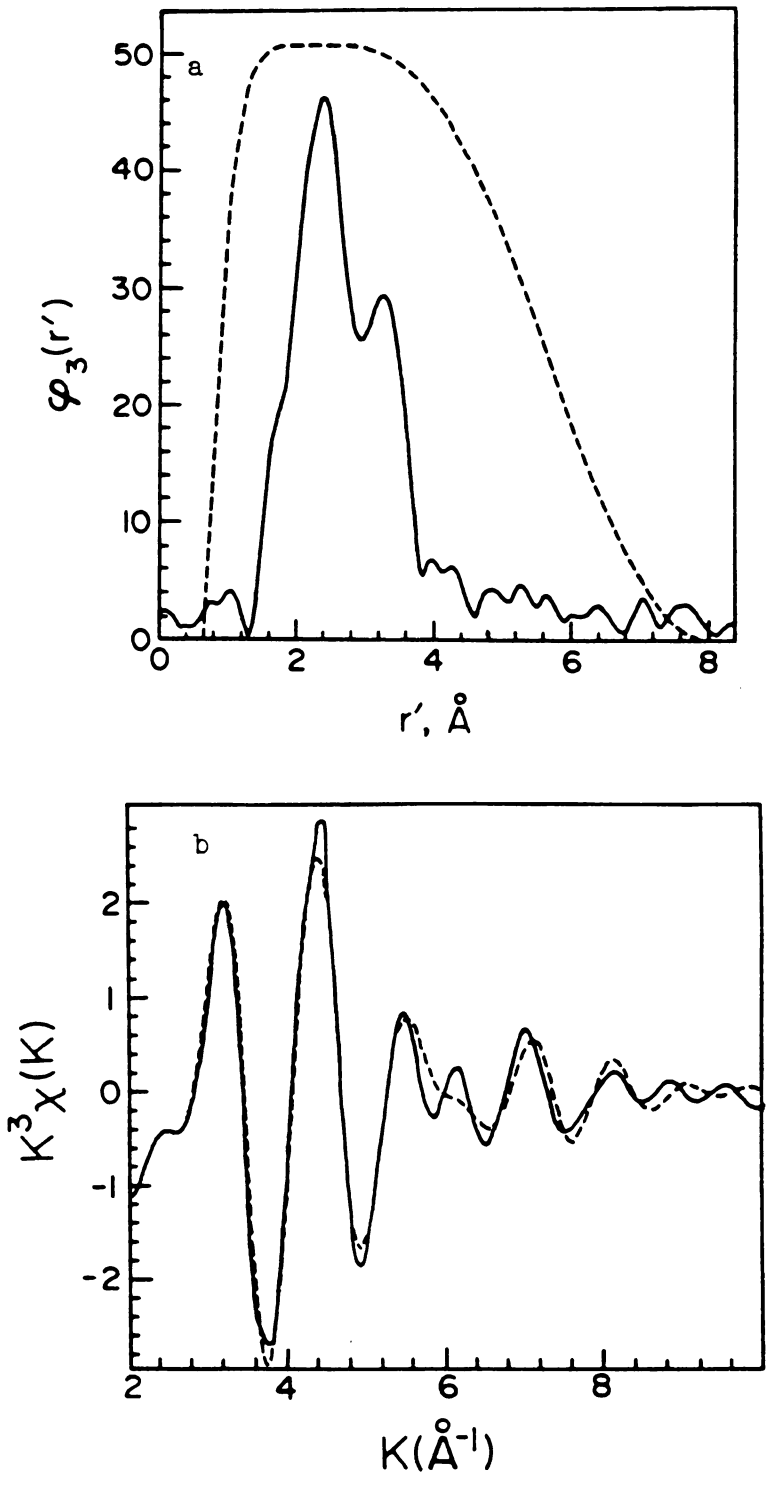

Figure 23. (a) Fourier transform (solid curve) of the Rb K-edge EXAFS, $k^3\chi(k)$ vs. k, and filtering window (dashed curve) for $Rb^+(15C5)_2Na^-$; (b) Fourier filtered EXAFS spectrum (solid curve) and best fit based upon theory (dashed curve).

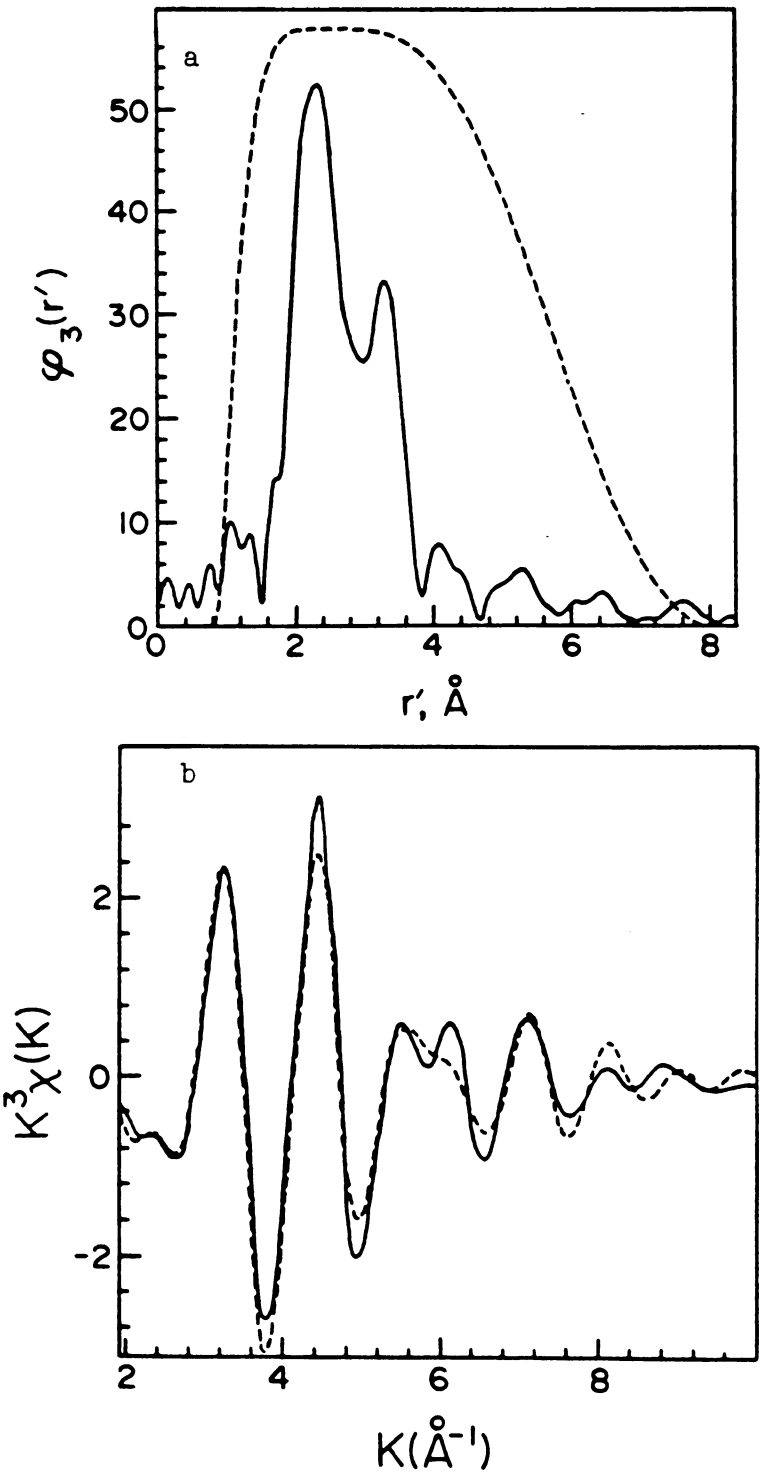

Figure 24. (a) Fourier transform (solid curve) of the Rb K-edge EXAFS, $k^3\chi(k)$ vs. k, and filtering window (dashed curve) for $Rb^+(15C5)_2e^-$; (b) Fourier filtered EXAFS spectrum (solid curve) and best fit based upon theory (dashed curve).

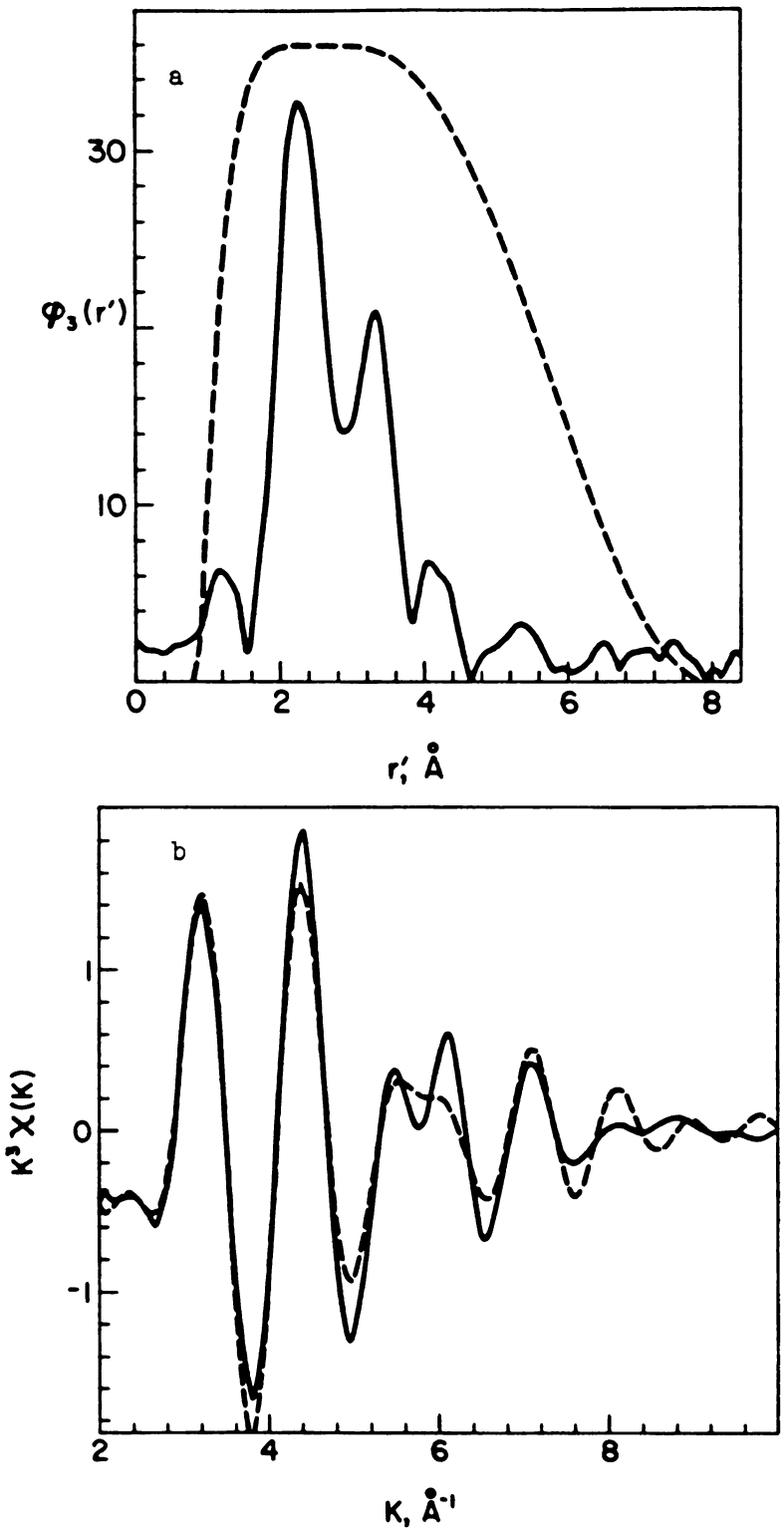

Figure 25. (a) Fourier transform (solid curve) of the Rb K-edge EXAFS, $k^3\chi(k)$ vs. k, and filtering window (dashed curve) for $Rb^+(15C5)_2Rb^-$; (b) Fourier filtered EXAFS spectrum (solid curve) and best fit based upon theory (dashed curve).

3.01 A). The cation is fully protected by the rings, and has no contact with the anion. The closest approach between the cation and the sodide anion is 7.49 A. The peak observed at 3.5 A corresponds to a shell of carbon neighbors from the 15-crown-5 ring. There are twenty such neighbors at an average distance of 3.82 A. The similarities in the positions and magnitudes of the peaks suggest a similar local structure for the rubidium cation in $Rb^{+}(15C5)_2 \cdot Na^{-}$ and $Rb^{+}(15C5)_2 \cdot e^{-}$. Similar long distances for Rb^{+} to anion contacts are to be expected for $Rb^{+}(15C5)_2 \cdot Rb^{-}$. However, EXAFS cannot provide such long distance values. As expected for an electride salt, the FT's of $Rb^{+}(15C5)_2 \cdot e^{-}$ do not show distances corresponding to the anion.

The dashed curves shown in Figures 23-25(a) are the window functions used to filter the backscattering contributions from the distance space (A) before Fourier inverse transformation of the data back to k-space (A^{-1}). The Fourier-filtered data, $k^3\chi$ vs. k in the region from 2.0 to 10.0 A are shown as solid curves in Figures 23-25(b). The filtered EXAFS spectra were then resolved into two terms to account for a shell of oxygen nearest neighbors and an outer shell of carbon neighbors and were least-squares fit with the single- electron, single- scattering formalism of the EXAFS effect, Equation 19. The best fits based upon theory, BFBT are depicted as dashed curves in Figures 23-25(b). The resulting 'best fit' (BFBT) least-squares refined parameters are presented in Table 3. These values

Table 3 : Best Fit (Based on Theoretical Functions) Least-Squares Refined Interatomic Distances r(A), Debye-Waller Factors σ(A), and Energy Threshold Differences ΔE_o(eV)

Compound	Term	r	σ	ΔE_o
$Rb^+(15C5)_2 \cdot Na^-$	Rb-O	2.99	0.155	2.43
	Rb-C	3.87	0.120	4.34
$Rb^+(15C5)_2 \cdot e^-$	Rb-O	2.97	0.150	3.14
	Rb-C	3.88	0.105	4.50
$Rb^+(15C5)_2 \cdot Rb^-$	Rb-O	2.96	0.146	3.30
	Rb-C	3.88	0.104	5.08
$Rb^+(18C6) \cdot SCN^-$	Rb-O	2.99	0.126	3.52
	Rb-S	3.48	0.0916	2.35
	Rb-C	3.96	0.0728	7.55
$Rb^+(18C6) \cdot Br^- \cdot 2H_2O$	Rb-O	3.00	0.132	3.79
	Rb-Br	3.46	0.0769	0.0160
	Rb-C	3.94	0.0769	6.43
$Rb^+(18C6) \cdot Na^-$	Rb-O	2.93	0.135	3.88
	Rb-C	3.85	0.0952	6.18
Rb(18C6)	$Rb\text{-}O_1$	2.99	0.144	4.15
	$Rb\text{-}O_2$	3.64	0.0664	-0.120
	Rb-C	3.95	0.0664	8.25
$Rb^+(18C6) \cdot Rb^-$	$Rb\text{-}O_1$	2.90	0.123	3.81
	$Rb\text{-}O_2$	3.60	0.0474	-0.342
	Rb-C	3.91	0.0474	8.69

illustrate the structural similarity of the $Rb^+(15C5)_2$ moiety in these salts. The data were further refined by using the Fine Adjustment Based on Models (FABM) formalism [69]. The distance correlation curves are illustrated in Figures 31 and 33. The B vs. σ correlation curves are shown in Figures 32 and 34. The resulting values, presented in Table 4, agree with those from theory. Note that there is a slight shortening in the Rb-O distances in the order sodide > electride > rubidide, with the rubidide having the shortest Rb-O distances. This suggests that in this salt the rubidium cation is least perturbed by the anionic species.

The radial distribution functions (not corrected for phase shift) for $Rb^+(18C6)\cdot SCN^-$, $Rb^+(18C6)Br^-\cdot 2H_2O$, $Rb^+(18C6)\cdot Na^-$, $Rb^+(18C6)\cdot Rb^-$, and Rb(18C6) are presented in Figures 26-30(a). For the thiocyanate salt {Figure 26(a)}, peaks are observed at 2.5 A, 3.1 A, and 3.6 A, which correspond to Rb-O, Rb-S, and Rb-C distances respectively. In this compound, Rb^+ is coordinated to six oxygens of the crown ether (Rb-O, 2.93 - 3.15 A) and to two thiocyanate anions (Rb-N(S), 3.23 and 3.31 A) [73]. In the case of the sodide, $Rb^+(18C6)\cdot Na^-$ (Figure 28), there is no peak in the radial distribution function at distances between those of Rb-O and Rb-C. This suggests that the structure of $Rb^+(18C6)\cdot Na^-$ is different from that of the model thiocyanate, in that there are no close contacts with the sodium anion, and only the contacts to oxygens and carbons

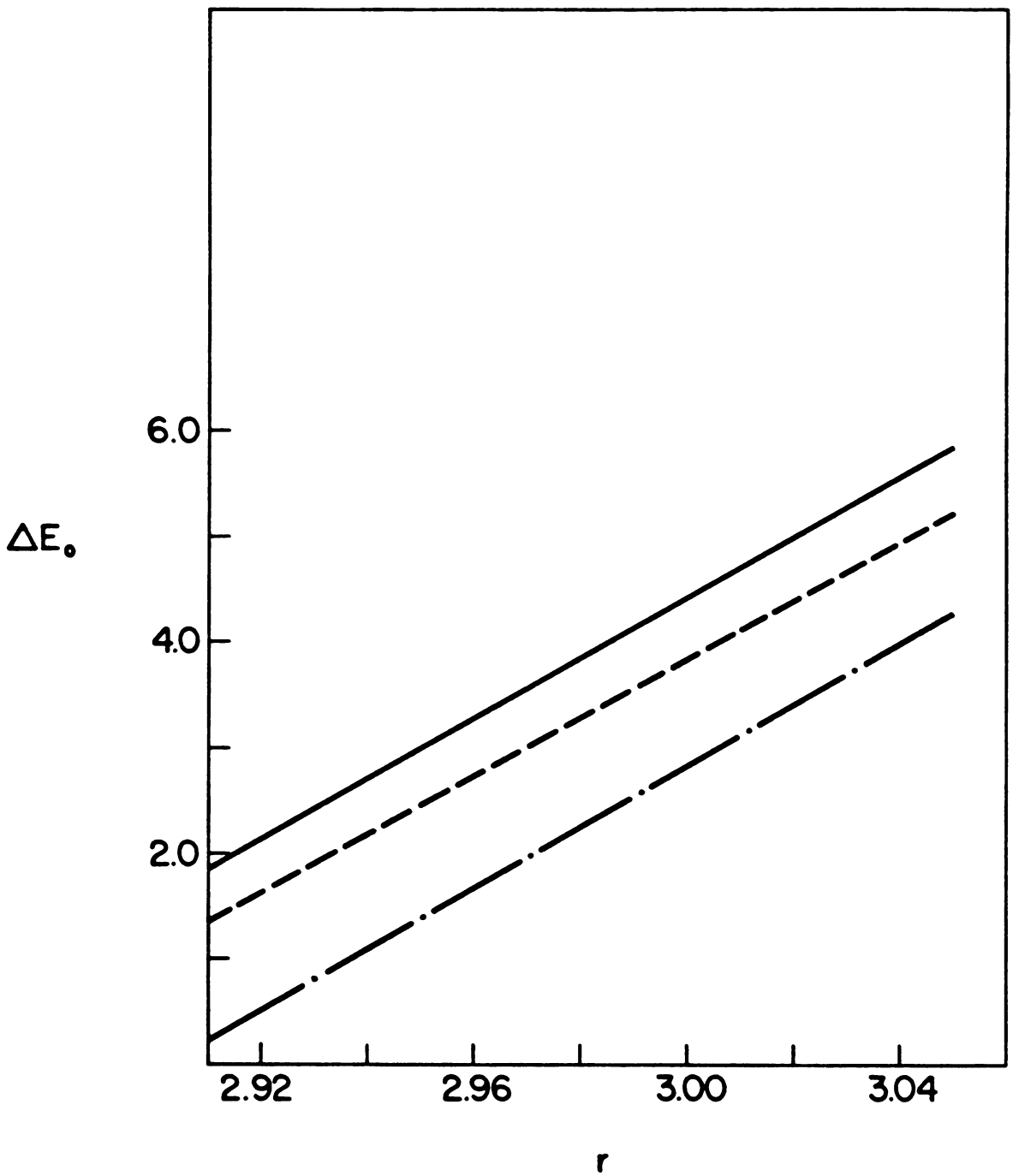

Figure 31. Parameter correlation curves ΔE_o vs. r for the Rb^+ - O terms of ——— $Rb^+(15C5)_2Rb^-$, ----- $Rb^+(15C5)_2e^-$, and ·—·—· $Rb^+(15C5)_2Na^-$.

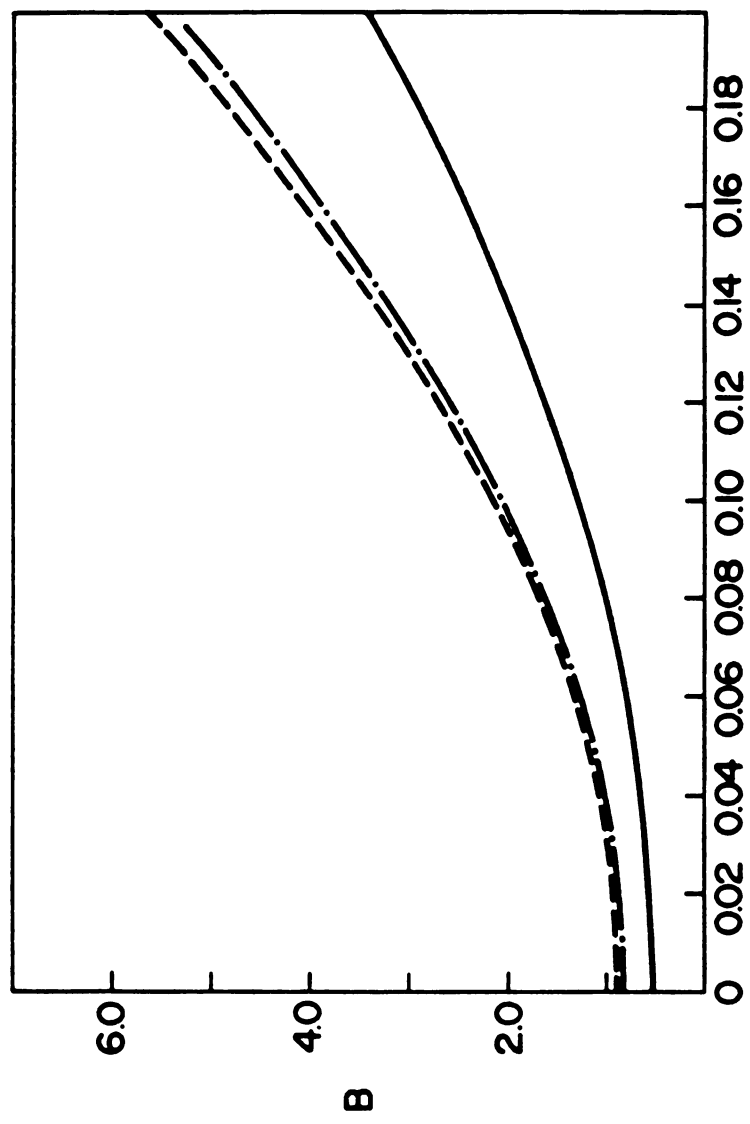

Figure 32. Parameter correlation curves B vs. σ for the Rb^+ - O terms of —— $Rb^+(15C5)_2Rb^-$, - - - - $Rb^+(15C5)_2e^-$, and ·—·—· $Rb^+(15C5)_2Na^-$.

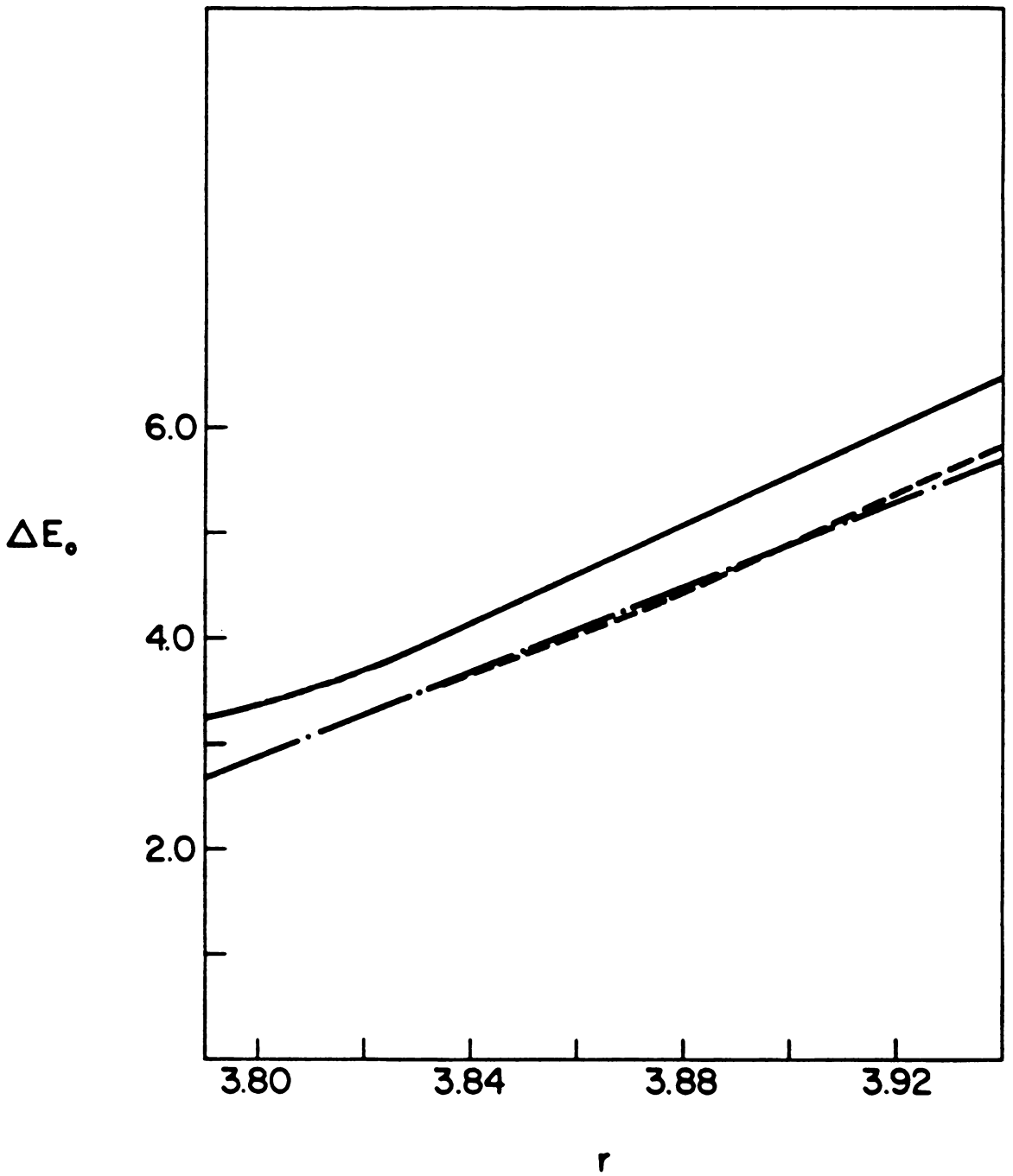

Figure 33. Parameter correlation curves ΔE_o vs. r for the Rb^+ - C terms of ——— $Rb^+(15C5)_2Rb^-$, ----- $Rb^+(15C5)_2e^-$, and ·—·—· $Rb^+(15C5)_2Na^-$.

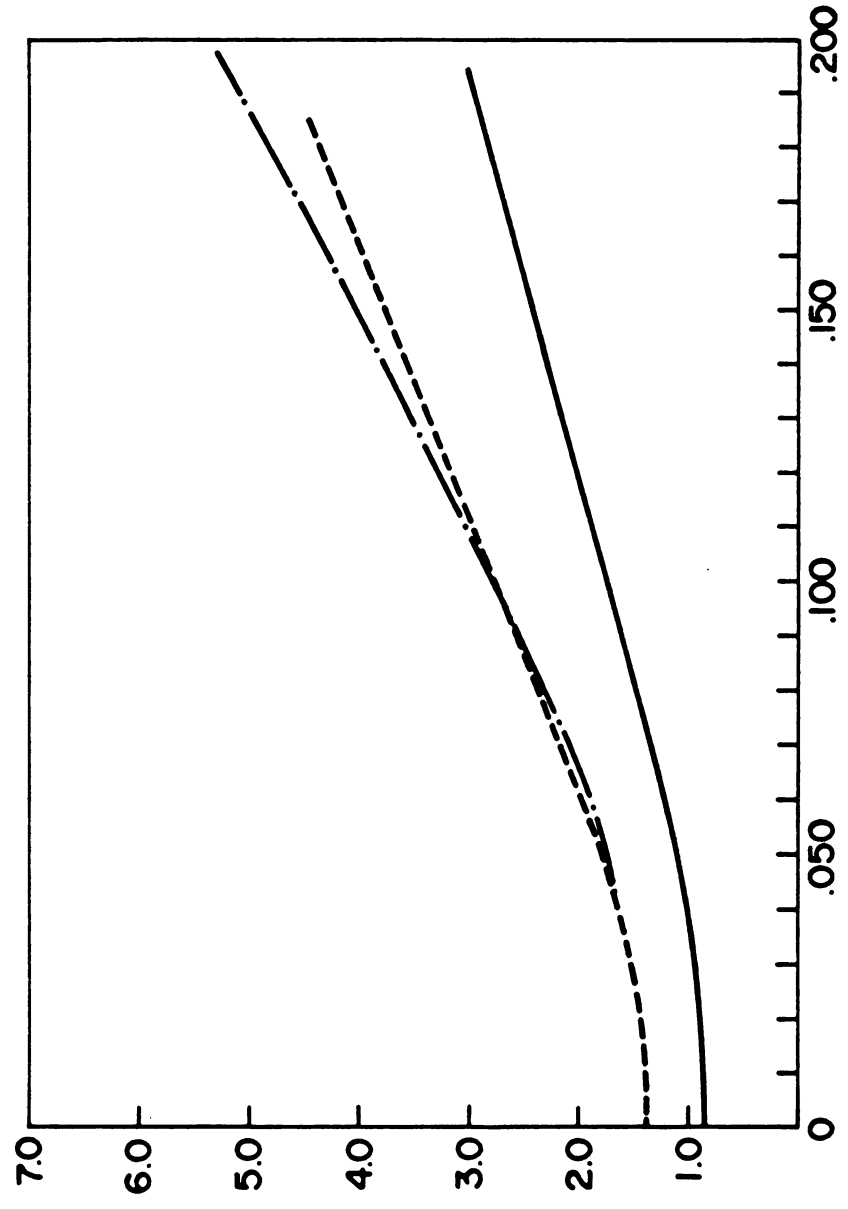

Figure 34. Parameter correlation curves B vs. σ for the Rb^+ - C terms of —— $Rb^+(15C5)_2Rb^-$, - - - - $Rb^+(15C5)_2e^-$, and '—·—·' $Rb^+(15C5)_2Na^-$.

Table 4 . Fine Adjustment (Based on Model Compounds) to Best Fit Based on Theory Results for Interatomic Distances r(Å) and Coordination Numbers (N)

Compound	Term	r[a]	N
$Rb^+(15C5)_2 \cdot Na^-$	Rb-O	3.009[b]	10.00[b]
	Rb-C	3.818[b]	20.00[b]
$Rb^+(15C5)_2 \cdot e^-$	Rb-O	2.973	10.46
	Rb-C	3.816	19.38
$Rb^+(15C5)_2 \cdot Rb^-$	Rb-O	2.954	12.50
	Rb-C	3.801	24.74
$Rb^+(18C6) \cdot SCN^-$	Rb-O	3.024[c]	6.00[c]
	Rb-C	3.803[c]	12.00[c]
$Rb^+(18C6)Br^- \cdot 2H_2O$	Rb-O	3.013	4.75
	Rb-C	3.805	10.97
$Rb^+(18C6) \cdot Na^-$	Rb-O	2.945	5.66
	Rb-C	3.730	12.74
Rb(18C6)	Rb-O	2.987	7.36
	Rb-C	3.770	17.37
$Rb^+(18C6) \cdot Rb^-$	Rb-O	2.916	7.36
	Rb-C	3.745	16.80

[a]Standard deviations 0.05 - 0.11 Å

[b]Single-Crystal X-ray Diffraction Results.[13]

[c]Single-Crystal X-ray Diffraction Results.[19]

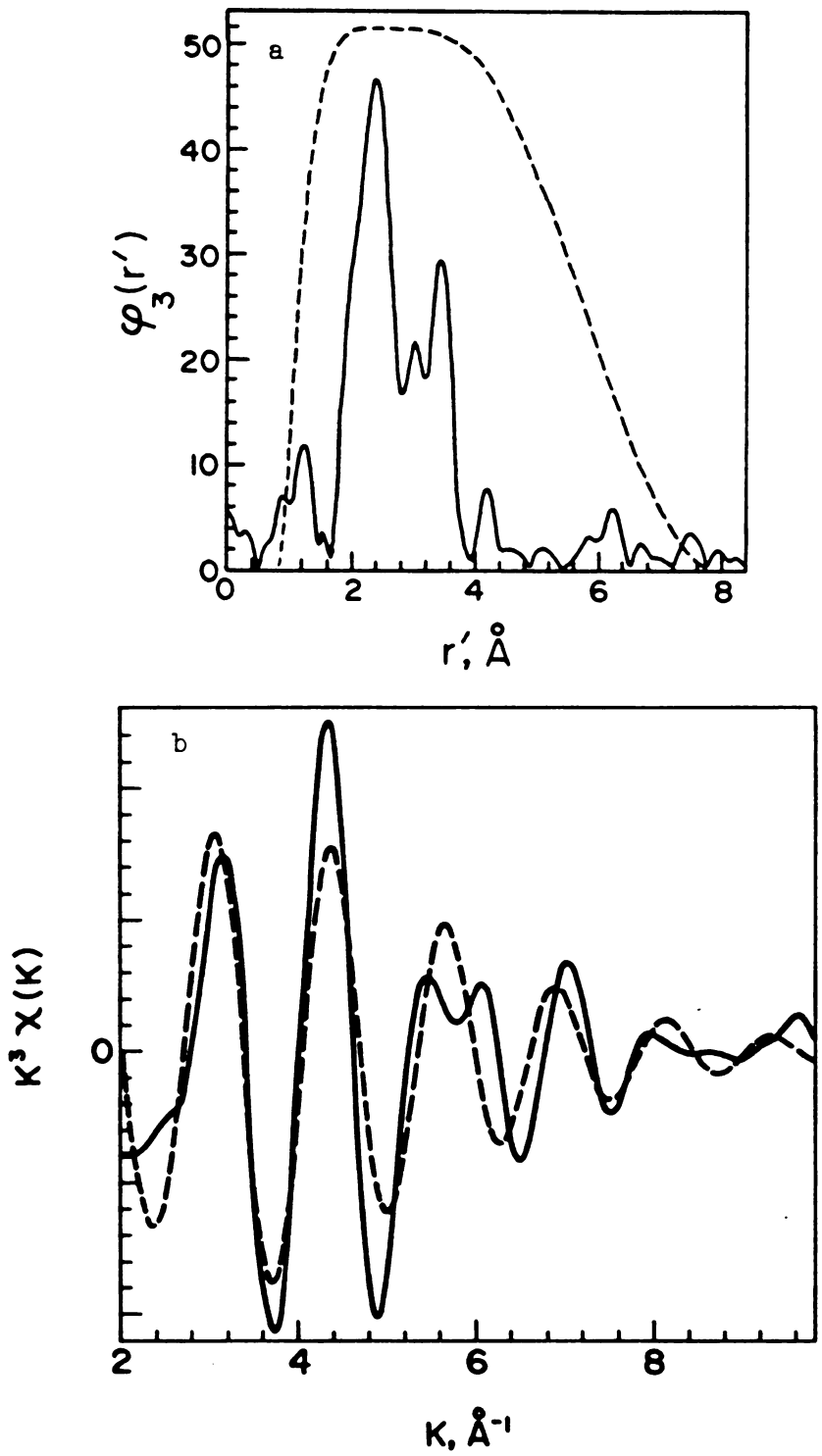

Figure 26. (a) Fourier transform (solid curve) of the Rb K-edge EXAFS, $k^3\chi(k)$ vs. k, and filtering window (dashed curve) for $Rb^+(18C6)SCN^-$; (b) Fourier filtered EXAFS spectrum (solid curve) and best fit based upon theory (dashed curve).

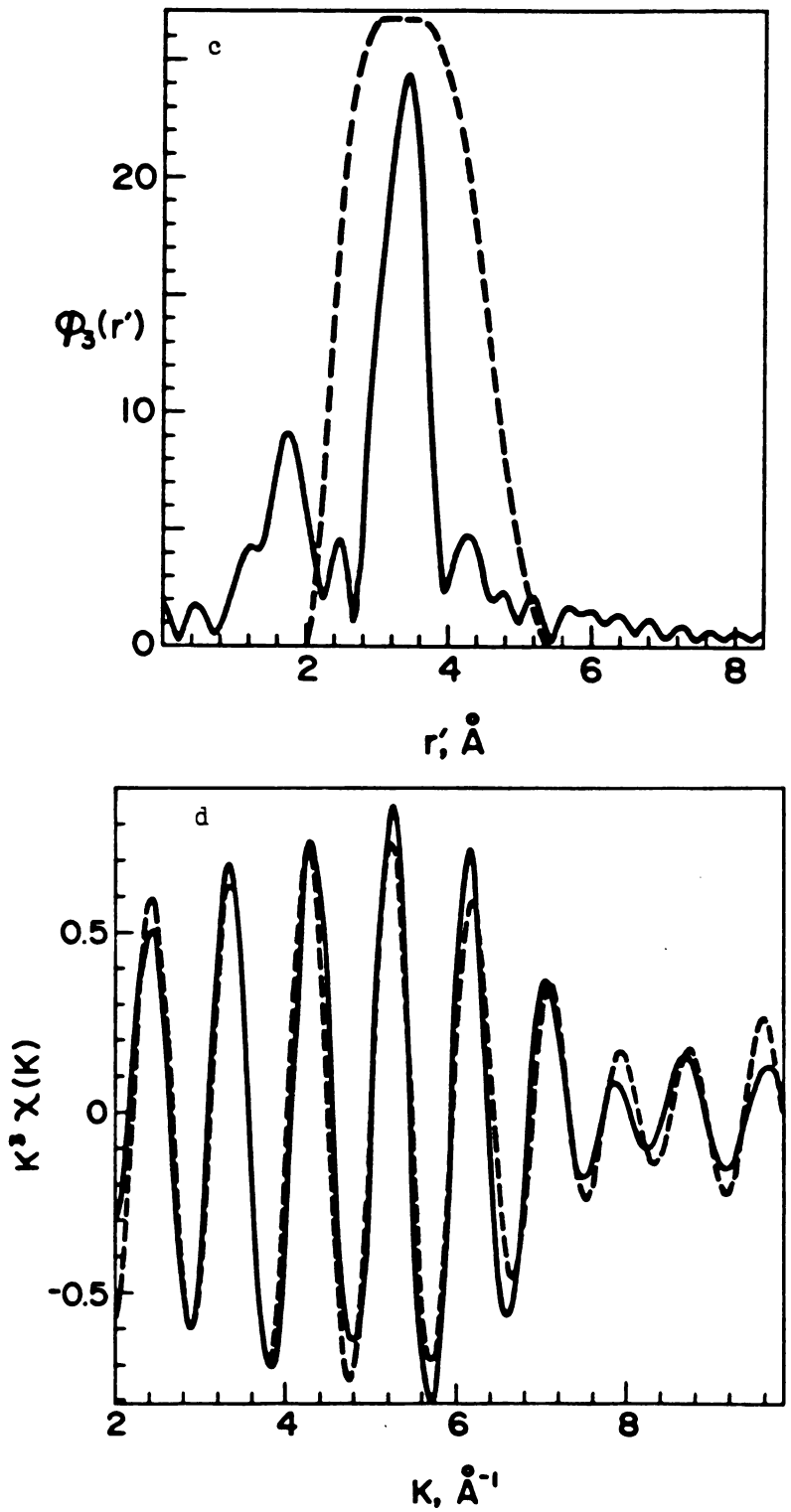

Figure 26. (c) Fourier transform (solid curve) of the difference EXAFS spectrum, $k^3\chi(k)$ vs. k. and filtering window (dashed curve) for $Rb^+(18C6)SCN^-$; (d) Fourier filtered difference EXAFS spectrum (solid) and best fit based upon theory.

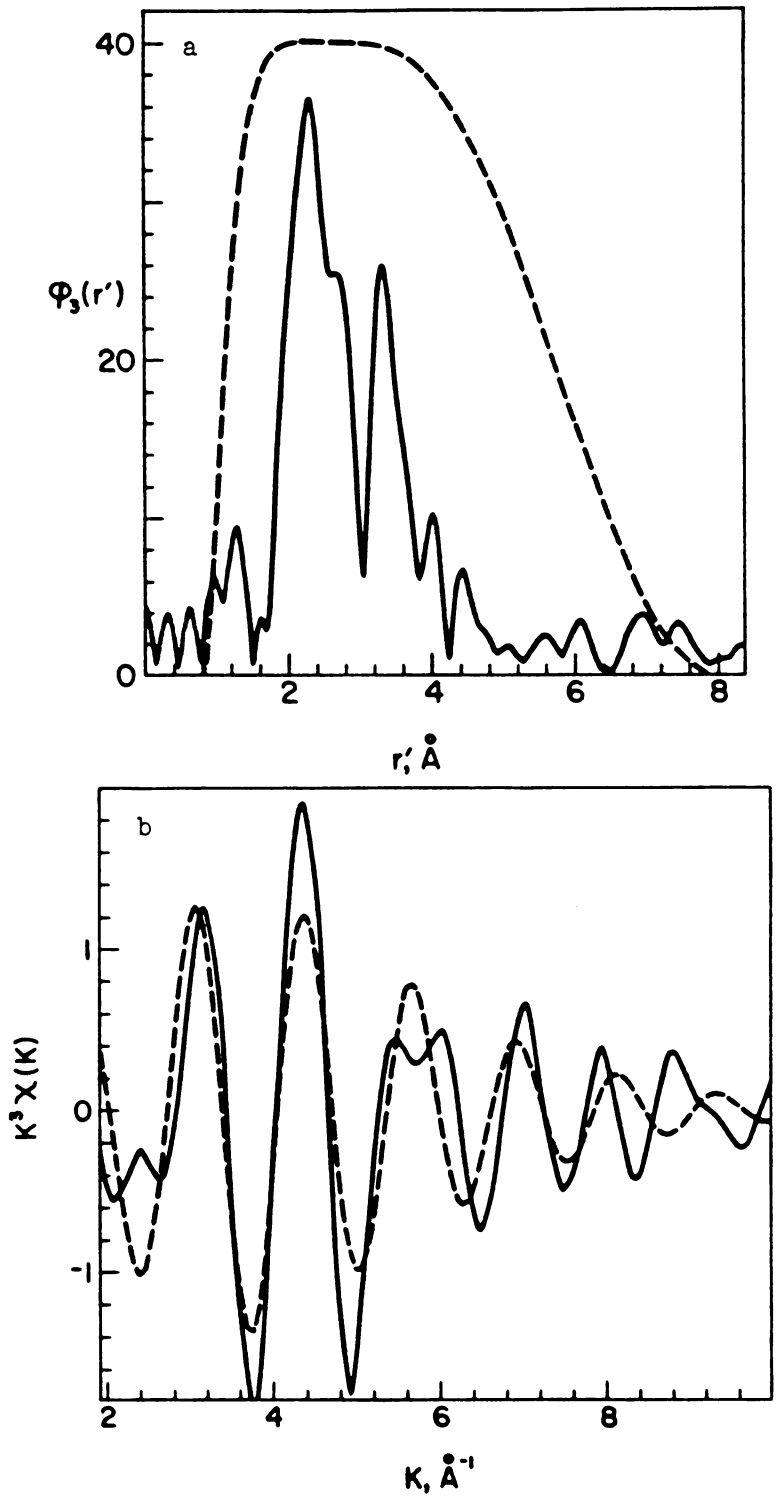

Figure 27. (a) Fourier transform (solid curve) of the Rb K-edge EXAFS, $k^3\chi(k)$ vs. k, and filtering window (dashed curve) for $Rb^+(18C6)Br^-\cdot 2H_2O$; (b) Fourier filtered EXAFS spectrum (solid curve) and best fit based upon theory (dashed curve).

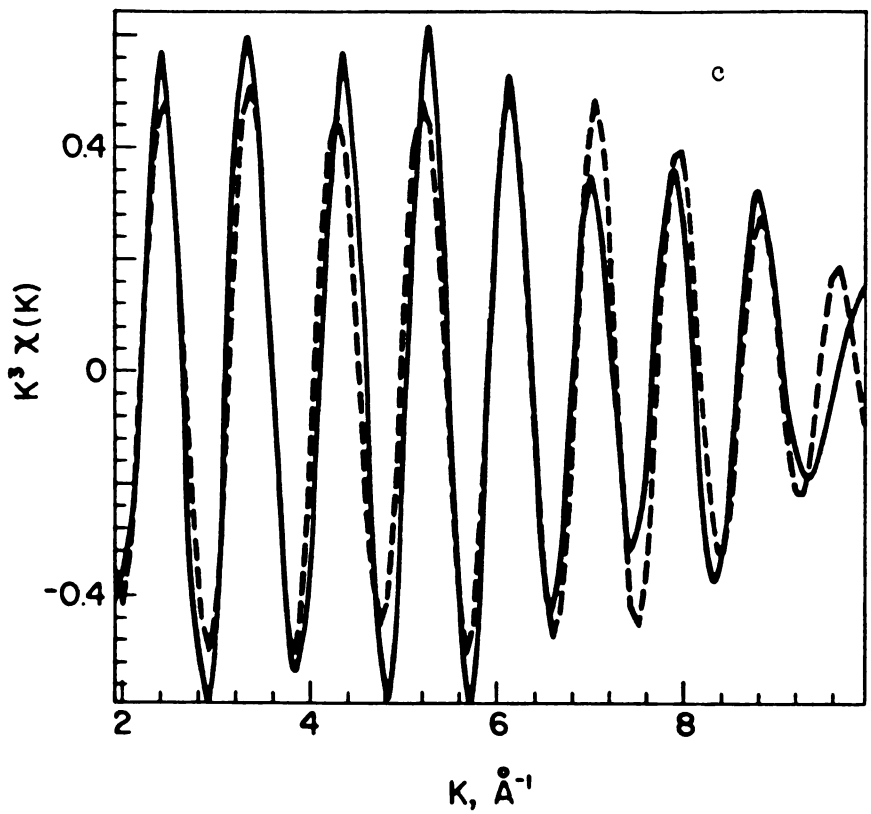

Figure 27. (c) Fourier filtered difference EXAFS spectrum (solid curve) and best fit based upon theory (dashed curve) for $Rb^+(18C6)Br^-\cdot 2H_2O$.

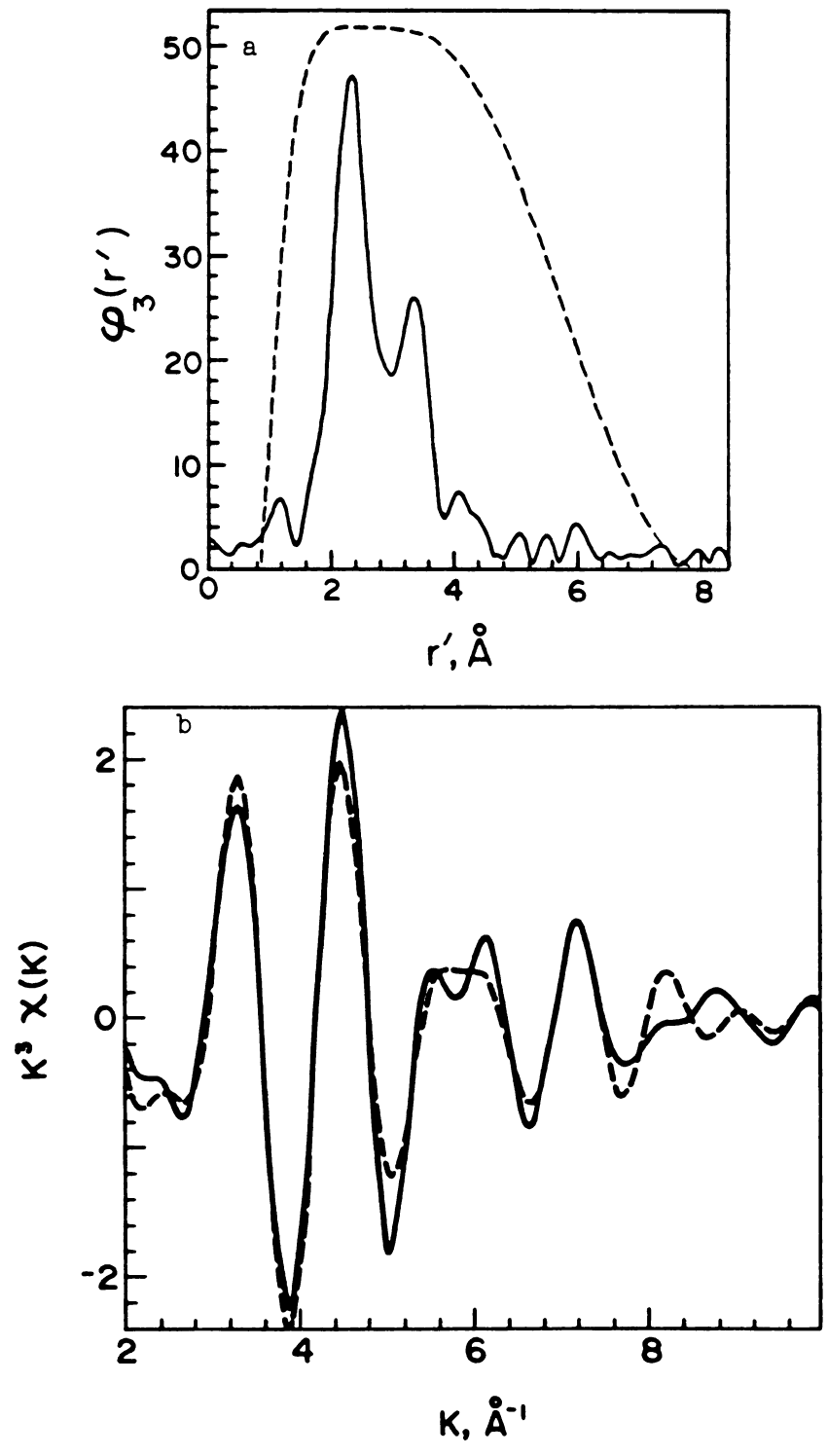

Figure 28. (a) Fourier tranform (solid curve) of the Rb K-edge EXAFS, $k^3\chi$ (k) vs. k, and filtering window (dashed curve) for $Rb^+(18C6)Na^-$; (b) Fourier filtered EXAFS spectrum (solid curve) and best fit based upon theory (dashed curve).

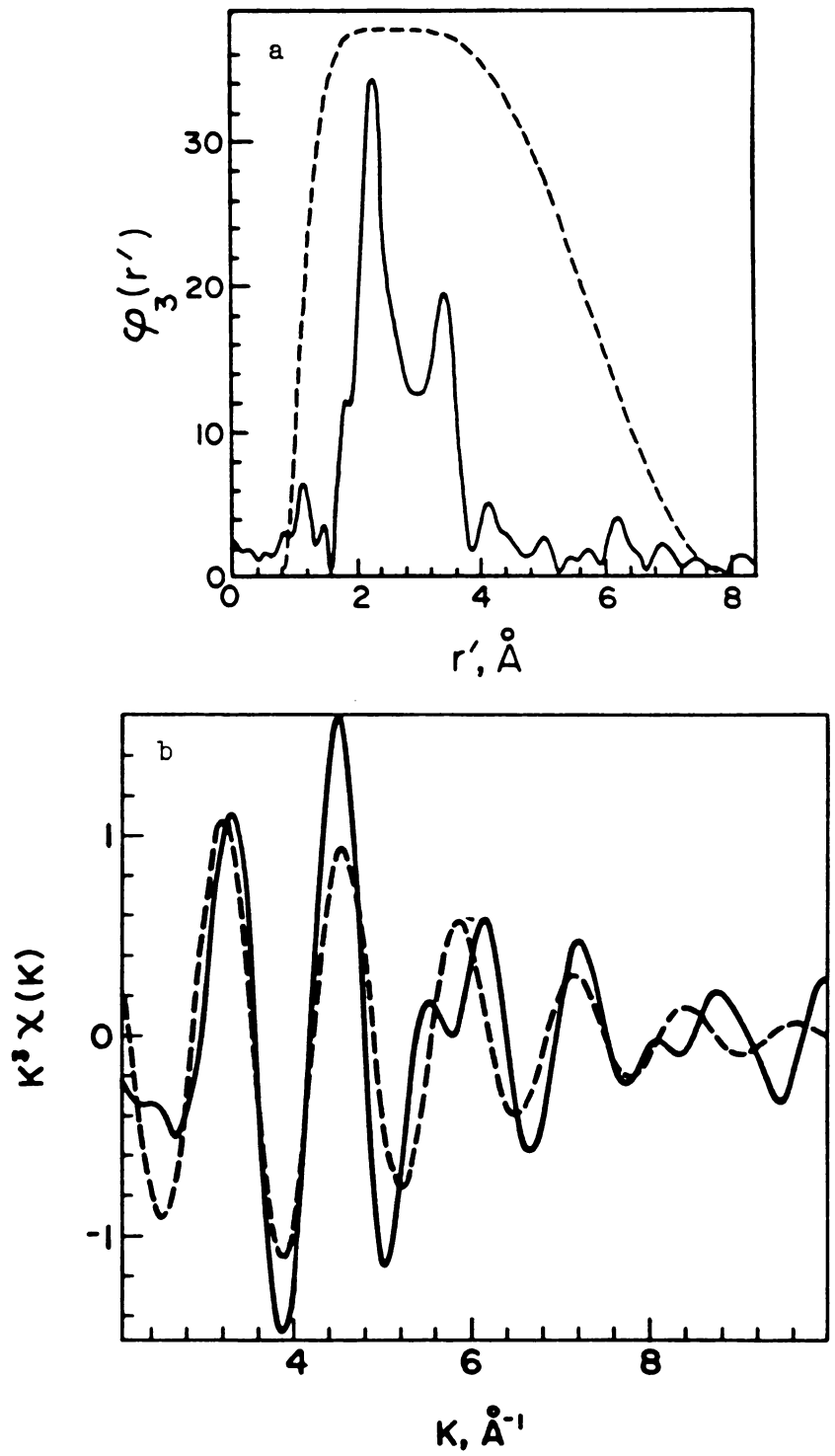

Figure 29. (a) Fourier transform (solid curve) of the Rb K-edge EXAFS, $k^3\chi$ (k) vs. k, and filtering window (dashed curve) for $Rb^+(18C6)Rb^-$; (b) Fourier filtered EXAFS spectrum (solid curve) and best fit based upon theory (dashed curve).

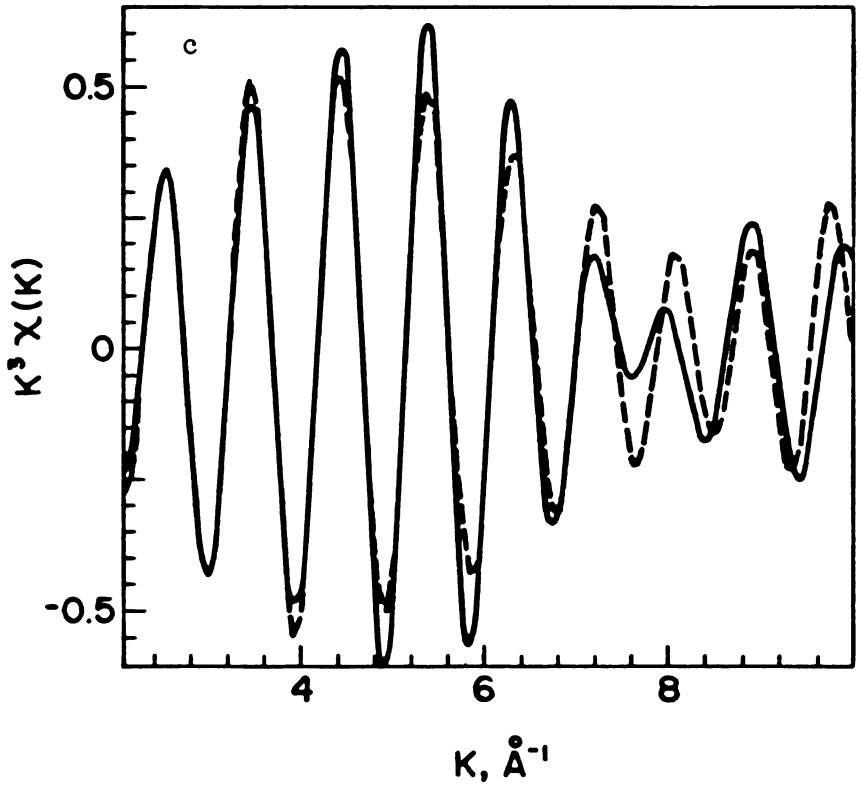

Figure 29. (c) Fourier filtered difference EXAFS spectrum (solid curve) and best fit based upon theory (dashed curve) for $Rb^+(18C6)Rb^-$.

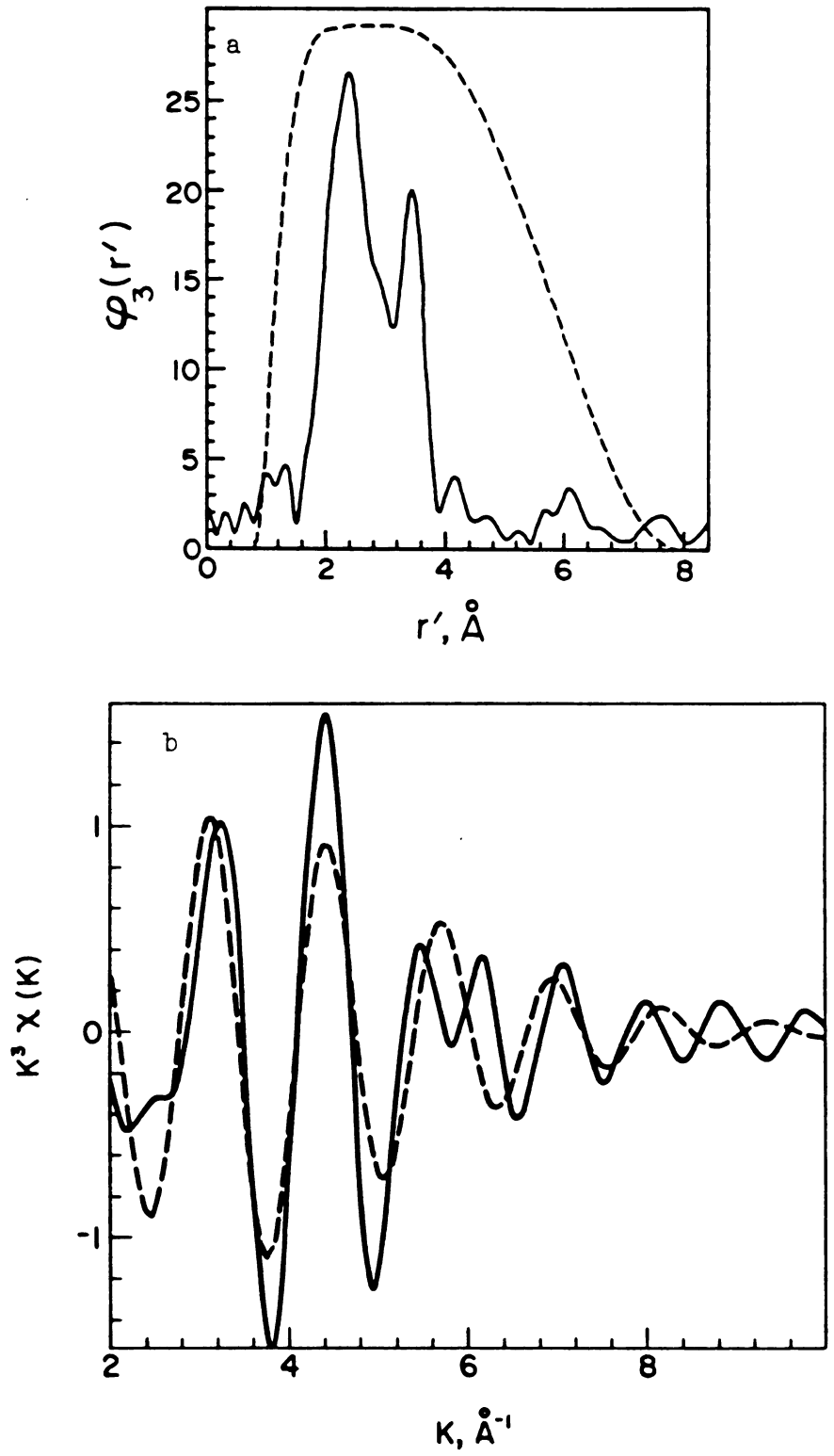

Figure 30. (a) Fourier transform (solid curve) of the Rb K-edge EXAFS, $k^3\chi(k)$ vs. k, and filtering window (dashed curve) for Rb(18C6); (b) Fourier filtered EXAFS spectrum (solid curve) and best fit based upon theory (dashed curve).

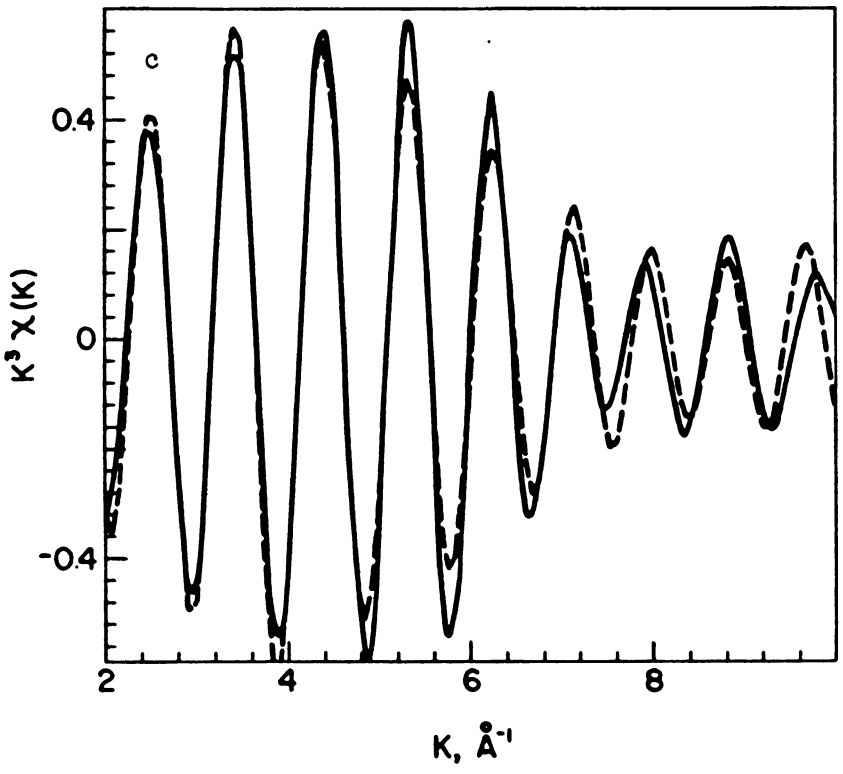

Figure 30. (c) Fourier filtered difference EXAFS spectrum (solid curve) and best fit based upon theory (dashed curve) for Rb(1806).

of the complexing agent can be detected by EXAFS. In this case, the spectrum was Fourier-filtered, resolved into two components, $k^3\chi_O$ and $k^3\chi_C$, and fit with Equation 19 for j=O,C, as was done previously for the $Rb^+(15C5)_2 \cdot X^-$ series. The FT's of $Rb^+(18C6) \cdot Br^- \cdot 2H_2O$, $Rb^+(18C6) \cdot Rb^-$ and Rb(18C6), are similar to that of the thiocyanate salt, in that three distinct shells of neighbors are observed. The characteristic peaks at 2.5 Å and 3.5 Å, which represent the Rb-O and Rb-C interactions, respectively, are present. For the bromide (Figure 27), a peak at 2.7 Å corresponds to coordination to the oxygens of the water molecules of the dihydrate. In the case of $Rb^+(18C6) \cdot Rb^-$ and Rb(18C6) (Figures 29 and 30, respectively) a smaller peak at 3.0 Å is evident in the FT. This peak cannot be attributed to bonding to the large Rb^- anion, since the observed distances are much shorter than would be expected. Instead, it is believed to arise from a lengthening of some of the Rb-O distances due to a distortion of the 18-crown-6 ring. It is known that the 18-crown-6 molecule is flexible and can adopt different conformations compatible with the coordination requirements of the specific complex. Such a distortion would create two nonequivalent rubidium-oxygen interactions. Also note that these Fourier transforms do not allow the definitive identification of the Rb(18C6) salt as an electride and, instead, suggest that some rubidide may be present. After Fourier filtering, a difference Fourier technique [79, 84] was used to resolve the data for these

compounds into two components, $k^3\chi_O$ and $k^3\chi_{A/C}$, which could then be curve-fit with a three term (j=O, A, C) backscattering formulation. Here A represents the shell of neighbors located between the oxygen and carbon shells, that is, A=SCN^- and Br^- for $Rb^+(18C6)\cdot SCN^-$ and $Rb^+(18C6)\cdot Br^-\cdot 2H_2O$ respectively, and A=O for $Rb^+(18C6)\cdot Rb^-$ and Rb(18C6).

The resulting values for the best fit parameters are listed in Table 3. The ΔE_o vs. r correlation curves are shown in Figures 35 and 37. The B vs. σ correlation plots are illustrated in Figures 36 and 38. The FABM results are given in Table 4. Note that for the $Rb^+(18C6)\cdot X^-$ compounds there is a slight shortening in the Rb-O bond as the anion is changed just as was observed for the $Rb^+(15C5)_2\cdot X^-$ series, with the rubidide having the shortest Rb-O distances for this case as well. For Rb(18C6) and $Rb^+(18C6)\cdot Rb^-$ the values obtained from the fit with two Rb-O terms suggest that the first Rb-O shell of neighbors appears at approximately the same distance as in the models. The second shell appears at 3.60 A for $Rb^+(18C6)\cdot Rb^-$ and at 3.64 A for Rb(18C6). It was not possible to further refine these values with the FABM method because there are no known reference compounds that exhibit this type of coordination, although it can be pointed out that these distances are similar to the Rb^+-to-anion distances in $Rb^+(18C6)\cdot SCN^-$ and $Rb^+(18C6)\cdot Br^-\cdot 2H_2O$. It should also be noted that in $Rb^+(18C6)\cdot Rb^-$ and Rb(18C6) a reduction in the magnitude of the FT is present. This is expected for $Rb^+(18C6)\cdot Rb^-$ since

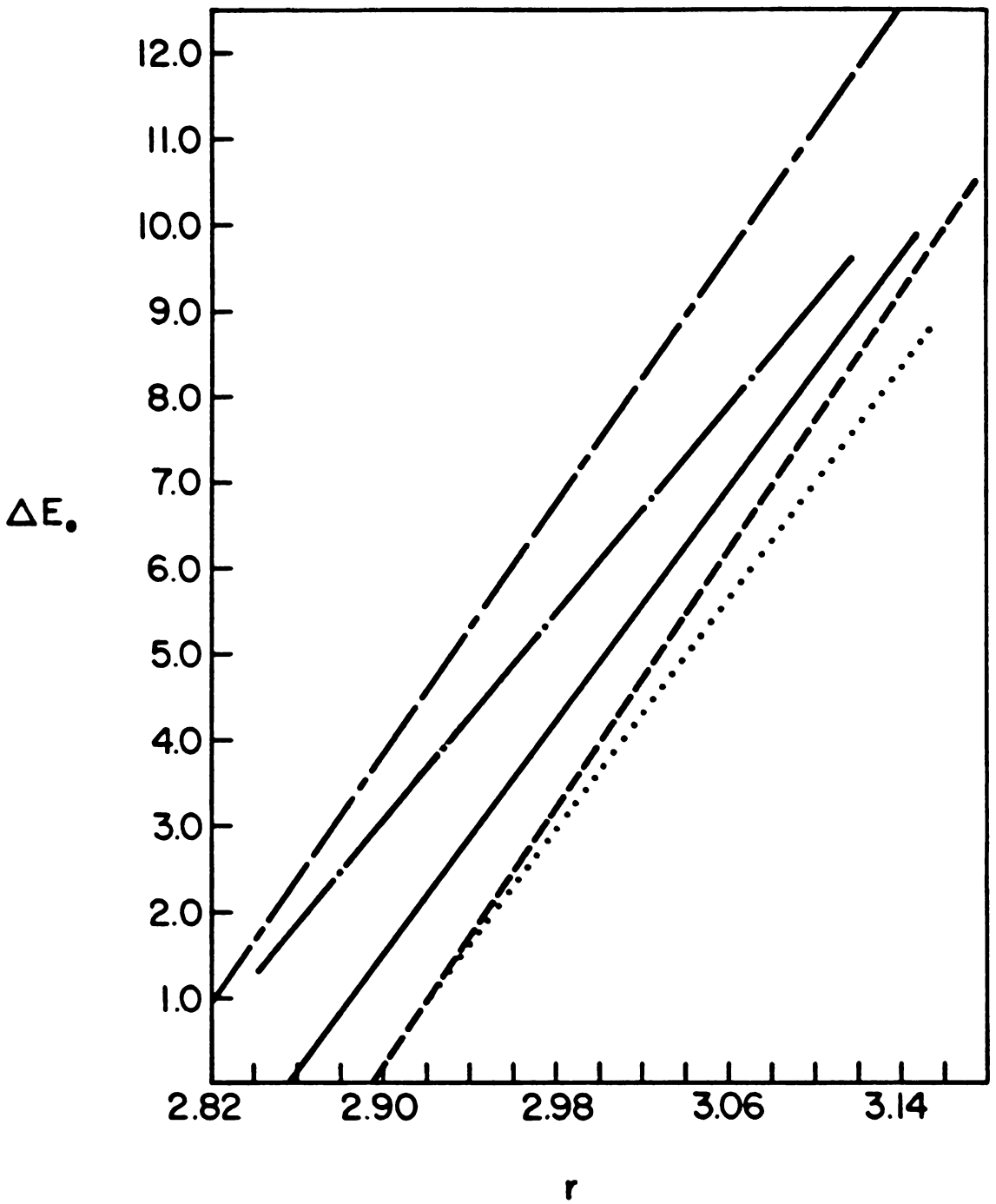

Figure 35. Parameter correlation curves ΔE_o vs. r for the Rb^+ - O terms of — – — – $Rb^+(18C6)Rb^-$, —·—·— $Rb^+(18C6)Na^-$, ——— Rb(18C6), - - - - - $Rb^+(18C6)Br^- \cdot 2H_2O$, and ..... $Rb^+(18C6)SCN^-$.

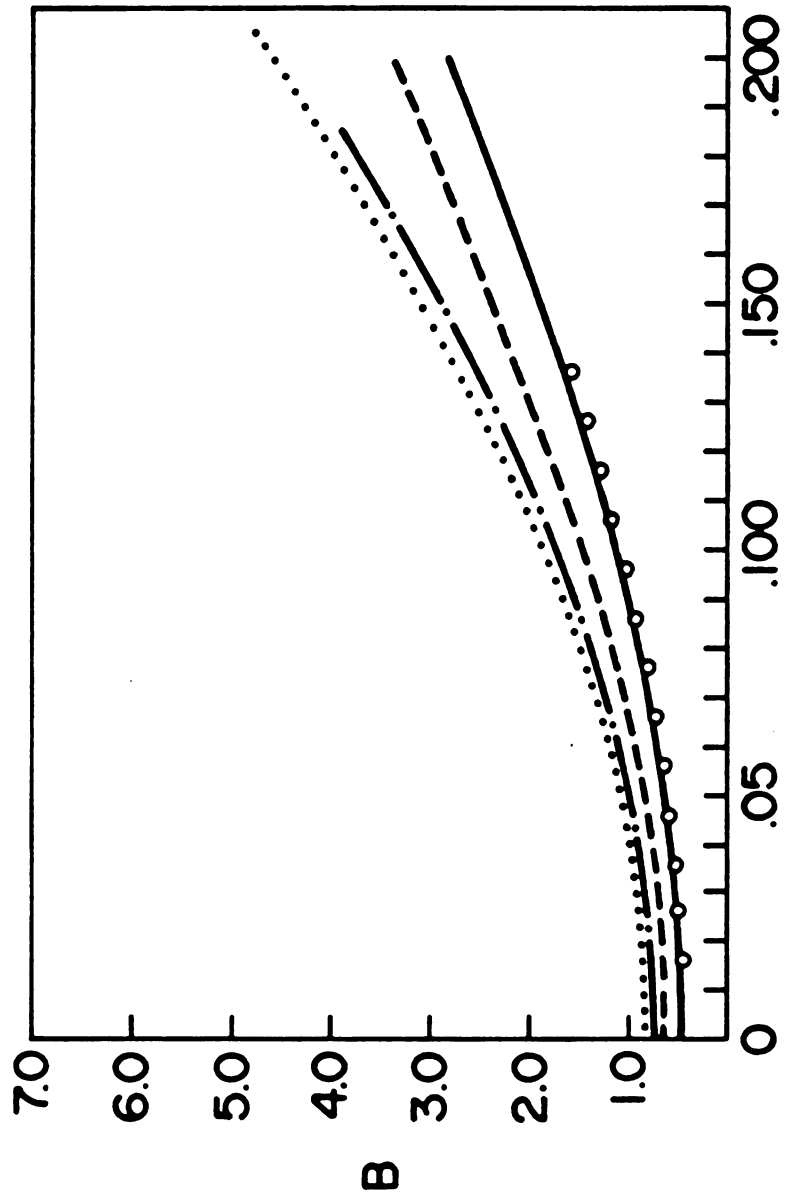

Figure 36. Parameter correlation curves B vs. σ for the Rb^+ - O terms of o o o o $Rb^+(18C6)Rb^-$, _·_·_ $Rb^+(18C6)Na^-$, —— Rb(18C6), ----- $Rb^+(18C6)Br^-\cdot 2H_2O$, and ..... $Rb^+(18C6)SCN^-$.

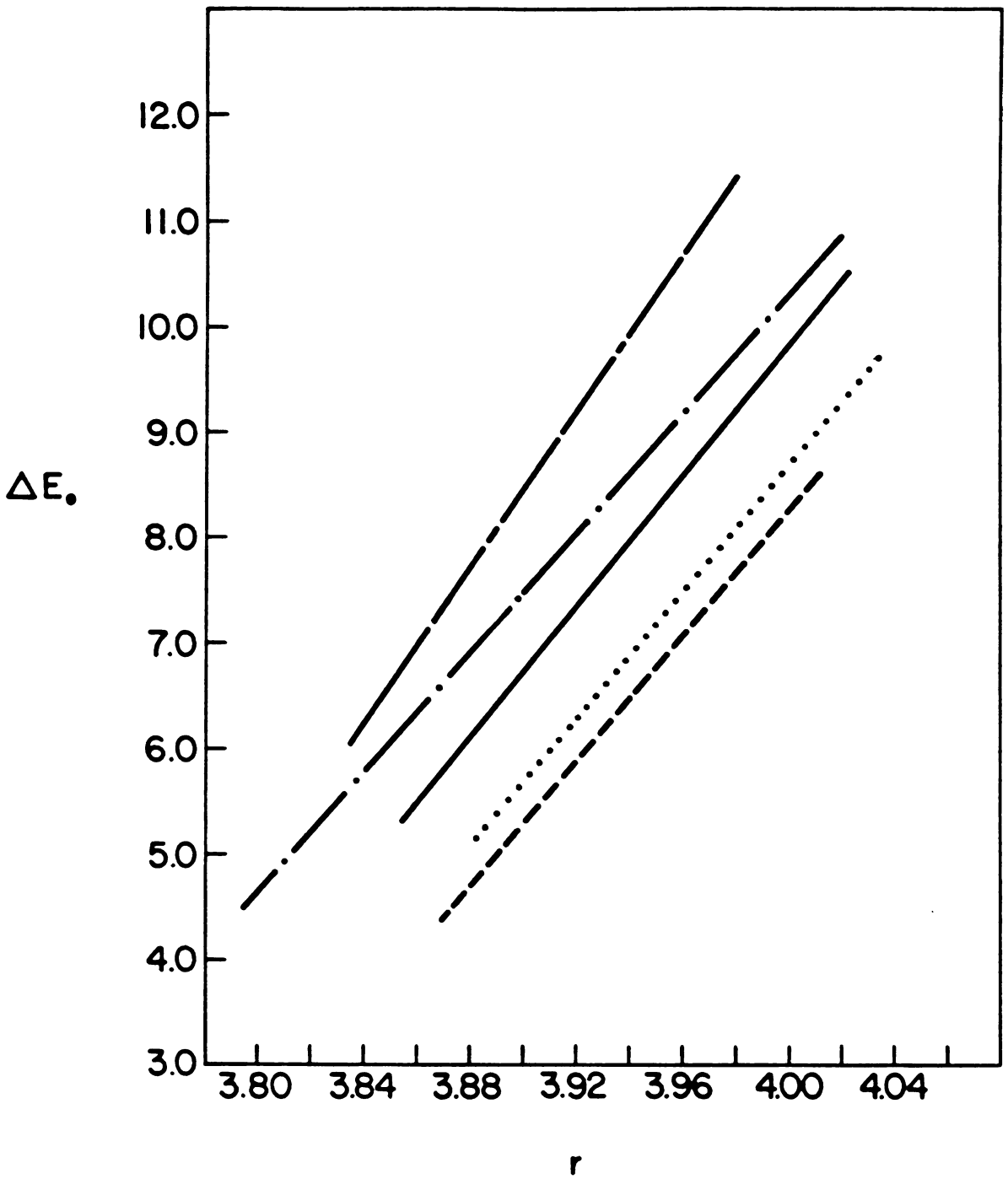

Figure 37. Parameter correlation curves ΔE_o vs. r for the Rb^+ - C terms of — – — $Rb^+(18C6)Rb^-$, —·—·— $Rb^+(18C6)\ Na^-$, —— $Rb(18C6)$, - - - - $Rb^+(18C6)Br^-.2H_2O$ and ..... $Rb^+(18C6)SCN^-$.

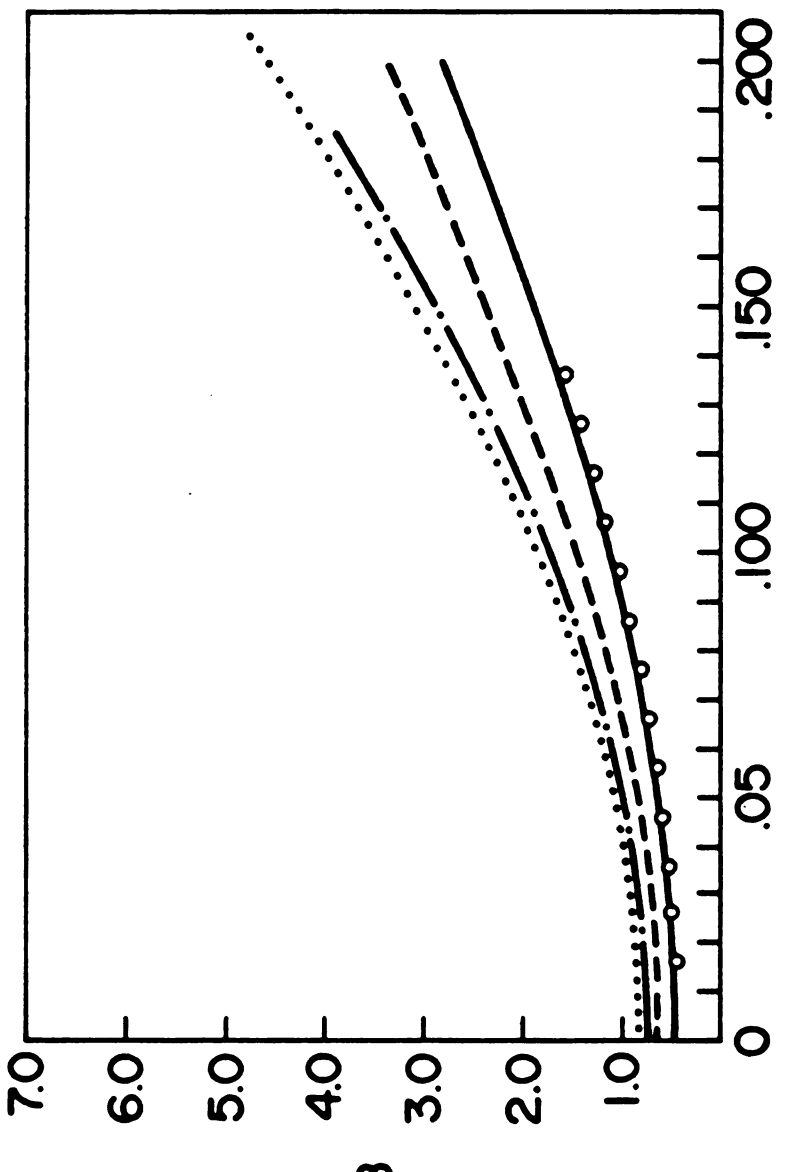

Figure 38. Parameter correlation curves B vs. σ for the Rb^+ - C terms of o o o $Rb^+(18C6)Rb^-$, —·—·— $Rb^+(18C6)Na^-$, ——— $Rb(18C6)$, - - - - $Rb^+(18C6)Br^-\cdot 2H_2O$, and ····· $Rb^+(18C6)SCN^-$.

only half of the rubidium is present as the cation and Rb^- has no significant contribution to the EXAFS spectrum. The reduction in the EXAFS amplitude of Rb(18C6) suggests that this too may be a rubidide, perhaps the sandwich compound $Rb^+(18C6)_2 \cdot Rb^-$. However, as was mentioned earlier, other evidence (NMR and optical spectra) does not support this assignment and no other sandwich complexes of Rb^+ with 18C6 are known.

It is of interest to note here that Rb(18C6) can be prepared by two possible methods [59]. In the first method, equimolar amounts of rubidium and 18-crown-6 are dissolved in dimethyl ether, followed by crystallization in trimethylamine. Alternatively, the starting materials, along with a stoichiometric amount of lithium, are dissolved in methylamine, and crystallized in a mixture of isopropyl amine and diethyl ether. The crystals prepared by the first method appear bronze-colored and have either cubic or hexagonal external morphology. The crystals prepared from the solutions that contain lithium, are thin needles, golden in color. Crystals obtained by each method were analyzed by X-ray absorption. A comparison of the background-removed EXAFS data of $Rb^+(18C6)Rb^-$ with that of Rb(18C6) prepared with lithium showed identical phase and amplitude in the spectra of both compounds. By comparison, the spectrum of a sample prepared by crystallization from trimethylamine showed slight differences in the phase and in the detailed spectral features. It is possible that Rb(18C6) is a doped

rubidide. If such were the case, according to the experimental observations, the preparation of Rb(18C6) with added lithium seems to yield a doped rubidide with a smaller content of trapped electrons as compared to the product of crystallization in trimethylamine. A final assignment on the nature of the compound Rb(18C6) is not possible at this time. Many attempts to prepare high-quality single crystals of Rb(18C6) by both methods failed, often yielding mixtures of the product with free 18-crown-6 or free metal.

The FT of $Cs^{+}(18C6)_{2}\cdot Rb^{-}$ yields no discernible peaks above the background. This confirms the view obtained from the XANES studies, which indicated that Rb^{-} is a large, spherical anion with no neighboring species within bonding distance. For the systems that contain mixtures of complexed rubidium cations and rubidide anions a proportionate reduction in the amplitude of the $k^{3}\chi(k)$ vs. k data is evident and this feature could be used in addition to the XANES spectrum to indicate the presence of the rubidium anion in a compound.

4.3.4 EXAFS Amplitudes

In all the radial distribution functions shown, the overall magnitudes of the peaks for these complexes are smaller than usually obtained from EXAFS spectroscopy. This is consistent with the nature of the complexation of alkali metals by cryptands and crown ethers. The magnitude of the radial structure function is accounted for in part by the

factor $\exp[-2\sigma_j^2 k^2]$ in the amplitude component of the EXAFS equation (Equation 14). This Debye-Waller factor has two components σ_{stat} and σ_{vib} due to static disorder and thermal vibrations respectively [53]. It can be described by

$$\sigma = \sqrt{\sigma_{stat}^2 + \sigma_{vib}^2} \qquad (23)$$

For the type of coordination in these alkali metal complexes both contributions are rather large. The cation is complexed loosely by the ligating oxygens, the bonds are relatively weak and there is appreciable vibrational motion even at the low temperatures employed for data collection. Some room temperature EXAFS scans of the model compounds were very noisy and their quality proved unacceptable for data analysis. The static contribution to the Debye-Waller factor is also relatively large. The crystallographic data show that the distances between the rubidium cation and the oxygen atoms are not all equal (see Chapter 5). In addition, in some cases, more than one stable conformation for the crown ether is allowed and this causes disorder in the complexation. This type of disorder has been observed in the structures of $Rb^+(15C5)_2 \cdot Na^-$ and $Cs^+(15C5)_2 \cdot I^-$ [85]. The static contribution to the Debye-Waller factor can be estimated by:

$$\sigma_{stat} \approx \sqrt{\frac{\sum_{j=1}^{N} (r_j - r_o)^2}{N}} \qquad (24)$$

for N neighbors of the same type, for which $r_j - r_o$ is the

deviation from the mean distance r_o. By using this expression with the crystallographic data for the six Rb-O distances in $Rb^+(18C6)SCN^-$ [73], the Rb-O contribution to σ_{stat} was found to be 0.083 A.

The value of σ_{vib} cannot be independently calculated because the necessary vibrational data are not available. By using the experimental Debye-Waller factor, it can be estimated to be 0.043 A. Similar calculations for $Rb^+(18C6)\cdot Br^-\cdot 2H_2O$ give 0.091 A and 0.041 A for σ_{stat} and σ_{vib} respectively.

The reduced EXAFS amplitudes obtained for these complexes are also due to the relatively large distances between the rubidium cation and the nearest shell of oxygen neighbors from the ligand (3.00 A). This causes a reduction in the amplitude because of the r^{-2} dependence of the EXAFS function (Equation 14).

4.4 Conclusions

The combined use of XANES and EXAFS has permitted the identification and structural characterization of rubidium-containing alkalides and electrides. The white line areas provide a means of identifying these new products as pure rubidides, electrides, or mixtures. The XANES studies have been especially valuable in identifying the rubidium-containing species in heteronuclear alkalides such as $Rb^+(18C6)\cdot Na^-$, $Cs^+(18C6)_2\cdot Rb^-$ and $K^+C222\cdot Rb^-$. In other cases, they have shown the presence of mixtures of alkalides

such as in $RbK(15C5)_2$ and RbK(18C6). They have also been valuable in the study of those compounds that contain only rubidium and the complexant. For example, they have allowed the characterization of $Rb^+(15C5)_2e^-$ as a pure electride and of $Rb^+(15C5)_2 \cdot Rb^-$ as a rubidide with complexed rubidium as the cation. These assignments would not have been possible with optical spectroscopy or ^{87}Rb magic angle sample spinning NMR studies. For the compound Rb(18C6), however, a final determination was not possible and the results suggest that this stoichiometry might correspond to a mixture of the sandwich rubidide and the non-sandwich electride.

The salts $Rb^+(18C6) \cdot X^-$ are especially difficult to crystallize and for these, the results of this study provide the only available structural information at present. These data suggest that the conformation of 18-crown-6 in $Rb^+(18C6) \cdot Rb^-$ and Rb(18C6) is different from that in the models $Rb^+(18C6) \cdot SCN^-$ and $Rb^+(18C6) \cdot Br^- \cdot 2H_2O$. The structures of the $Rb^+(15C5)_2 \cdot X^-$ complexes are similar to the model $Rb^+(15C5)_2 \cdot Na^-$, exhibiting a rubidium cation sandwiched between two 15-crown-5 rings. The rubidide anion, Rb^-, has been shown to be a large spherical anion with no nearest neighbors at detectable distances.

CHAPTER FIVE

CRYSTAL STRUCTURES OF $Rb^+(15C5)_2Na^-$ AND $Rb^+(18C6)Br^- \ 2H_2O$

5.1 Crystal Structure of $Rb^+(15C5)_2Na^-$

As mentioned in Chapter 1, the structure of the first alkalide salt, $Na^+C222Na^-$, was obtained by single crystal X-ray diffraction methods shortly after the preparation of the compound [2]. This was possible because of the relatively high stability exhibited by this compound. However, following this structural determination, all attempts to obtain the structures of other alkalides failed due to the difficulties involved in producing crystals of high enough quality and to the instability and sensitivity of the compounds. In 1985, the structures of two sodides, $Cs^+(18C6)_2Na^-$ [85] and $Rb^+(15C5)_2Na^-$, were obtained. Later in that year, the first structure of an electride, $Cs^+(18C6)_2e^-$, was solved [85]. These successful structural determinations were the direct result of new and improved methods of preparing single crystals of alkalides and electrides, and of the implementation of new anaerobic techniques in the handling and mounting of the sensitive crystals. In the following sections, the elucidation of

the structure of $Rb^+(15C5)_2Na^-$ by single crystal X-ray diffraction methods will be presented.

5.1.1 Crystal Selection and Mounting: $Rb^+(15C5)_2Na^-$

The crystals for study by single crystal X-ray diffraction were inspected and mounted while inside a glove bag under an inert, dry nitrogen atmosphere. The glove bag had been purged for at least eight hours prior to the loading of the crystals and contained a microscope equipped with a cold stage. The cold stage is made of copper and contains underneath its surface a series of cylidrical channels through which chilled nitrogen gas flows, cooling, by thermal conduction, the top surface of the cold stage. The nitrogen gas is chilled by flowing it through a series of copper coils immersed in liquid nitrogen. A copper/Constantan thermocouple placed next to the sample area allowed the measurement of the temperature of the sample on the cold stage. This temperature could be carefully controlled by changing the pressure of the cold nitrogen gas flow or by mixing the cold gas with warm dry nitrogen gas, as necessary.

The crystals of $Rb^+(15C5)_2Na^-$ were provided by Dr. M. Tinkham [86] and were obtained directly from a synthesis as described in Chapter 2. They had been stored in a glass ampoule at approximately -100^oC. The ampoule was brought inside the glove bag and kept cold by placing it in a

container with liquid nitrogen. The crystals were not immersed in the liquid nitrogen, but were placed directly above the boil-off of the liquid. This was sufficient to maintain the crystals at a temperature comparable to that at which they had been stored. The ampoule was opened and the crystals were poured onto a microscope slide on the cold stage. The crystals were dispersed on the cold surface of the slide and covered with a few drops of octane. The octane had been previously dried by distillation over sodium metal under vacuum, followed by freeze-pumping. Octane freezes at -55^{o}C, and once the crystals are mounted, it provides an insulating coating which protects the surface of the crystals from attack by air, moisture and other reducible impurities. A reflective, bronze-colored fragment crystal of $Rb^{+}(15C5)_{2}Na^{-}$ was mounted on a glass fiber in a random orientation. To attach the crystal to the glass fiber, a small amount of Celvacene High Vacuum Grease (Medium, from CVC Products, Inc.) had been spread on the fiber. The glass fiber had been previously fixed onto a stainless steel goniometer pin. Once the crystal was mounted, the pin was loaded onto a portable nitrogen boiler to be transferred from the glove bag to the goniometer head of the diffractometer. The nitrogen boiler contains a heater immersed in liquid nitrogen. Upon heating, a stream of cold dry nitrogen gas is produced which serves the double purpose of keeping the crystal cold and bathing it in an

inert atmosphere during transfer. The flow rate of the stream of the boiler, as well as the temperature of the stream, were controlled by varying the temperature of the heater.

5.1.2 Data Collection and Reduction

The preliminary examination for crystal quality, lattice parameters, crystallographic system and probable space group, as well as the data collection, were performed by using Mo K_α radiation (λ= 0.71073 Å) on a Nicolet P3F computer controlled 4-circle diffractometer equipped with a graphite crystal incident beam monochromator.

The unit cell parameters and an orientation matrix for the data collection were obtained from least-squares refinement, by using the setting angles of 17 reflections in the range $15 < 2\theta < 20^{\circ}$. The unit cell was found to be monoclinic with the parameters a = 11.555(3) Å, b = 13.587(3) Å, c = 9.958(3) Å, $\beta = 92.03(2)^{\circ}$, and calculated volume, V = 1562.4(7) $Å^3$. For Z = 2 and formula weight 549.00 g/m, the calculated density is 1.17 g/cm^3. As a check on crystal quality, omega scans of several intense reflections were measured; the width at half-height was 0.23° with a take-off angle of 6.0°, which indicated good crystal quality. The observed systematic absences of the form hkl and h+k=2n+1 corresponded to those of the c-centered lattice and the space group was

determined to be C2/m (#12 in the International Tables for X-Ray Crystallography [87]). The crystal data are summarized in Table 5.

The intensity data were collected at a temperature of 213(3) K, by using the θ-2θ scan technique. The details of the X-ray diffraction data collection are presented in Table 6.

A total of 2163 refections were collected, of which 1088 were unique and not systematically absent. Three representative reflections were measured every 45 reflections, as a check on crystal and instrumental stability. The slope of the least-squares line through a plot of intensity versus time was -11(8) counts/hour, which corresponds to a total loss in intensity of 0.9%. A linear decay correction was applied. The correction factors on F ranged from 1.001 to 1.005 with an average value of 1.003. Lorentz and polarization corrections were applied to the intensity data. No absorption correction was made, but a secondary extinction correction was applied [88].

5.1.3 Solution and Refinement of the Structure

The structure was solved by using the Patterson heavy-atom method [89, 90], which revealed the positions of the rubidium atoms. The remaining atoms were located in succeeding difference Fourier syntheses [90]. Carbon 8 on the 15-crown-5 ring was found to be disordered. The two

Table 5. Summary of Crystal Data for $Rb^{+}(15C5)_2Na^{-}$

F.W. 549.00 F(000) = 576

peak width at half-height = 0.23°

Mo Kα radiation (λ = 0.71073Å)

temperature = 213(3)°K

monoclinic space group C2/m

a = 11.555(3)Å b = 13.587(3)Å c = 9.958(3)Å

β = 92.03(2)°

V = 1562.4(7)$Å^3$

Z = 2 ρ = 1.17 g/cm^3

μ = 15.9 cm^{-1}

Table 6. Summary of X-Ray Diffraction Data Collection for $Rb^{+}(15C5)_2Na^{-}$

Instrument:	Nicolet P3F diffractometer
Monochromator:	Graphite crystal, incident beam
Take-off angle:	6.0°
Crystal-detector dist.:	19 cm
Scan type:	θ-2θ
Scan rate:	4°/min (in 2θ)
Scan width, deg:	$2.00 + (2\theta(K\alpha_2) - 2\theta(K\alpha_1))$
Maximum 2θ:	45°
No. of refl. measured:	2163 total, 1088 unique
Corrections:	Lorentz-polarization
	Linear decay (1.001 to 1.005 on I)
	Reflection averaging (R_{int} = 4.7%)
	Extinction (coef. = 4.75×10^{-7})

positions for this atom, C8A and C8B were refined with individual weights of 0.5. The hydrogen atoms were located and their positions and isotropic thermal parameters were refined except for those bonded to the disordered atoms C8A and C8B, which were constrained to ride on their bonded carbon atom.

All calculations were performed on a VAX-11/750 computer and an FPS-164 array processor by using SDP-PLUS [91]. The atomic scattering factors were taken from Cromer and Waber [92] except for that of Na^-, which was calculated by D. A. Liberman [93]. Corrections for anomalous dispersion effects were included; the values for $\Delta f'$ and $\Delta f''$ were those of Cromer [94].

The structure was refined in full-matrix least-squares based upon the minimization of $\Sigma w(|F_o| - |F_c|)^2$ with the weight defined as 1.0 for all observed reflections. Only the reflections having intensities greater than three times their standard deviations were used in the refinements. The final cycle of refinement included 120 variable parameters and converged with unweighted and weighted agreement factors of:

$$R_1 = \Sigma | F_o - F_c | / \Sigma F_o = 0.044$$

$$R_2 = \{ \Sigma w (F_o - F_c)^2 / \Sigma w F_o^2) \}^{1/2} = 0.052$$

The details of the refinement are summarized in Table 7.

Table 7. Summary of Structure Solution and Refinement Parameters for $Rb^{+}(15C5)_2Na^{-}$

Solution:	Patterson method
Hydrogen atoms:	Isotropic
Refinement:	Full-matrix least-squares
Minimization function:	$\Sigma w(\|Fo\|-\|Fc\|)^2$
Least-squares weights:	$4Fo^2/\sigma(Fo^2)^2$
Anomalous dispersion:	All non-hydrogen atoms
Reflections included:	688 with $Fo^2>3.0\sigma(Fo^2)$
Parameters refined:	120
Unweighted agreement factor:	0.044
Weighted agreement factor:	0.052
Esd of obs. of unit weight:	1.14
Convergence, largest shift:	0.19σ
High peak in final diff. map:	0.24(3) $e/Å^3$
Low peak in final diff. map:	-.14(0) $e/Å^3$
Computer hardware:	VAX 11/750, FPS 164
Computer software:	SDP/VAX (Enraf-Nonius & B. A. Frenz & Associates, Inc.)

5.1.4 Description of the Structure of $Rb^{+}(15C5)_2Na^{-}$

The final positional parameters with their estimated standard deviations and isotropic thermal displacement factors for $Rb^{+}(15C5)_2Na^{-}$ are listed in Table 8. The anisotropic general thermal displacement parameters for the non-hydrogen atoms are listed in Table 9. The unit cell, illustrated in Figure 39, can be described best as c-centered monoclinic. Both rubidium and sodium occupy special positions in the lattice, the fractional coordinates for rubidium being 1/2, 0, 1/2, and for sodium, 1/2, 1/2, 0. Each rubidium is complexed by two 15-crown-5 rings. Only the rubidium, the sodium and one half of one 15-crown-5 are unique; the remaining atoms can be generated by successive inversion and reflection symmetry operations. As mentioned above, Carbon 8 on the crown ether ring is disordered. Figure 39 shows the two positions for this carbon, each of which was refined with 0.5 occupancy. The complexed cations are oriented with their longest axis along c, showing a slant of 62.4^{o} with respect to the **ab** plane. Figure 40 shows the packing of $Rb^{+}(15C5)_2$ and Na^{-} in the unit cell. In this diagram, the positions of the ions are represented by circles and the crown ethers are not shown. Each ion is surrounded by eight counter-ions, as illustrated for rubidium by the dashed lines in the figure. The shortest Rb^{+}- Na^{-} contacts lie on a plane

Table 8. Positional Parameters and Their Estimated Standard Deviations for $Rb^{+}(15C5)_2Na^{-}$ at 213 K

Atom	x	y	z	B(Å^2)
Rb1	0.500	0.000	0.500	3.89(3)
Na1	0.500	0.500	0.000	7.7(2)
O1	0.4537(6)	0.000	0.1948(7)	6.3(2)
O4	0.5015(4)	-0.1794(4)	0.3268(5)	6.1(1)
O7	0.7204(4)	-0.1047(4)	0.4366(6)	7.5(2)
C2	0.3880(7)	-0.0891(6)	0.1675(8)	6.4(2)
C3	0.4714(8)	-0.1713(6)	0.1891(8)	6.9(2)
C5	0.6058(8)	-0.2347(6)	0.3525(9)	8.0(3)
C6	0.7115(7)	-0.1780(8)	0.335(1)	9.1(3)
C8A	0.823(1)	-0.0331(9)	0.465(1)	5.6(4)
C8B	0.811(1)	0.053(1)	0.370(2)	7.1(5)
H2a	0.365(6)	-0.078(5)	0.066(7)	5(2)*
H2b	0.333(5)	-0.081(4)	0.245(6)	3(1)*
H3a	0.544(7)	-0.148(7)	0.134(9)	9(3)*
H3b	0.437(5)	-0.223(4)	0.154(6)	2(1)*
H5a	0.606(5)	-0.281(5)	0.284(6)	4(2)*
H5b	0.585(5)	-0.259(5)	0.439(6)	4(2)*
H6a	0.708(7)	-0.153(7)	0.230(9)	9(3)*
H6b	0.774(5)	-0.209(5)	0.334(6)	3(1)*
H8Aa	0.823	-0.012	0.556	6.3*
H8Ab	0.894	-0.067	0.449	6.3*
H8Ba	0.790	0.035	0.281	7.5*
H8Bb	0.880	0.091	0.370	7.5*

Starred atoms were refined isotropically.
Anisotropically refined atoms are given in the form of the isotropic equivalent thermal parameter defined as:

$$(4/3) * [a^2*B(1,1) + b^2*B(2,2) + c^2*B(3,3) + ab(\cos \text{gamma})*B(1,2) + ac(\cos \text{beta})*B(1,3) + bc(\cos \text{alpha})*B(2,3)]$$

Table 9. General Temperature Factor Expressions - U's for $Rb^{+}(15C5)_2Na^{-}$ at 213 K (in $Å^2$)

Name	U(1,1)	U(2,2)	U(3,3)	U(1,2)	U(1,3)	U(2,3)
Rb1	0.0555(8)	0.0471(7)	0.0454(7)	0	0.0041(6)	0
Na1	0.112(5)	0.082(5)	0.099(5)	0	0.010(4)	0
O1	0.078(5)	0.079(5)	0.080(5)	0	-0.009(4)	0
O4	0.092(4)	0.067(3)	0.072(3)	0.010(3)	0.001(3)	-0.011(3)
O7	0.062(3)	0.064(3)	0.159(5)	0.009(3)	0.020(3)	0.024(4)
C2	0.089(6)	0.078(5)	0.076(5)	-0.008(5)	-0.007(4)	-0.011(5)
C3	0.123(7)	0.065(5)	0.072(5)	0.003(5)	-0.009(5)	-0.018(4)
C5	0.137(7)	0.071(5)	0.095(6)	0.037(6)	0.009(6)	-0.009(5)
C6	0.083(5)	0.135(8)	0.132(7)	0.056(5)	0.037(5)	0.033(7)
C8A	0.057(8)	0.06(1)	0.10(1)	0.017(7)	-0.006(7)	0.027(7)
C8B	0.055(9)	0.10(1)	0.11(1)	-0.001(9)	0.010(9)	-0.01(1)

The form of the anisotropic thermal parameter is:

$$\exp[-2\pi^2\{h^2a^2U(1,1) + k^2b^2U(2,2) + l^2c^2U(3,3) + 2hkabU(1,2) + 2hlacU(1,3) + 2klbcU(2,3)\}]$$

where a, b, and c are reciprocal lattice constants.

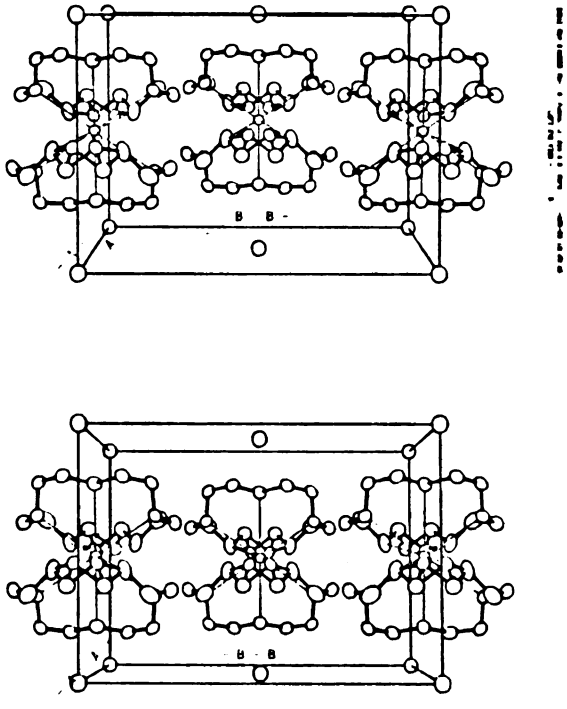

Figure 39. Stereoscopic view of the unit cell of $Rb^{+}(15C5)_2Na^{-}$.

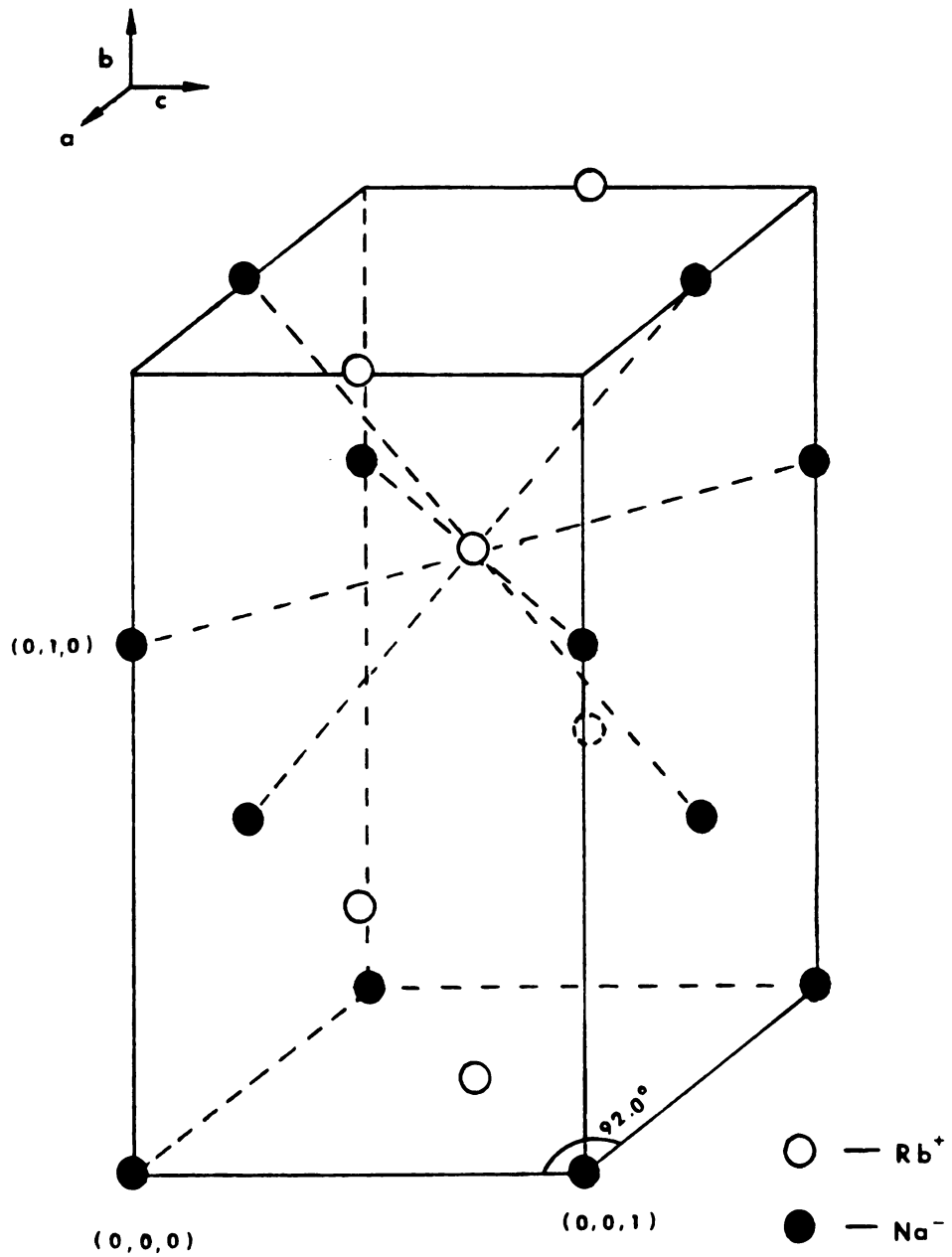

Figure 40. Packing of $Rb^{+}(15C5)_2$ (open circles) and Na^{-} (solid circles) in $Rb^{+}(15C5)_2Na^{-}$.

parallel to plane **ac** at 7.49 Å. Two other contacts on the same plane are at 7.75 Å. There are four contacts on the perpendicular plane **ab** at 8.42 Å. Along plane **ab** each Na^- is surrounded by four other anions at 8.92 Å. Because of the special positions occupied by rubidium and sodium, the cation-cation distances are equal to the anion-anion ones. By viewing the cell down the c-axis, the structure can be described as consisting of alternating two-dimensional layers of cations and anions. At c=0, a plane of anions is observed parallel to plane **ab**, with each anion being coordinated to four nearest coplanar anions at a distance of 8.92 Å. At c=1/2, the plane contains cations, with each cation surrounded by four nearest neighbors also at 8.92 Å. This arrangement of stacks repeats itself along the c axis. Figure 41 shows a surface contour representation [95] of the packing viewed down the c-axis. The figure shows a slice of the packing. This type of representation takes into account the van der Waals radii of the atoms. It clearly shows that a small portion of each crown ether penetrates into the layer of anions, forming a system of channels through the lattice, along plane **ab**. The anion sits in a cavity located at the intersection of the channels; at this point the diameter of the channel is largest. Figure 42(a) illustrates the channels as viewed down the b axis of the cell. Figure 42(b) is a cut along plane **ac** showing the cavity where the anion sits. The cavity is not completely spherical, but slightly elongated

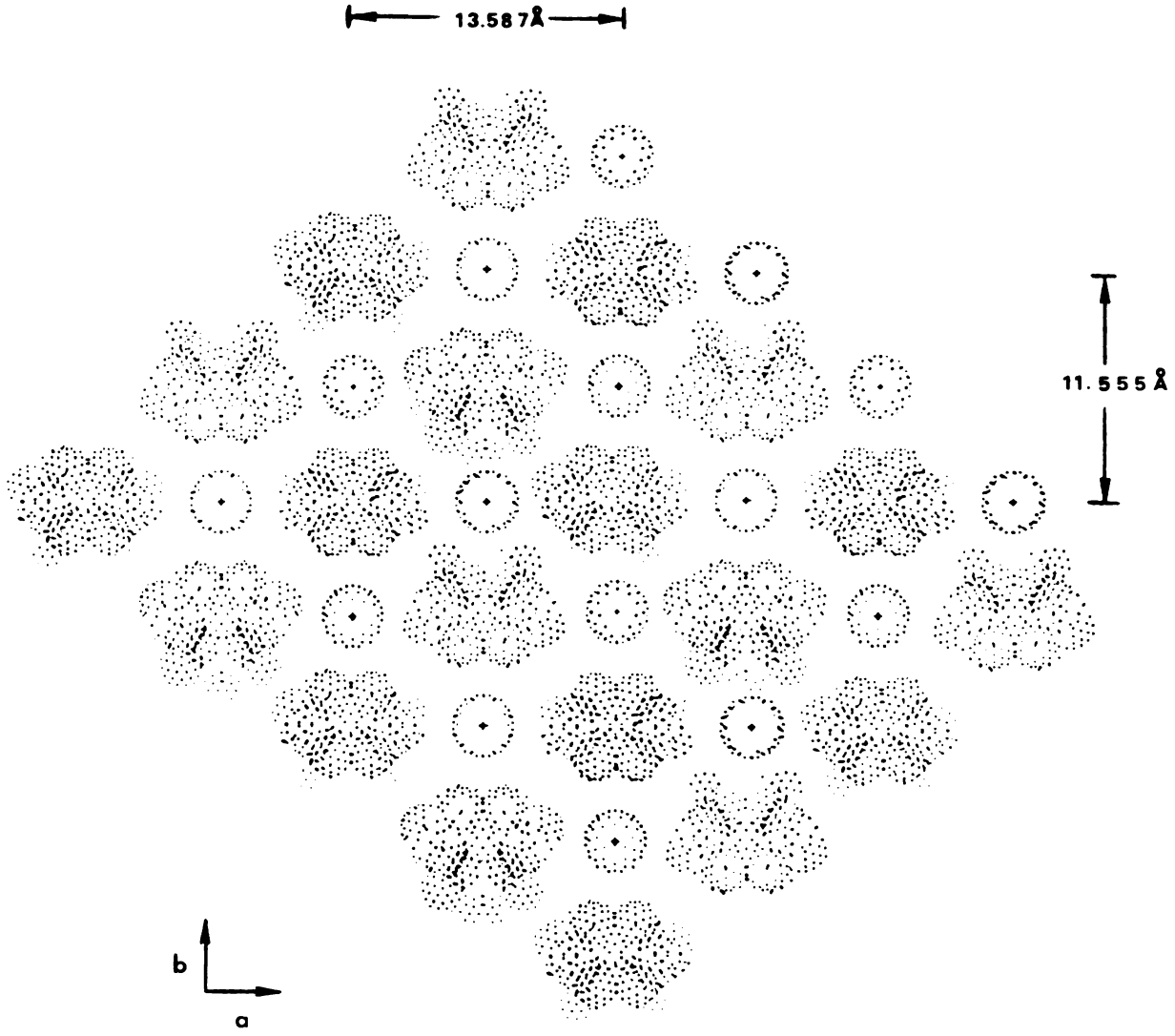

Figure 41. Surface contour representation of a thin slice of the packing of $Rb^{+}(15C5)_2$ and Na^{-} viewed along the c-axis.

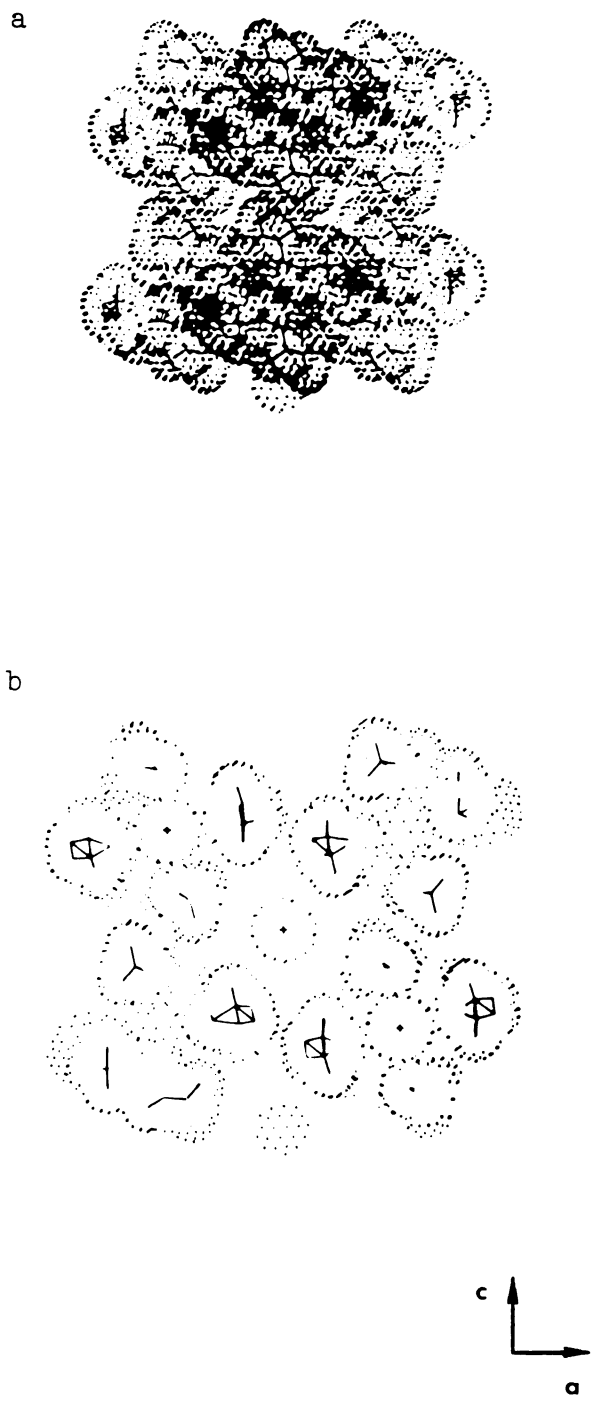

Figure 42. (a) Surface contour representation of the unit cell of $Rb^{+}(15C5)_2Na^{-}$ viewed down the b-axis. (b) Slice of the unit cell shown in (a).

along one dimension. It is possible that the interactions or the motion of the anions along the channels could give rise to anisotropy of the electrical properties of this compound. The EXAFS data presented in Chapter 4 indicated similarities in the local structure around rubidium between this sodide and the corresponding electride, $Rb^{+}(15C5)_2e^{-}$. If there were similarities in the packing, as was the case for $Cs^{+}(18C6)_2Na^{-}$ and $Cs^{+}(18C6)_2e^{-}$, it would be reasonable to expect anisotropy in the conductivity and other electrical properties of $Rb^{+}(15C5)_2e^{-}$ due to the motions or interactions of the electrons along the channels. Based upon this structure, we would expect the electride to behave as a 2-dimensional conductor.

Along the plane formed by the cations, the complexed cations are packed together so tightly that, as a result, there are no significant channels in the structure along the c-axis. This contrasts with $Cs^{+}(18C6)_2Na^{-}$ and $Cs^{+}(18C6)_2e^{-}$ in which the c-axis channels are the largest.

As mentioned, the sodium anion sits in a cavity surrounded by eight cations. Its nearest neighbors are hydrogens from the crown ether rings that line the cavity. It is possible to calculate an approximate value for the radius of the anion, by using the distances between the sodide and the neighboring hydrogens. The distances between the sodium anion and its nearest neighbors are given in Table 10. The estimated value for the van der

Table 10. Intermolecular Contacts Up To 4.63Å From Sodide Ion (in Angstroms) for $Rb^{+}(15C5)_2Na^{-}$ at 213 K

Atom1	Atom2	Distance	Anion Radius
Na1	H2a	4.38(7)	3.18
Na1	H3b	4.14(7)	2.49
Na1	H5a	4.26(8)	3.06
Na1	H8Ba	3.799	2.60
Na1	H8Bb	4.173	2.97

Numbers in parentheses are estimated standard deviations in the least significant digits.

Waals radius of aliphatic hydrogen is 1.2 Å [96]. By using these values, the radius of the sodium anion can be estimated to be between 2.60 and 3.18 Å. The lower limit only takes into account the closest contacts, while the upper limit takes into account the longest bond lengths. The average was estimated to be 2.99 Å. This value is in agreement with those obtained for $Cs^+(18C6)_2Na^-$ (average 2.65 Å [65]), and $Na^+C222Na^-$ (average 2.81 Å [57]).

The complexed rubidium sits at a crystallographic inversion center and has as nearest neighbors the ten oxygens of the two 15-crown-5 rings. The Rb^+- O distances are not equal and have values in the range of 2.986 to 3.067 Å with an average of 3.009 Å. These distances are slightly longer than the sum of the ionic radius of rubidium and the van der Waals radius of oxygen (sum equals 2.88 Å) and are not appreciably different from those found in the thiocyanate and bromide complexes of rubidium with 18-crown-6. The Rb^+- O distances in $Rb^+(18C6)SCN^-$ range from 2.93 Å to 3.15 Å, with an average of 3.024 Å [73], and those in $Rb^+(18C6)Br^-$ range from 2.86 Å to 3.10 Å, with an average of 2.978 Å. The similarity in the Rb^+- O distances in $Rb^+(15C5)_2$ with those in $Rb^+(18C6)$ in spite of the difference in the size of their cavities, is not a total surprise if one considers the fact that in both cases the cation sits above the plane formed by the oxygens of the crown ether. Table 11 features the pertinent bond

Table 11. Bond Distances (in Angstroms) for $Rb^{+}(15C5)_2Na^{-}$ at 213 K

Atom1	Atom2	Distance
Rb1	O1	3.067(7)
Rb1	O4	2.986(5)
Rb1	O7	3.003(5)
O1	C2	1.450(9)
O4	C3	1.408(9)
O4	C5	1.435(11)
O7	C6	1.420(12)
O7	C8A	1.554(13)
O7	C8B@	1.44(2)
C2	C3	1.486(12)
C5	C6	1.459(13)
C8A	C8B	1.51(2)
C2	H2a	1.04(7)
C2	H2b	1.02(6)
C3	H3a	1.07(9)
C3	H3b	0.87(6)
C5	H5a	0.92(7)
C5	H5b	0.97(6)
C6	H6a	1.10(9)
C6	H6b	0.84(6)
C8A	H8Aa	0.95
C8A	H8Ab	0.95
C8B	H8Ba	0.95
C8B	H8Bb	0.95

Numbers in parentheses are estimated standard deviations in the least significant digits.

@ indicates an atom at x, -y, z

distances. The bond angles and torsion angles are summarized in Tables 12 and 13 respectively.

5.2 Crystal Structure of $Rb^+(18C6)Br^-$ Dihydrate

The properties and structures of the complexes of alkali metal salts with crown ethers and cryptands have been extensively studied [46, 47, 97]. From these studies, considerable information about the complexation process has been obtained. In the study of alkalides and electrides, the complexes of alkali salts and crown ethers or cryptands are of particular interest, since the complexed salts can serve as effective structural models. Following the synthesis and structural determination of the first alkalide, $Na^+C222Na^-$, it was particularly convenient to compare the structural features to those of the corresponding iodide salt, Na^+C222I^- [2]. Indeed, similar Na^+- O and Na^+- N distances of the complexed cation were found in the two salts and the sodide ion was found to be similar to the iodide in its placement and distance from other atoms.

The model compounds were also useful both in solution and solid state alkali metal NMR studies. In the early studies of the ^{23}Na NMR spectra of solutions of $Na^+C222Na^-$, two distinct, well separated peaks were observed. The spectra of the sodide were compared to those of solutions of $Na^+C222Br^-$ [45,49]. The Na^+C222 peak of the sodide

Table 12. Selected Bond Angles (in Degrees) for $Rb^{+}(15C5)_2Na^{-}$ at 213 K

Atom1	Atom2	Atom3	Angle
O1	Rb1	O1#	180.00
O1	Rb1	O4	55.40(9)
O1	Rb1	O4#	124.60(9)
O1	Rb1	O7	84.9(2)
O1	Rb1	O7#	95.1(2)
O4	Rb1	O4#	180.00
O4	Rb1	O4@	109.4(1)
O4	Rb1	O4&	70.6(1)
O4	Rb1	O7	58.0(1)
O4	Rb1	O7#	122.0(1)
O4	Rb1	O7@	104.1(2)
O4	Rb1	O7&	75.9(2)
O7	Rb1	O7#	180.00
O7	Rb1	O7@	56.5(1)
O7	Rb1	O7&	123.5(1)
Rb1	O1	C2	105.0(4)
C2	O1	C2@	113.2(7)
Rb1	O4	C3	119.5(4)
Rb1	O4	C5	110.3(4)
C3	O4	C5	113.0(6)
Rb1	O7	C6	116.2(4)
Rb1	O7	C8A	108.3(5)
Rb1	O7	C8B@	120.2(7)
C6	O7	C8A	127.2(7)
C6	O7	C8B@	92.9(8)
O1	C2	C3	105.5(6)
O4	C3	C2	109.7(7)
O4	C5	C6	113.8(7)
O7	C6	C5	109.1(7)
O7	C8A	C8B	109.(1)
O7	C8B@	C8A@	98.(1)

Numbers in parentheses are estimated standard deviations in the least significant digits.

@ indicates an atom at x, -y, z
# indicates an atom at 1-x, -y, 1-z
& indicates an atom at 1-x, y, 1-z

Table 13: Selected Torsion Angles in Degrees for $Rb^{+}(15C5)_2Na^{-}$ at 213 K

Atom 1	Atom 2	Atom 3	Atom 4	Angle
C2@	O1	C2	C3	175.01 (0.55)
C5	O4	C3	C2	-161.90 (0.66)
C3	O4	C5	C6	80.78 (0.88)
C8A	O7	C6	C5	174.48 (0.82)
C8B@	O7	C6	C5	-167.14 (0.66)
C6	O7	C8A	C8B	82.79 (1.19)
C6	O7	C8B@	C8A@	175.93 (0.43)
O1	C2	C3	O4	69.51 (0.79)
O4	C5	C6	O7	67.30 (0.93)
O7	C8A	C8B	O7@	76.22 (1.08)

@ indicates an atom at x, -y, z

occurred at the same chemical shift as in the bromide. Thus, the bromide salt was an effective reference compound in the assignment of the NMR peaks obtained for $Na^+(C222)Na^-$.

The structure of $Rb^+(18C6)Br^-$ was of interest for a number of reasons. First, to be able to interpret the X-ray absorption data obtained by EXAFS and XANES spectroscopies, it was necessary to compare the data to those of stable model compounds of known structure. Structural information on alkalides and electrides containing rubidium was necessary. ^{87}Rb solid state NMR studies had failed to provide information about the complexed rubidium cation due to the extreme quadrupolar brodadening of its signal. Furthermore, several attempts at direct structural determination of $Rb^+(18C6)Na^-$ and Rb(18C6) by single crystal X-ray diffraction have failed. In the case of the sodide, relatively stable, well-formed crystals were obtained [98]. However, it was not possible to determine the space group from the obtained data. It has been postulated that the compound crystallizes in a superlattice. In the case of Rb(18C6), small crystals were obtained after many crystallization attempts; however, the collected intensities of reflection were extremely weak and assignment of the space group was not possible.

The structure of $Rb^+(18C6)Br^-$ dihydrate was determined to serve as a structural model in the EXAFS and XANES studies of alkalide and electride salts that contain

$Rb^+(18C6)$ as the cation. It was expected that the spherical bromide anion would make this salt a particularly effective model.

5.2.1 Crystal Selection and Mounting: $Rb^+(18C6)Br^-$ Dihydrate

The colorless crystals of $Rb^+(18C6)Br^-$ dihydrate were prepared as described in Chapter 2. A single crystal of approximate dimensions 0.5 x 0.5 x 0.5 mm^3 was picked from the mother liquor and mounted inside of a fine glass capilary. The tube was then sealed and mounted on the diffractometer.

5.2.2 Data Collection and Reduction

The preliminary inspection of the crystal and the subsequent collection of the diffraction data were done at 295(1) K by using Mo K_{α_1} radiation (λ = 0.70926 Å) on a Picker FACS -I automatic diffractometer equipped with a graphite crystal monochromator.

The precise unit cell parameters were determined by a least-squares fit to the setting angles of 16 reflections in the range $35^\circ \leq 2\theta \leq 40^\circ$. The unit cell was found to be orthorhombic with parameters a = 10.110(3), b = 15.173(5), and c = 12.519(5) Å, and calculated volume V = 1920.4 $Å^3$. For Z=4 and formula weight 465.72 g/m, the calculated density is 1.611 g/cm^3. The orthorhombic space group and

diffraction conditions allowed assignment of the space group as P_{nma} (#62 in the International Tables for X-Ray Crystallography [87]). The crystal data are summarized in Table 14.

A total of 3189 refections were measured, of which 2911 were unique. Three standard reflections: 4 0 0, 0 0 4 and 0 3 1, were monitored throughout the data collection to serve as reference for crystal and instrumental stability. The loss in intensity at the end of the data collection amounted to 4%. A linear decay correction of 2% was applied on F. Lorentz and polarization corrections and an analytical absorption correction [99] were applied.

Table 14. Summary of Crystal Data for $Rb^+(18C6)Br^-$ Dihydrate

---

F. W. 465.72 g/m F(000) = 944

Mo $K_{\alpha 1}$ radiation (λ = 0.70926 Å)

Temperature = 295(1) K

Orthorhombic space group P_{nma}

a = 10.110(3) b = 15.173(5) c = 12.519(5) Å

V = 1920.4 $Å^3$

Z = 4 D_x = 1.611 g/cm^3

5.2.3 Structure Solution and Refinement

The crystal structure was solved by the Patterson heavy-atom method, which revealed the positions of the rubidium and bromide ions. Direct methods verified the heavy-atom positions obtained from the Patterson maps. The atomic scattering factors were taken from Cromer and Waber [92]. Corrections for anomalous dispersion effects were included [94]. The structure was refined in full-matrix least-squares. The final cycle of refinement converged with unweighted and weighted agreement factors of 0.057 and 0.036, respectively. The calculations were performed on DEC PDP 8/I, DEC PDP 11/40 and CDC Cyber 170 Model 750 computers.

5.2.4 Description of the Structure of $Rb^{+}(18C6)Br^{-}$ Dihydrate

The final positional parameters with their estimated standard deviations and isotropic thermal displacement factors are listed Table 15. The anisotropic thermal parameters with their estimated standard deviations are listed in Table 16. A stereographic view of the unit cell is shown in Figure 43. The rubidium, the bromide and one half of one 18-crown-6 are unique; a mirror plane bisects the crown ether ring through oxygens O(1) and O(10). The rubidium and bromide ions lie on this plane. The rubidium

Table 15. Positional Parameters and Their Estimated Standard Deviations (in Parenthesis) for $Rb^{+}(18C6)Br^{-}$ Dihydrate

Atom	X	Y	Z	B(Å^2)
Rb	-0.13424(8)	0.750	0.01121(8)	4.04
Br	-0.15549(9)	0.250	0.14468(10)	5.78
O(1)	0.0330(6)	0.750	0.2068(5)	4.74
O(10)	-0.4119(6)	0.750	-0.0339(5)	5.42
C(2)	0.1108(8)	0.6726(6)	0.2041(8)	5.71
C(3)	0.0225(9)	0.5936(6)	0.2112(8)	5.66
O(4)	-0.0561(5)	0.5882(3)	0.1196(4)	4.73
C(5)	-0.1372(9)	0.5119(5)	0.1195(8)	5.38
C(6)	-0.2256(9)	0.5161(6)	0.0247(9)	5.51
O(7)	-0.3145(4)	0.5861(3)	0.0363(4)	4.92
C(8)	-0.4003(8)	0.5962(7)	-0.0534(8)	5.39
C(9)	-0.4878(8)	0.6717(6)	-0.0302(8)	5.70
O(W1)	0.1232(4)	0.1361(4)	0.2049(5)	7.75
H(2A)	0.179(5)	0.673(4)	0.261(5)	4.6(15)
H(2B)	0.157(7)	0.670(5)	0.136(5)	6.6(22)
H(3A)	-0.028(4)	0.599(3)	0.277(4)	1.9(13)
H(3B)	0.68(6)	0.541(4)	0.229(5)	5.0(17)
H(5A)	-0.193(6)	0.517(4)	0.186(4)	4.0(15)
H(5B)	-0.083(5)	0.470(4)	0.107(5)	4.4(17)
H(6A)	-0.269(6)	0.470(4)	0.012(6)	4.9(19)
H(6B)	-0.179(6)	0.521(4)	-0.036(5)	4.2(19)
H(8A)	-0.448(6)	0.546(5)	-0.066(5)	6.0(20)
H(8B)	-0.350(6)	0.609(4)	-0.126(6)	6.5(19)
H(9A)	-0.546(6)	0.670(4)	-0.080(5)	3.7(16)
H(9B)	-0.533(7)	0.664(5)	0.039(6)	7.5(25)
H(W1A)	0.039	0.171	0.188	8.6
H(W1B)	0.187	0.170	0.250	8.6

Table 16. Anisotropic Thermal Parameters and Standard Deviations for $Rb^{+}(18C6)Br^{-}$ Dihydrate (in $Å^2$).

Name	B(1,1)	B(2,2)	B(3,3)	B(1,2)	B(1,3)	B(2,3)
Rb	4.29(4)	3.60(4)	4.23(5)	0	0.19(4)	0
Br	3.98(4)	5.85(7)	7.51(8)	0	0.85(5)	0
O(1)	5.6(3)	3.0(3)	5.6(4)	0	-1.3(3)	0
O(10)	4.1(3)	5.5(4)	6.7(5)	0	-0.5(3)	0
C(2)	6.1(5)	4.6(5)	6.4(5)	0.5(4)	-2.3(5)	0.3(4)
C(3)	7.9(5)	3.6(4)	5.5(5)	1.4(4)	-0.6(5)	0.6(4)
O(4)	5.8(2)	3.3(2)	5.1(3)	-0.3(2)	-0.9(2)	0.4(2)
C(5)	5.5(4)	2.7(4)	8.0(6)	0.7(4)	1.7(5)	0.3(4)
C(6)	5.0(4)	4.5(5)	7.0(6)	-0.9(4)	0.9(5)	-1.0(5)
O(7)	5.1(2)	4.1(3)	5.6(3)	0.5(2)	0.3(2)	-0.3(2)
C(8)	5.7(4)	5.1(5)	5.4(5)	-1.5(4)	-0.9(4)	0.2(4)
C(9)	4.5(4)	5.9(5)	6.7(7)	-1.1(4)	-1.7(4)	0.6(5)
O(W1)	7.4(3)	7.3(3)	8.6(4)	-0.1(3)	-1.1(3)	-1.9(3)

The temperature factor has the form:

$$T = -SUM (H(I)*H(J)*BIJ*ASTAR(I)*ASTAR(J)) / 4$$

where H is the Miller Index, ASTAR is the reciprocal cell length, and I and J are cycled 1 through 3.

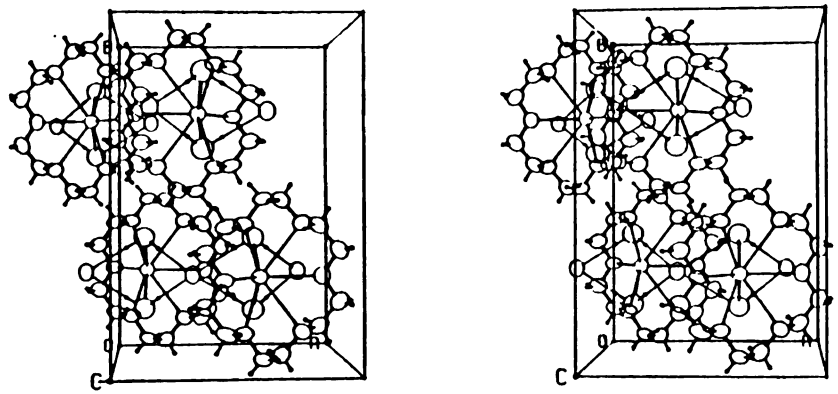

Figure 43. Stereoscopic view of the unit cell of $Rb^{+}(18C6)Br^{-}$ Dihydrate (viewed down c-axis).

cation is coordinated to the six oxygens of the 18-crown-6 at unequal distances ranging from 2.86 to 3.10 Å, with an average distance of 2.98 Å. The rubidium cation is slightly displaced from the mean plane formed by the oxygens of the hexaether. The rubidium coordination is completed by contacts to the oxygens of the two water molecules at 3.212 Å. The Rb^+ distances to the bromide anions are slightly longer at 3.52 Å. This $Rb^+ - Br^-$ value is slightly longer than the sum of the ionic radius of bromide and the van der Waals radius of oxygen (sum is 3.43 Å). Each bromide is bridged by hydrogen bonding to two adjacent anions by four water molecules, thus forming a one-dimensional chain throughout the cell along **a**. The Br^-- H distances are 2.37 and 2.40 Å. The complexed rubidium cations are attached to the chain by their coordination to the oxygens of water molecules. The planes of oxygen atoms on adjacent complexes form an angle of approximately 66^o with respect to each other. This is illustrated in Figure 44. Table 17 and Table 18 list the interatomic distances and interatomic angles respectively. The torsion angles are given in Table 19.

The conformation of the 18-crown-6 ring in $Rb^+(18C6)Br^-$ can be described as D_{3d}. This is the same conformation present in the thiocyanate complex $Rb^+(18C6)SCN^-$, as well as in the 18-crown-6 complexes with KSCN and CsSCN [73]. Similarities in the bond lengths and angles in both complexes are evidence for this assignment.

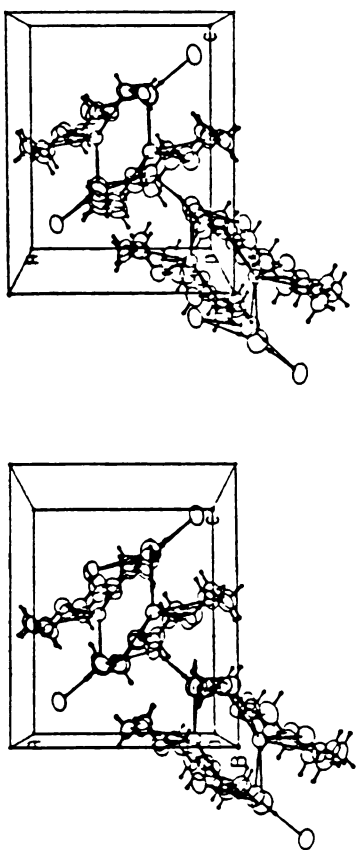

Figure 44. Stereoscopic view of the unit cell of $Rb^{+}(18C6)Br^{-}$ Dihydrate (viewed down the b-axis).

Table 17. Bond Distances (in Angstroms) and Estimated Standard Deviations (in Parentheses) for $Rb^{+}(18C6)Br^{-}$ Dihydrate.

Atom1	Atom2	Distance
O(1)	Rb	2.976(6)
O(4)	Rb	2.915(5)
O(7)	Rb	3.098(5)
O(10)	Rb	2.863(6)
O(W1)	Rb	3.212(6)
O(W1)	Br	3.390(5)
O(W1)'	Br	3.397(5)
C(2)	O(1)	1.414(8)
C(3)	C(2)	1.497(11)
O(4)	C(3)	1.397(9)
C(5)	O(4)	1.418(8)
C(6)	C(5)	1.487(11)
O(7)	C(6)	1.400(9)
C(8)	O(7)	1.427(9)
C(9)	C(8)	1.476(11)
O(10)	C(9)	1.415(8)
H(W1A)	Br	2.365
H(W1B)	Br	2.398
H(2A)	C(2)	0.99(6)
H(2B)	C(2)	0.98(6)
H(3A)	C(3)	0.97(5)
H(3B)	C(3)	0.95(6)
H(5A)	C(5)	1.01(5)
H(5B)	C(5)	0.86(6)
H(6A)	C(6)	0.83(6)
H(6B)	C(6)	0.90(6)
H(8A)	C(8)	0.92(7)
H(8B)	C(8)	1.06(7)
H(9A)	C(9)	0.86(6)
H(9B)	C(9)	0.99(7)
H(W1A)	O(W1)	1.03
H(W1B)	O(W1)	1.00

' indicates an atom at -1/2+X, Y, 1/2-Z

Table 18. Selected Bond Angles (in Degrees) and Estimated Standard Deviations (in Parentheses) for $Rb^{+}(18C6)Br^{-}$ Dihydrate.

Atom1	Atom2	Atom3	Angle
O(1)	Rb	O(4)	57.50(14)
O(1)	Rb	O(7)	104.53(18)
O(1)	Rb	O(10)	136.00(29)
O(1)	Rb	O(W1)	132.32(17)
O(4)	Rb	O(7)	55.69(12)
O(4)	Rb	O(10)	110.95(16)
O(4)	Rb	O(W1)	85.96(16)
O(4)@	Rb	O(4)	114.79(9)
O(4)@	Rb	O(7)	142.02(19)
O(4)@	Rb	O(W1)	146.73(19)
O(7)	Rb	O(10)	56.18(12)
O(7)	Rb	O(W1)	70.97(13)
O(7)@	Rb	O(7)	106.72(9)
O(7)@	Rb	O(W1)	122.51(18)
O(10)	Rb	O(W1)	82.41(16)
O(W1)$	Rb	O(W1)*	65.10(18)
Rb	O(1)	C(2)	107.25(38)
Rb	O(4)	C(3)	119.13(37)
Rb	O(4)	C(5)	122.01(39)
Rb	O(7)	C(6)	102.77(39)
Rb	O(7)	C(8)	101.05(39)
Rb	O(10)	C(9)	121.67(37)
O(W1)	Br	O(W1)'	99.48(15)
O(W1)	Br	O(W1)"	61.30(10)
O(W1)	Br	O(W1)#	133.12(26)
O(W1)'	Br	O(W1)"	133.12(9)
O(W1)'	Br	O(W1)#	61.16(14)
O(W1)"	Br	O(W1)#	99.48(21)
C(2)	O(1)	C(2)	112.31(34)
O(1)	C(2)	C(3)	109.39(63)
C(2)	C(3)	O(4)	109.74(74)
C(3)	O(4)	C(5)	112.21(75)
O(4)	C(5)	C(6)	108.30(61)
C(5)	C(6)	O(7)	109.58(70)
C(6)	O(7)	C(8)	112.96(81)
O(7)	C(8)	C(9)	107.00(63)
O(10)	C(9)	C(8)	108.66(61)
C(9)	O(10)	C(9)	114.20(34)
Rb=	O(W1)	Br	64.37(9)
Rb=	O(W1)	Br&	99.80(10)
Br&	O(W1)	Br	114.28(9)

' indicates an atom at -1/2+X, Y, 1/2-Z; " indicates an atom at X, 1/2-Y, Z; # indicates an atom at -1/2+X, 1/2-Y, 1/2-Z; @ indicates an atom at X, 3/2-Y, Z; $ indicates an atom at 1-X, 1/2+Y, -Z; * indicates an atom at 1-X, 1-Y, -Z; & indicates an atom at 1/2+X, Y, 1/2-Z; = indicates an atom at X, 1-Y, -Z.

Table 19. Selected Torsion Angles in Degrees for $Rb^{+}(18C6)Br^{-}$ Dihydrate.

Atom 1	Atom 2	Atom 3	Atom 4	Angle
C(2)@	O(1)	C(2)	C(3)	177.97
O(1)	C(2)	C(3)	O(4)	66.05
C(2)	C(3)	O(4)	C(5)	177.03
C(3)	O(4)	C(5)	C(6)	174.87
O(4)	C(5)	C(6)	O(7)	-66.70
C(5)	C(6)	O(7)	C(8)	178.13
C(6)	O(7)	C(8)	C(9)	179.92
O(7)	C(8)	C(9)	O(10)	70.19
C(8)	C(9)	O(10)	C(9)@	170.25

@ indicates an atom at X, 3/2-Y, Z.

The torsion angles about C - C bonds are close to 65°: 66.1° to 70.2° in the bromide, and 59.6° to 67.3° in the thiocyanate. The torsion angles about C - O bonds are close to 180°: 170.3° to 179.9° in the bromide and 168.8° to 179.1° in the thiocyanate. The C - C - O bond angles are close to tetrahedral: 107.0° to 109.7° in the bromide and 110.9° to 114.1° in the thiocyanate. The C - O - C angles are slightly wider: 112.2° to 114.2° in the bromide and 110.9° to 114.10° in the thiocyanate. The bond lengths are very similar in $Rb^+(18C6)Br^-$ and $Rb^+(18C6)SCN^-$, with C - C bonds in the range of 1.48 Å to 1.50 Å and C - O bond lengths ranging from 1.40 Å to 1.44 Å in both complexes.

$Rb^+(18C6)Br^-$ dihydrate was used as a model compound in the studies by EXAFS and XANES spectroscopies, as described in Chapter 4. It was effective in modeling the local structure in the vicinity of the rubidium cation, particularly, the Rb^+ - O distances between the cation and ligand. It is possible that this similarity in distances indicates that the conformation of the hexaether in $Rb^+(18C6)Na^-$, $Rb^+(18C6)Rb^-$, and Rb(18C6) is similar to that found in the bromide and the thiocyanate complexes. However, this cannot be ascertained without information about the bond angles. The coordination sphere around the rubidium cation in the bromide salt is complicated by the bonding to the oxygens of water molecules and by the effect of the hydrygen bonding in linking the complexes in a quasi-one dimensional chain. Although the BFBT of the

EXAFS data showed coordination distances at 3.60 Å and 3.64 Å for $Rb^{+}(18C6)Rb^{-}$ and Rb(18C6) respectively, it is not possible with the available data to make assignments or to speculate whether these distances would correspond to a complicated coordination similar to that found in the bromide.

CHAPTER SIX

PREPARATION OF M^- IN SOLUTION IN THE PRESENCE OF $Li(CH_3NH_2)_4$

The stability of solutions of the alkali metals and complexing agents in amines and ethers is of crucial importance to the preparation and characterization of alkalides and electrides. The recent success in the preparation of new compounds and in the crystallization of alkalides and electrides that had been prepared previously only as powders, is due, in great part, to the use of a number of solvents which are resistant to decomposition. The solvents that thus enhance the stability of the solutions do not contain β or acidic hydrogen atoms.

Prior to the use of these solvents, for the preparation of the most unstable compounds, lithium metal was added to the solutions of the starting materials in methylamine, since it had been found that the solutions containing lithium were much more stable than those containing only the starting materials [12, 19]. The added lithium enhanced the stability of the solutions throughout the synthesis, even after the addition of cosolvents such as 2-aminopropane or diethylether. At the end of the synthesis, the lithium remained in solution, and it was possible to just rinse it off the crystals. Initially,

lithium had been added to solutions containing cesium and 18-crown-6 with the object of increasing the electron concentration in the product, in an attempt to enhance electron delocalization [12]. The extent of the additional stability provided by the lithium was sufficient to enable the preparation of a variety of compounds not possible without the use of lithium in the solutions.

Although the exact mechanism of the stabilization was not completely understood, it was believed that lithium could inhibit the autocatalytic decomposition process, probably by reaction with free radicals, anion radicals or amide ions which take part in a chain decomposition reaction [12].

Another feature of the stabilization by lithium that was not fully understood was the apparent solubilization of the metal in a number of solvents used for syntheses, such as 2-aminopropane. Lithium metal is insoluble in this solvent. It was found that, while pure lithium is insoluble in the solvents used, $Li(CH_3NH_2)_4$ is not. Thus, if some methylamine was left in solution after the dissolution of the starting materials, the lithium would remain in solution [100].

During the course of the present work, it was observed that the presence of lithium in the solutions of the starting materials appeared to produce solubilization of the other alkali metals present in solution, even in the absence of complexing agents. For example, sodium is

only slightly soluble in methylamine in the absence of a complexant [101]. By having an equimolar amount of lithium present in solution, it was possible to dissolve the sodium metal in the absence of complexing agents, to produce solutions with concentrations at least 0.1 M in sodium and lithium. The same effect was observed for rubidium in methylamine.

These data suggest that the solubilization of sodium, rubidium and the other alkali metals in methylamine in the presence of lithium occurs through the formation, in solution, of $Li^{+}(CH_3NH_2)_4M^{-}$, where M^{-} corresponds to Na^{-}, Rb^{-}, etc. To probe the nature of the species produced in these solutions, the optical spectra of the solutions were measured. Initially, the absorption spectrum of a thin film of the solution of lithium in methylamine was measured. Subsequently, the solution was poured onto a sodium mirror; the sodium was dissolved, and the optical spectrum was measured again.

The solutions were prepared by using the same techniques used in the preparation of solutions for the syntheses of alkalides and electrides. The procedures were described in Chapter 3.

The optical spectrum of a thin damp film of the solution of lithium in methyamine is illustrated in Figure 45. The spectrum shows the typical plasma absorption characteristic of an "expanded metal", in which the electrons are delocalized. This spectrum has been obtained

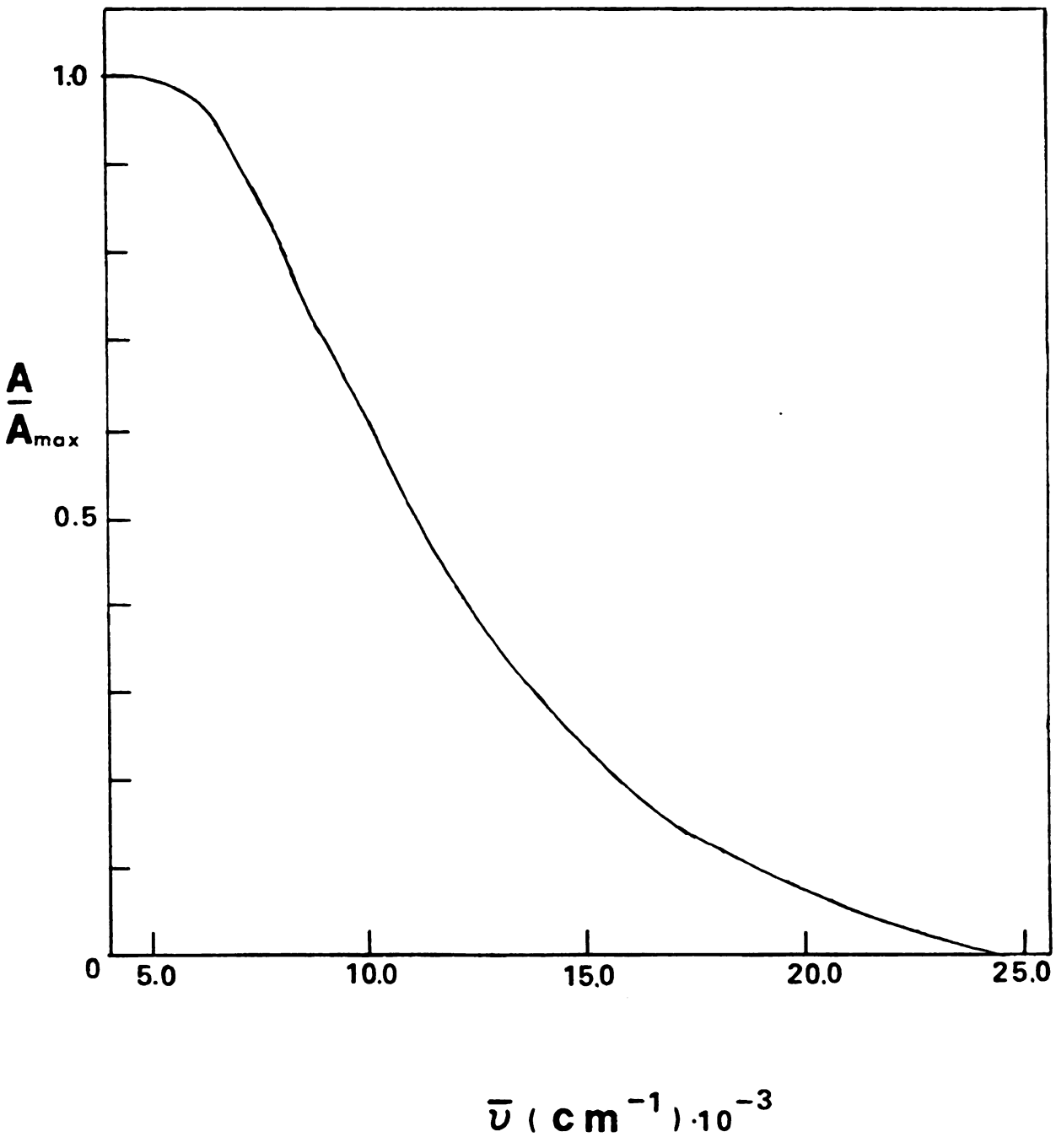

Figure 45. Optical spectrum of a thin film of Li $(CH_3NH_2)_4$.

previously and was used to verify the metallic nature of the concentrated lithium solutions in methylamine.

After sodium was added to the solutions, the spectrum illustrated in Figure 46 was obtained. The plasma absorption disappeared, and instead, a band at 660 nm, characteristic of the absorption by Na^-, was observed. These experimental observations agree with the proposed formation of $Li^+(CH_3NH_2)_4M^-$.

The preparation of $Li^+(CH_3NH_2)_4M^-$ in the solid state was attempted by following the procedures used for the preparation of crystalline samples of alkalides and electrides. These attempts were, however, unsuccessful.

In conclusion, the preliminary results presented here indicate that $Li(CH_3NH_2)_4$ is a powerful reducing agent, that can solubilize the alkali metals by forming the alkali metal anions in solution. The conditions necessary for the isolation of salts of the form $Li^+(CH_3NH_2)_4M^-$ should be investigated.

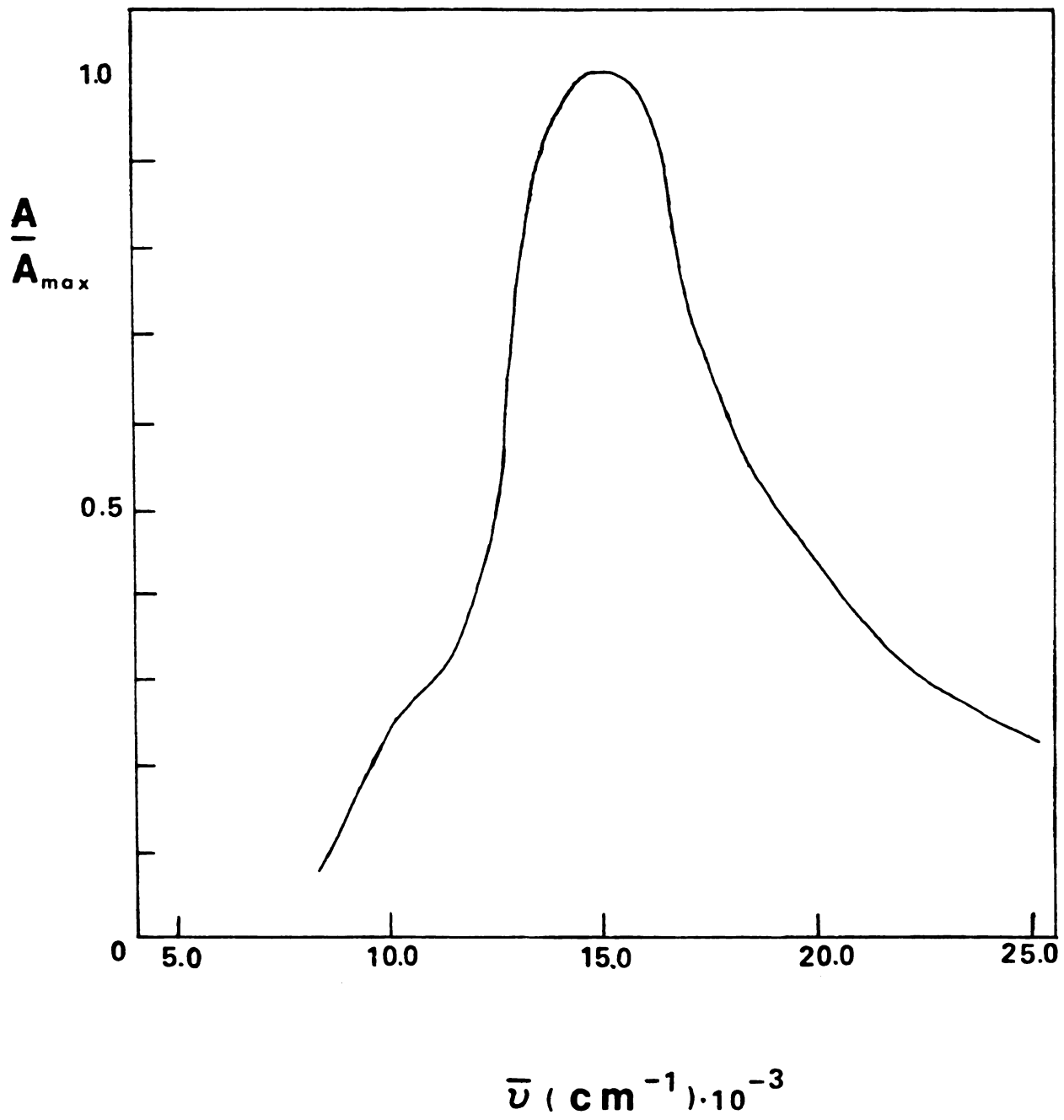

Figure 46. Optical spectrum of a thin film of $Li^{+}(CH_3NH_2)_4Na^{-}$.

CHAPTER SEVEN

CONCLUSIONS AND SUGGESTIONS FOR FUTURE WORK

7.1 Conclusions

Three new rubidides, $Cs^+(18C6)_2Rb^-$, $K^+C222Rb^-$, and $Li^+C211Rb^-$ were synthesized. Of the three, $Cs^+(18C6)_2Rb^-$ is the most stable and this allowed its complete characterization. The identification of this salt as a pure rubidide was achieved through the combined use of optical spectroscopy, ^{87}Rb and ^{133}Cs solid state NMR, and rubidium K-edge XANES studies. Studies by EPR, magnetic susceptibility and dc conductivity indicated that this compound contains a small concentration of non-interacting trapped electrons. $K^+C222Rb^-$ was identified as a rubidide by optical spectroscopy and XANES. Detailed studies of the electronic poperties of this compound, or of $Li^+C211Rb^-$, however, were not possible due to their high instability.

The techniques necessary for the handling, mounting and transport of the sensitive single crystals of alkalides and electrides were developed. The structure of $Rb^+(15C5)_2Na^-$ was obtained by single crystal X-ray diffraction. The unit cell was found to be monoclinic, in the space group C2/m with lattice parameters

a = 11.555(3) Å, b = 13.587(3) Å, c = 9.958(3) Å and β = 92.03(2)°. Each ion is surrounded by eight counterions. By viewing the cell along the c-axis, the structure can be described as consisting of alternating two-dimensional layers of cations and anions. The cation layers contain tightly packed $Rb^+(15C5)_2$ cations and penetrate slightly into the anion layers, thus forming a series of channels along which the anions are localized.

The structure of $Rb^+(18C6)Br^-$ dihydrate was obtained by single crystal X-ray diffraction, in order to use it as a structural model for compounds of the form $Rb^+(18C6)M^-$, in the studies by EXAFS and XANES. The unit cell is orthorhombic in the space group P_{nma}, with cell parameters a = 10.110(3) Å, b = 15.173(5) Å, c = 12.519(5) Å and V = 1920.4 $Å^3$.

An extensive series of rubidium-containing alkalides and electrides was studied by rubidium K-edge XANES and EXAFS spectroscopies. The XANES studies involved the measurement and comparison of the relative areas of the white lines in the spectra of the rubidium-containing salts. These studies allowed the unambiguous identification of the heteronuclear alkalides $Cs^+(18C6)_2Rb^-$, $K^+C222Rb^-$ and $Cs^+(15C5)_2Rb^-$ as pure rubidides, and of $RbK(15C5)_2$ and RbK(18C6) as mixtures of both potasside and rubidide. XANES results also provided the identification of $Rb^+(15C5)_2Na^-$ and $Rb^+(18C6)Na^-$ as pure sodides with complexed rubidium for the cations. For

powders of the homonuclear compounds of rubidium and 15C5 and rubidium and C222, XANES permitted identification of the electrides $Rb^+(15C5)_2e^-$ and $RbC222e^-$, distinguishing them from the rubidides $Rb^+(15C5)_2Rb^-$ and $Rb^+C222Rb^-$. While some of these assignments have been confirmed by solid state NMR results, others are only possible by using XANES. The ^{87}Rb NMR signal of cations of the form Rb^+C cannot be observed due to extreme quadrupolar broadening.

The Rb K-edge EXAFS results for a series of salts of the form Rb^+CN^-, where C represents either 15-crown-5 or 18-crown-6 and N^- represents Na^-, Rb^- or e^- have provided structural information about the local environment of the complexed rubidium in the salts. Model compounds were necessary. For the compounds containing 15-crown-5, the sodide, $Rb^+(15C5)_2Na^-$ was employed as the model. The data for this series indicated distances for the corresponding electride and rubidide, $Rb^+(15C5)_2e^-$ and $Rb^+(15C5)_2Rb^-$, which are very close to those of the sodide. Similar values for the number of nearest neighbors were also obtained. This would lead one to expect very similar local structures around the cation in the three salts. For the compounds containing $Rb^+(18C6)$ as the cation, the salts $Rb^+(18C6)Br^-$dihydrate and $Rb^+(18C6)SCN^-$ were used as models. The data for the corresponding sodide $Rb^+(18C6)Na^-$, indicates two types of coordinating atoms, presumably the usual oxygen and carbon neighbors. The coordination numbers correspond to a single complexant

molecule per cation. The distances corresponding to the anion contacts are longer than 4 Å, and thus, were not observed. The data for the two compounds $Rb^+(18C6)Rb^-$ and Rb(18C6) indicates a structure different from that of $Rb^+(18C6)Na^-$ in that three different sets of distances are obtained. The Rb^+ - O and Rb^+ - C distances for these compounds fall in the expected range of 2.92 - 2.99 Å and 3.75 - 3.77 Å respectively. The remaining distances, at 3.60 and 3.64 Å for $Rb^+(18C6)Rb^-$ and Rb(18C6), respectively, are too short to be cation - anion contacts and could be elongated Rb^+ - O distances, perhaps due to a distortion in the crown ether ring.

It is clear that the structural information obtained from EXAFS is limited in some respects. No information regarding the long-range arrangement of the molecular units in the lattice is obtained. In addition, because of the long distances involved, no information is provided about the species surrounding the anions. Also, no idea about the conformation of the complexant around the complexed cation can be obtained due to the lack of information about bond angles. However, with the exception of single crystal X-ray diffraction, no other technique attempted by us thus far has provided the amount of structural information obtained from these EXAFS studies.

Studies of the solutions of lithium in methylamine indicate that $Li(CH_3NH_2)_4$ is a strong reducing agent,

capable of solubilizing the alkali metals by forming $Li^{+}(CH_3NH_2)_4M^{-}$ in solution.

7.2 Suggestions for Future Work

The EPR, magnetic susceptibility, and dc conductivity data for $Cs^{+}(18C6)_2Rb^{-}$ indicated that this solid contains a small concentration of non-interacting trapped electrons. This compound seems to be a prime candidate for the preparation of a rubidide salt doped with electride. The mixed sodide/electride, $Cs^{+}(18C6)_2Na^{-}{}_{0.15}e^{-}{}_{0.85}$ has already been prepared [65]. Increasing the concentration of trapped electrons in the rubidide could result in increased electron-electron interactions. Along the same lines, it would also be of interest to introduce various concentrations of trapped electrons into $Rb^{+}(15C5)_2Na^{-}$. As shown by the crystal structure, this sodide contains interpenetrating channels along plane **ab** of the single crystal. Introducing a high content of trapped electrons could lead to strong electron-electron interactions along the channels and the onset of two-dimensional conductivity.

The use of differential scanning calorimetry should become standard practice in the study of every alkalide and electride prepared. DSC would be particularly useful in providing a better understanding on some of the physical properties shown by alkalides. For example, the ln vs. reciprocal temperature plot of $Cs^{+}(18C6)Rb^{-}$ shows a change

of slope (Chapter 3); DSC would be of great help in determining whether this result is due to a phase transition or similar effect.

The technique of powder X-ray diffraction should be used to supplement the short-range structural data obtained from EXAFS for compounds for which it is not possible to obtain high quality single crystals.

The XANES and EXAFS studies should continue to be used for those compounds for which high quality single crystals cannot be obtained. Potassium K-edge EXAFS should be feasible and could offer significant structural information, especially when combined with the data obtained from X-ray powder diffraction.

The preparation of solids of the form $Li^{+}(CH_3NH_2)_4M^{-}$, where M^{-} represents Na^{-}, K^{-}, etc. should be investigated. This should involve the use of a variety of solvents and crystallization conditions. Perhaps the use of a solvent with a stronger tendency for complexation (such as the bidentate ligand ethylenediamine) would allow the preparation of this novel type of alkalide.

REFERENCES

REFERENCES

1. J. L. Dye, J. M. Ceraso, M. T. Lok, B. L. Barnett, F. J. Tehan, J. Am. Chem. Soc., **96**, 608 (1974).

2. F. J. Tehan, B. L. Barnett, J. L. Dye, J. Am. Chem. Soc., **96**, 7203 (1974).

3. J. L. Dye, C. W. Andrews, S. E. Mathews, J. Phys. Chem., **79**, 3065 (1975).

4. J. L. Dye, J. Chem. Educ., **54**, 332 (1977).

5. J. L. Dye, Sci. American, **237**, 92 (July, 1977).

6. J. L. Dye, Angew. Chem. Int. Ed. Eng., **18**, 587 (1979).

7. J. L. Dye, in Progress in Macrocyclic Chemistry, R. M. Izatt and J. J. Christensen, Eds., Vol.1, Wiley-Interscience, New York, 1979, p. 63.

8. J. L. Dye, J. Phys. Chem., **84**, 1084 (1980).

9. B. Van Eck, L. D. Le, D. Issa and J. L. Dye, Inorg. Chem., **21**, 1966 (1982).

10. J. L. Dye, J. Phys. Chem., **88**, 3842 (1984).

11. J. L. Dye, A. Ellaboudy, Chemistry in Britain, **3**, 210 (1984).

12. J. L. Dye, Prog. Inorg. Chem., **32**, 327 (1984).

13. B. Dietrich, J.-M. Lehn, and J. P. Sauvage, Tetrahedron Lett., 2885, 2889 (1969).

14. J.-M. Lehn, J. P. Sauvage, B. Dietrich, J. Am. Chem. Soc., **92**, 2916 (1970).

15. C. J. Pedersen, J. Am. Chem. Soc., **89**, 7017 (1967); **92**, 386 (1970).

16. C. J. Pedersen, Fed. Proc., **27**, 1305 (1968).

17. J. L. Dye, M. R. Yemen, M. G. Da Gue, J.-M. Lehn, J. Chem. Phys., **68**, 1665 (1978).

18. M. G. DaGue, J. S. Landers, H. L. Lewis, J. L. Dye, Chem. Phys. Lett., **66**, 169 (1979).

19. D. Issa and J. L. Dye, J. Am. Chem. Soc., **104**, 3781 (1982).

20. A. Ellaboudy, J. L. Dye and P. B. Smith, J. Am. Chem. Soc., **105**, 6490 (1983).

21. J. S. Landers, J. L. Dye, A. Stacy and M. J. Sienko, J. Phys. Chem., **85**, 1096 (1981).

22. S. Jaenicke and J. L. Dye, J. Solid State Chem., **54**, 320 (1984).

23. J. L. Dye, M. G. DaGue, M. R. Yemen, J. S. Landers, H. L. Lewis, J. Phys. Chem., **84**, 1096 (1980).

24. D. Issa, A. Ellaboudy, R. Janakiraman and J. L. Dye, J. Phys. Chem., **88**, 3847 (1984).

25. J. Papaioannou, S. Jaenicke and J. L. Dye, in press.

26. J. L. Dye, Pure and Appl, Chem., **49**, 3 (1977).

27. W. Weyl, Annalen der Physik und Chemie, **197**, 601 (1864).

28. P. P. Edwards, Adv. Inorg. Chem. Radiochem., **25**, 135 (1982).

29. J. C. Thompson, Electrons in Liquid Ammonia, Oxford University Press, Oxford, 1976.

30. J. L. Dye, Electrons in Fluids, J. Jortner and N. R. Kestner, Eds., Springer-Verlag, Berlin, 1973, p. 77.

31. J. L. Dye, Metal-Ammonia Solutions, J. J. Lagowski and M. J. Sienko, Eds., IUPAC, Butterworths, London, 1970, p. 1.

32. W. L. Jolly, Prog. Inorg. Chem., **1**, 235 (1959).

33. R. A. Ogg, Jr., J. Am. Chem. Soc., **68**, 155 (1946); J. Chem. Phys., **14**, 114, 295 (1946).

34. J. Jortner, J. Chem. Phys., **30**, 839 (1959).

35. N. R. Kestner, J. Jortner, J. Phys. Chem., **77**, 1040 (1973).

36. M. F. Fox and E. Hayon, Chem. Phys. Letters, **25**, 511 (1974).

37. M. F. Fox and E. Hayon, J. Chem. Soc., Faraday Trans. I, **72**, 1990 (1976).

38. J. L. Dye, M. G. DeBacker, V. A. Nicely, J. Am. Chem. Soc., **92**, 5226 (1970).

39. M. T. Lok, F. J. Tehan and J. L. Dye, J. Phys. Chem., **76**, 2975 (1972).

40. R. R. Dewald and J. L. Dye, J. Phys. Chem., **68**, 121 (1964).

41. E. J. Hart and J. W. Boag, J. Am. Chem. Soc., **84**, 4090 (1962).

42. M. S. Matheson and L. M. Dorfman, Pulse Radiolysis, M.I.T. Press, Cambridge, Mass. (1969).

43. J. L. Dye, M. G. DeBacker and L. M. Dorfman, J. Chem. Phys., **52**, 6251 (1970).

44. S. Matalon, S. Golden and M. Ottolenghi, J. Phys. Chem., **73**, 3098 (1969).

45. J. L. Dye, C. W. Andrews and J. M. Ceraso, J. Phys. Chem., **79**, 3076 (1975).

46. C. J. Pedersen in Synthetic Multidentate Macrocyclic Compounds, R. M. Izatt and J. J. Christensen, Eds., Academic Press, New York, 1978, p. 1.

47. D. Bright and M. R. Truter, J. Chem. Soc, B, 1544 (1970).

48. J. M. Ceraso and J. L. Dye, J. Am. Chem. Soc. **95**, 4432 (1973).

49. J. M. Ceraso and J. L. Dye, J. Chem. Phys., **61**, 1585 (1974).

50. D. Moras and R. Weiss, Acta Crystallogr. B, **29**, 383 (1973).

51. A. Ellaboudy, M. L. Tinkham, B. Van Eck, J. L. Dye and P. B. Smith, J. Phys. Chem., **88**, 3852 (1984).

52. See for example: (a) K. J. Rao, J. Wong and M. J. Weber, J. Chem. Phys., **78**, 6228 (1983). (b) H. K. Pan, G. S. Knapp and S. L. Cooper, Colloid and Polymer Sci., **262**, 734 (1984).

53. B. K. Teo in EXAFS Spectroscopy: Techniques and Applications, B. K. Teo and D. C. Joy, Eds., Plenum Press, New York, 1981, p. 13.

54. E. A. Stern and S. M. Heald in Handbook on Synchrotron Radiation, V. 1, E. E. Koch, Ed., North-Holland Publishing Co., 1983, p. 955.

55. L. V. Azaroff and D. M. Pease, in X-ray Spectroscopy, L. V. Azaroff, Ed., McGraw-Hill, New York, 1974, p. 184.

56. J. S. Landers, Ph. D. Dissertation, Michigan State University, 1981.

57. D. Issa, Ph. D. Dissertation, Michigan State University, 1982.

58. B. Van Eck, Ph. D. Dissertation, Michgan State Universtiy, 1983.

59. A. S. Ellaboudy, Ph. D. Dissertation, Michigan State University, 1984.

60. M. R. Yemen, Ph. D. Dissertation, Michigan State University, 1982.

61. G. T. Kohman in The Art and Science of Growing Crystals, J. J. Gilman, Ed., John Wiley and Sons, Inc. New York, 1963, p. 152.

62. C. W. Bunn and H. Emmet, Discussions Faraday Soc., 5, 119 (1949).

63. M. L. Tinkham, A. Ellaboudy, J. L. Dye and P. B. Smith, J. Phys. Chem., 90, 14 (1986).

64. C. Kittel, Introduction to Solid State Physics, Fifth Edition, John Wiley and Sons, Inc., New York, 1976.

65. R. de L. Kronig, Z. Physik., 70, 317 (1931); 75, 191, 468 (1932).

66. (a) E. A. Stern, Phys. Rev. B, 10, 3027 (1974); (b) E. A. Stern, D. E. Sayers, and F. W. Lytle, ibid., 11, 4836 (1975).

67. P. A. Lee and G. Beni, Phys. Rev. B, 15, 2862 (1977).

68. B. K. Teo and P. A. Lee, J. Am. Chem. Soc., 101, 2815 (1979).

69. B. K. Teo, M. R. Antonio and B. A. Averill, J. Am. Chem. Soc., 105, 3751 (1983).

70. (a) F. W. Lytle, G. H. Via and J. H. Sinfelt, in Synchrotron Radiation Research, H. Winick and S. Doniach, Eds., Plenum Press, New York, 1980, p. 401. (b) F. W. Lytle, P. S. Wei, R. B. Greegor, G. H. Via, J. H. Sinfelt, J. Chem. Phys., 70, 4849 (1979).

71. For a description of CHESS see: B. W. Batterman in EXAFS Spectroscopy: Techniques and Applications, B.

K. Teo and D. C. Joy, Eds., Plenum Press, New York, 1981.

72. J. A. Bearden, Rev. Mod. Phys.. **39**, 78 (1967).

73. J. D. Dunitz, M. Dobler, P. Seiler and R. P. Phizackerley, Acta Crystallogr. **B30**, 2733 (1974).

74. (a) B. K. Teo, R. G. Shulman, G. S. Brown and A. E. Meixner, J. Am. Chem. Soc., **101**, 5624 (1979). (b) B. K. Teo, P. Eisenberger, B. M. Kincaid, ibid., **100**, 1735 (1977).

75. P. A. Lee, P. H. Citrin, P. Eisenberger, B. M. Kincaid, Rev. Mod. Phys., **53**, 769 (1981).

76. Cubic spline background removal program from Bell Laboratories. Spline approximation algorithm from: P. A. Fox, A. D. Hall, N. L. Schryer, The PORT Mathematical Subroutine Library, **1976**, Bell Laboratories computing Science Technical Report No. 47.

77. International Tables for X-ray Crystallography, Vol. III, Kynoch Press, Birmingham, UK, 1968, Table 3.2.2C pp. 171-173.

78. Fourier transform and filtering routines developed by B. M. Kincaid, Bell Laboratories.

79. M. R. Antonio, Ph. D. Dissertation, Michigan State University, 1983.

80. F. W. Kutzler, C. R. Natoli, D. K. Misemer, S. Doniach and K. O. Hodgson, J. Chem. Phys., **73**, 3274 (1980).

81. M. L. Tinkham and J. L. Dye, J. Am. Chem. Soc., **107**, 6129 (1985).

82. R. G. Shulman, Y. Yafet, P. Eisenberger and W. E. Blumberg, Proc. Natl. Acad. Sci., **73**, 1384 (1976).

83. B. K. Teo, J. Am. Chem. Soc., **103**, 3990 (1981).

84. M. R. Antonio, B. K. Teo and B. A. Averill, J. Am. Chem. Soc., **107**, 3583 (1985).

85. S. B. Dawes, Ph. D. Dissertation, Michigan State University, 1986.

86. M. L. Tinkham, Ph. D. Dissertation, Michigan State University, 1985.

87. International Tables for X-ray Crystallography, V. I, Kynoch Press, Birmingham, UK, 1965.

88. W. H. Zachariasen, Acta Crystallogr., **16**, 1139 (1963).

89. J. P. Glusker and K. N. Trueblood, Crystal Structure Analysis: A Primer, Oxford University Press, New York, 1972.

90. M. F. C. Ladd and R. A. Palmer, Structure Determination by X-Ray Crystallographhy, Plenum Press, New York, 1985.

91. B. A. Frenz, The Enraf-Nonius CAS 4 SDP - A Real-Time System for Concurrent X-Ray Data Collection and Crystal Structure Determination, H. Schenk, R. Olthof-Hazelkamp, H. van Kongsveld and G. C. Bassi, Eds., Delft University Press, Delft, Holland, 1978, pp.64 - 71.

92. D. T. Cromer and J. T. Waber, in International Tables forr X-Ray Crystallography, V. IV, Kynoch Press, Birmingham, UK, 1974, Table 2.2B, p. 99.

93. D. A. Liberman, unpublished results.

94. D. T. Cromer in International Tables for X-Ray Crystallography, V. IV, Kynoch Press, Birmingham, UK, 1974, Table 2.3.1, p. 149.

95. Evans and Sutherland PS300 Graphics System was used.

96. A. Bondi, J. Phys. Chem., **68**, 441 (1964).

97. (a) M. R. Truter, Struct. Bonding, **16**, 71 (1973).
(b) J.-M. Lehn, ibid., 1.

98. J. Kim, unpublished results, this laboratory.

99. L. K. Templeton and D. H. Templeton, Abstracts American Crystallographic Assoc. Proceedings, Series 2, V. I, p. 143.

100. M. K. Faber, Ph. D. Dissertation, Michigan State University, 1985.

101. R. R. Dewald and K. W. Browall, J. Phys. Chem., **74**, 129 (1970).